

A. Attachments

The publications related to Chapters 3, 4 and 5 are presented here. The post-print and arXiv versions can be accessed by following the indicated references in Table 1.

A.1 Can the ferroelectric soft-mode trigger an antiferromagnetic phase transition?

The paper “Can the ferroelectric soft-mode trigger an antiferromagnetic phase transition?”, Ref.^{A1}, regarding the quadruple perovskite $\text{BiMn}_3\text{Cr}_4\text{O}_{12}$ is presented in this section.



Can the ferroelectric soft mode trigger an antiferromagnetic phase transition?

André Maia^a, Christelle Kadlec^a, Maxim Savinov^a, Rui Vilarinho^b,
Joaquim Agostinho Moreira^b, Viktor Bovtun^a, Martin Kempa^a, Martin Míšek^a, Jiří Kaštil^a,
Andriy Prokhorov^a, Jan Maňák^a, Alexei A. Belik^c, Stanislav Kamba^{a,*}

^a Institute of Physics of the Czech Academy of Sciences, Na Slovance 1999/2, 182 21 Prague, Czech Republic

^b IFIMUP, Physics and Astronomy Department, Faculty of Sciences, University of Porto, Rua do Campo Alegre s/n, 4169-007, Porto, Portugal

^c International Center for Materials Nanoarchitectonics (WPI-MANA), National Institute for Materials Science (NIMS), Namiki 1-1, Tsukuba, Ibaraki 305-0044, Japan

ARTICLE INFO

Keywords:

Multiferroics
Phase transitions
Quadruple perovskites
Soft-modes
Phonons

ABSTRACT

Type-II multiferroics, where spin interactions induce a ferroelectric polarization, are interesting for new device functionalities due to large magnetoelectric coupling. We report on a new type of multiferroicity in the quadruple-perovskite $\text{BiMn}_3\text{Cr}_4\text{O}_{12}$, where an antiferromagnetic phase is induced by the structural change at the ferroelectric phase transition. The displacive nature of the ferroelectric phase transition at 125 K, with a crossover to an order-disorder mechanism, is evidenced by a polar soft phonon in the THz range and a central mode. Dielectric and pyroelectric studies show that the ferroelectric critical temperature corresponds to the previously reported Néel temperature of the Cr^{3+} spins. An increase in ferroelectric polarization is observed below 48 K, coinciding with the Néel temperature of the Mn^{3+} spins. This increase in polarization is attributed to an enhanced magnetoelectric coupling, as no change in the crystal symmetry below 48 K is detected from infrared and Raman spectra.

1. Introduction

Magnetoelectric multiferroics, where both magnetic and ferroelectric orders coexist and are coupled to one another, have received a lot of attention due to their potential numerous applications [1,2]. Quadruple perovskite multiferroics, with general chemical formula $(\text{AA}')\text{B}_4\text{O}_{12}$, are now being extensively studied due to their intriguing and, in some cases, large magnetically-driven ferroelectric polarization [3,4]. Recently, magnetoelectric multiferroicity was found in the A-site ordered quadrupole perovskite $\text{LaMn}_3\text{Cr}_4\text{O}_{12}$ (LMCO), where two antiferromagnetic (AFM) phase transitions, associated with the G-type ordering of the A-site Mn^{3+} and the B-site Cr^{3+} spins, take place at 50 and 150 K, respectively. [5] Due to the interplay between the Mn and Cr magnetic sublattices, a ferroelectric polarization of $\sim 1.5 \times 10^{-3} \mu\text{Ccm}^{-2}$ emerges [5]. This novel type of multiferroicity has been explained by the anisotropic symmetric exchange mechanism [6].

Since the $6s^2$ lone-pair electrons in ions like Bi^{3+} can lead to a large ferroelectric polarization, as in the type-I multiferroic BiFeO_3 ($60\text{--}100 \mu\text{Ccm}^{-2}$) [7], a new compound $\text{BiMn}_3\text{Cr}_4\text{O}_{12}$ (BMCO) was

recently sintered [8]. Surprisingly, BMCO was reported to exhibit both type-I and type-II multiferroic features [8]. Following the literature and starting from the high-temperature cubic phase with space group $Im\bar{3}$, BMCO undergoes the first ferroelectric phase transition (FE1 phase) at $T_{\text{FE1}} = 135$ K, marked by a broad anomaly in the temperature dependence of the permittivity ($\epsilon'_{\text{max}} \approx 420$) and the emergence of a spontaneous polarization [8] of $\approx 1.39 \mu\text{Ccm}^{-2}$ (at 70 K). The system enters the type-I multiferroic state at $T_{\text{N1}} \approx 125$ K, due to the stabilization of the G-type AFM order of the B-site Cr^{3+} spin sublattice, as revealed by neutron powder diffraction measurements [8]. On further cooling towards $T_{\text{N2}} \approx 48$ K, the second G-type AFM transition occurs for the A'-site Mn^{3+} sublattice [8]. The exchange interaction between these two magnetic sublattices induces a strong magnetoelectric coupling, which enhances the ferroelectric polarization by $\approx 0.19 \mu\text{Ccm}^{-2}$ below $T_{\text{FE2}} = T_{\text{N2}}$ [8]. This led the authors of reference [8] to claim that BMCO sequentially exhibits type-I and type-II multiferroic features, something unique among all multiferroics.

Although both LMCO and BMCO exhibit the same G-type AFM structure in the Mn^{3+} and Cr^{3+} spin sublattices, the spin-driven

* Corresponding author.

E-mail address: kamba@fzu.cz (S. Kamba).

<https://doi.org/10.1016/j.jeurceramsoc.2022.12.067>

Received 29 October 2022; Received in revised form 22 December 2022; Accepted 31 December 2022

Available online 2 January 2023

0955-2219/© 2023 Elsevier Ltd. All rights reserved.

contribution to the ferroelectric polarization at low temperatures in BMCO ($\sim 0.19\mu\text{Ccm}^{-2}$) is more than two orders of magnitude larger than that in LMCO ($\sim 1.5 \times 10^{-3} \mu\text{Ccm}^{-2}$) [5,8]. With the appearance of G-type AFM ordering on both Mn^{3+} and Cr^{3+} magnetic sublattices, the polar Cm structure (suggested by first-principle calculations) triggers the non-relativistic exchange striction mechanism, leading to a large spin-driven ferroelectric polarization [9]. While in BMCO the underlying mechanism for multiferroicity is exchange striction, in cubic $Im\bar{3}$ LMCO it is the weaker relativistic anisotropic symmetric exchange [6,9].

First-principles calculations suggest that the ferroelectric phase transition at T_{FEI} is driven by a soft polar optical phonon, which is predicted to exhibit a remarkable eigen-displacement of Bi^{3+} , inducing polarization and contributing as much as 93% to the lattice dielectric constant, due to the stereochemical activity of Bi $6s^2$ lone-pair electrons [9,10]. However, experimental evidence of the displacive nature of the ferroelectric phase transition is yet to be provided. Despite this, neutron powder, synchrotron X-ray and electron diffraction experiments did not reveal any deviations from the cubic symmetry, most likely due to the small lattice distortions below T_{FEI} [8].

The optical soft mode is generally a dynamical origin of displacive ferroelectric phase transitions. In this case, the increase in permittivity near T_C is caused by a softening, i.e., decrease in frequency, of one of the transversal polar phonons [11]. This can be understood from the Lyddane-Sachs-Teller relation: [12].

$$\frac{\epsilon_0}{\epsilon_\infty} = \prod_{j=1}^n \frac{\omega_{LOj}^2}{\omega_{TOj}^2} \quad (1)$$

describing the relation of the static permittivity, ϵ_0 , and the high-frequency (electronic) permittivity, ϵ_∞ , with the j -th longitudinal, ω_{LOj} , and transverse, ω_{TOj} , phonon frequencies. Assuming ϵ_∞ and all the ω_{LOj} to be temperature independent and that the static permittivity, ϵ_0 , follows the Curie-Weiss law, one of the transverse phonon frequencies (usually the lowest frequency phonon $\omega_{TO1} = \omega_{SM}$) should follow the Cochran law: [11].

$$\omega_{SM}^2 = A(T - T_C) \quad (2)$$

where A is the Cochran constant and T_C is the critical Curie temperature. As the predicted polar soft mode is infrared (IR) active, IR and THz spectroscopies are the best tools for verifying the predicted phonon softening when approaching T_{FEI} .

In this paper, we demonstrate that the ferroelectric phase transition is driven by the softening of a polar phonon. Moreover, we show that $T_{\text{FEI}} = T_{\text{N1}}$, meaning that the ferroelectric transition triggers the magnetic ordering, which is novel among type-II multiferroics. Microwave (MW) and EPR spectra hint that a strong dielectric relaxation, i.e., a soft central mode, should exist in the microwave region, approximately 30 K above T_{FEI} . The ferroelectric phase transition is shown to be predominantly of the displacive type, with a weak order-disorder character near T_{FEI} . Raman spectroscopy reveals a spin-phonon coupling below 130 K. The observed phonon activities are compared with the predictions from factor-group analysis and first-principles calculations. [9,10].

2. Experimental section

$\text{BiMn}_3\text{Cr}_4\text{O}_{12}$ ceramics were prepared from stoichiometric mixtures of Bi_2O_3 (99.9999%), Mn_2O_3 , and Cr_2O_3 (99.99%) at 6–7.5 GPa and about 1370 K for 1 h in 6 mm diameter Au capsules. Single-phase Mn_2O_3 was prepared from the commercial MnO_2 (99.997%) by heating in air at 923 K for 24 h. All oxides were provided by Alfa Aesar Chemicals or Rare Metallic Co. Ltd. The high-pressure and high-temperature sintering was necessary for the ordering of the Mn and Cr in the A and B perovskite sites, respectively. Laboratory powder X-ray diffraction (XRD) data were taken at room temperature using a MiniFlex600 diffractometer with CuK_α -radiation (2θ range of 10–80°, a step width of 0.02°, and a

counting speed of 1°min^{-1}). XRD data were analyzed by the Rietveld method with RIETAN-2000 program [13]. Weight fractions of impurities were estimated by RIETAN-2000 from refined scale factors. The best ceramics contained some impurities, specifically 1% of $\text{Bi}_2\text{O}_2\text{CO}_3$ and 1% Cr_2O_3 , while others contained up to 1% of $\text{Bi}_2\text{O}_2\text{CO}_3$, 3% of BiCrO_3 , and 8% Cr_2O_3 . The X-ray diffraction pattern at room temperature and scanning electron microscope images are shown in Figs. 1 and 2, respectively. For our investigations, we used the ceramics with a lower amount of impurities, while the others were only used to see the effect of impurities on the dielectric properties (see Fig. S1). It should be mentioned that some of the secondary phases are magnetic [14,15]. However, they exhibit different critical temperatures than $\text{BiMn}_3\text{Cr}_4\text{O}_{12}$, and a qualitatively different temperature dependence of magnetic susceptibility (see Fig. S2).

The low-frequency complex dielectric permittivity was measured from 10 to 300 K in the 1 kHz – 1 MHz frequency range using a HP4284A impedance analyzer together with a closed-cycle cryostat. The temperature rate and applied AC electric field was about 0.5 Kmin^{-1} and 1 Vcm^{-1} , respectively. The experimental specimen was fabricated as a 700 μm thin plane-parallel polished plate. Au-Pd electrodes with a diameter of 1 mm were evaporated using a Bal-Tex SCD 050 sputter coater onto the principal faces of the plates. The contacts for applying the electric field were provided by silver wires fixed to the electrodes with silver paste. The thermally stimulated depolarization current (TSDC) measurements were done using the Electrometer High Resistance Meter KEITHLEY 617. The temperature dependence of the current density was measured in heating runs, after cooling the sample down to 10 K under several poling electric fields. The specific heat was measured using a Quantum design PPM14.

MW resonance transmission measurements were performed using a composite dielectric resonator (DR), consisting of the base cylindrical DR and sample [17,18]. The disc-shaped sample without electrodes (1.8 mm thick, 5 mm in diameter) was placed on top of the base DR. The base and composite DRs were measured in the cylindrical shielding cavity using the transmission setup with a weak coupling by an Agilent E8364B network analyzer. The S_{21} transmission coefficients were recorded in the frequency range near and below the main TE_{018} mode of the base DR (≈ 5.8 GHz), i.e., from 1 to 7 GHz during heating from 10 to 400 K with a temperature rate of 0.5 Kmin^{-1} in a Janis closed cycle He cryostat. The temperature dependences of the S_{21} maxima, corresponding to the mean resonance frequencies, were used to study temperature evolution of the main excitations (of dielectric or magnetic origin) in the GHz range. The TE_{018} resonance frequency, quality factor

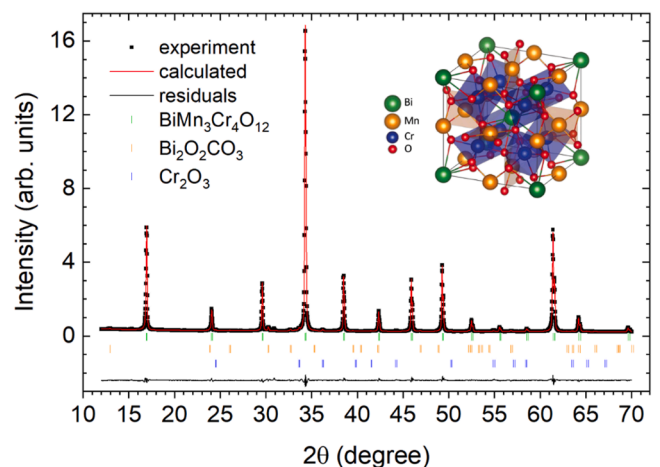


Fig. 1. X-ray diffraction pattern and result of Rietveld refinements at room temperature. The cubic quadruple-perovskite structure of $\text{BiMn}_3\text{Cr}_4\text{O}_{12}$ is depicted in inset, made using VESTA software [16]. In this sample, 2% of $\text{Bi}_2\text{O}_2\text{CO}_3$ and 3% of Cr_2O_3 impurities were detected.

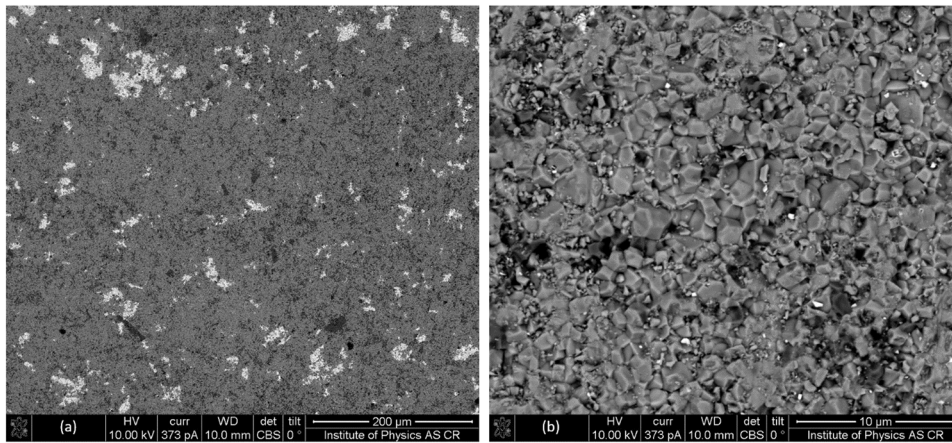


Fig. 2. Representative SEM images of a BiMn₃Cr₄O₁₂ ceramic sample at room temperature. Three different phases can be observed. The most predominant one (grey regions) is BiMn₃Cr₄O₁₂, while the white and black regions correspond to BiCrO₃ and Cr₂O₃ impurities, respectively. The chemical composition of some of these regions was determined using EDS. The Bi₂O₂CO₃ secondary phase observed in XRD was not detected in EDS, as this ceramic was from another batch than the sample in Fig. 1.

and insertion loss of the base DR, with and without the sample, were determined.

The EPR spectra were measured at X-band (9.384 GHz) in the 4–300K temperature range using the Bruker E580 ELEXSYS spectrometer equipped with the ER 4122 SHQE Super X High-Q cavity. The samples were placed on quartz rods of 4 mm in diameter. The following experimental parameters were used during the EPR measurements: 1.5 mW microwave power, 100 kHz modulation frequency, 0.2 mT modulation amplitude and 60 ms conversion time.

THz complex transmittance was measured using a custom-made time-domain spectrometer powered by a Ti:sapphire femtosecond laser with 35-fs-long pulses centered at 800 nm. The system is based on coherent generation and subsequent coherent detection of ultrashort THz transients. The detection scheme consists of an electro-optic sampling of the electric field of the transients within a 1-mm-thick, (110)-oriented ZnTe crystal as a sensor [19]. This allows measuring the time profile of the THz transients transmitted through the sample. Low-temperature IR reflectivity measurements were performed using a Bruker IFS-113v Fourier-transform IR spectrometer equipped with a liquid-He-cooled Si bolometer (1.6 K) serving as a detector. For both the THz complex transmittance and IR reflectivity measurements, the temperature control was done through an Oxford Instruments Optistat optical continuous He-flow cryostats with mylar and polyethylene windows, respectively. To fit the IR and THz spectra, due to a significant TO-LO splitting, a generalized-oscillator model with the factorized form of the complex permittivity was used:

$$\epsilon(\omega) = \epsilon'(\omega) - i\epsilon''(\omega) = \epsilon_\infty \prod_j \frac{\omega_{LOj}^2 - \omega^2 + i\omega\gamma_{LOj}}{\omega_{TOj}^2 - \omega^2 + i\omega\gamma_{TOj}} \quad (3)$$

where ω_{TOj} and ω_{LOj} denote the transverse and longitudinal frequencies of the j -th polar phonon, respectively, and γ_{TOj} and γ_{LOj} denote their corresponding damping constants. The high-frequency permittivity, ϵ_∞ , resulting from electronic absorption processes, was obtained from the room-temperature frequency-independent reflectivity tail above the phonon frequencies and was assumed temperature independent. The dielectric strength, $\Delta\epsilon_j$, of the j -th mode is: [20].

$$\Delta\epsilon_j = \frac{\epsilon_\infty}{\omega_{TOj}^2} \frac{\prod_k \omega_{LOk}^2 - \omega_{TOj}^2}{\prod_{k \neq j} \omega_{TOk}^2 - \omega_{TOj}^2} \quad (4)$$

The complex permittivity, $\epsilon(\omega)$, is related to the reflectivity, $R(\omega)$, by:

$$R(\omega) = \left| \frac{\sqrt{\epsilon(\omega)} - 1}{\sqrt{\epsilon(\omega)} + 1} \right|^2 \quad (5)$$

Unpolarized Raman spectra were recorded using a Renishaw inVia

Qontor spectrometer with a 532 nm linearly polarized diode-pumped laser and an edge filter. Measurements were done at fixed temperatures from 10 to 300 K using a THMS600 Linkam stage cooled by a nitrogen flow down to 80 K and a custom-made closed-cycle helium cryostat down to 10 K. The laser power (1.65 mW) was chosen adequately to prevent heating the sample. The wavenumber at a given temperature, $\omega(T)$, of each Raman mode is obtained by the best fit of the Raman spectra with a sum of damped oscillators: [21].

$$I(\omega, T) = [1 + n(\omega, T)]^{-1} \sum_j \frac{A_{0j} \Omega_{0j}^2 \Gamma_{0j} \omega}{(\Omega_{0j}^2 - \omega^2)^2 + \Gamma_{0j}^2 \omega^2} \quad (6)$$

where $n(\omega, T)$ is the Bose-Einstein factor and $A_{0j}, \Omega_{0j}, \Gamma_{0j}$ are the strength, wavenumber, and damping coefficient of the j -th oscillator, respectively. In the temperature range where no anomalous behavior is observed, the temperature dependence of the wavenumber of the phonon frequencies can be well described by the normal anharmonic temperature effect due to volume contraction as temperature decreases: [22].

$$\omega(T) = \omega_0 + C \left[1 + \frac{2}{e^x - 1} \right] \quad (7)$$

with $x \equiv \hbar\omega_0/2k_B T$ and where ω_0 and C are model constants, \hbar is the reduced Planck constant and k_B is the Boltzmann constant.

3. Results and discussion

3.1. Simultaneous Ferroelectric and Magnetic Phase Transitions

Fig. 3a shows the temperature dependencies of the real part of dielectric permittivity, $\epsilon'(T)$, measured at different fixed frequencies (1–1000 kHz range), and of the specific heat divided by temperature, $C_p(T)/T$. The $\epsilon'(T)$ curve exhibits anomalous behavior, peaking at 138 K, which has been interpreted in current literature as a manifestation of the ferroelectric phase transition [8]. The anomaly at 138 K is unusually broad, and the temperature for which $\epsilon'(T)$ is maximum lies 13 K above the high temperature anomaly observed in the $C_p(T)$ curve, at 125 K, in good agreement with reference [8]. $C_p(T)$ exhibits another anomaly at $T_{N2} = 48$ K. The anomalies of specific heat at 125 K and 48 K have been attributed as manifestation of the G-type AFM ordering of the Cr³⁺ and Mn³⁺ spins sublattices, respectively, corroborated by magnetic neutron diffraction [8]. The discrepancy between the temperatures where $\epsilon'(T)$ and $C_p(T)$ display anomalous behavior is incomprehensible, since ferroelectricity is predicted to be stabilized by the condensation of a polar phonon and, so, the lattice contribution to the specific heat should be large. This discrepancy, along with the rather broad anomaly in $\epsilon'(T)$,

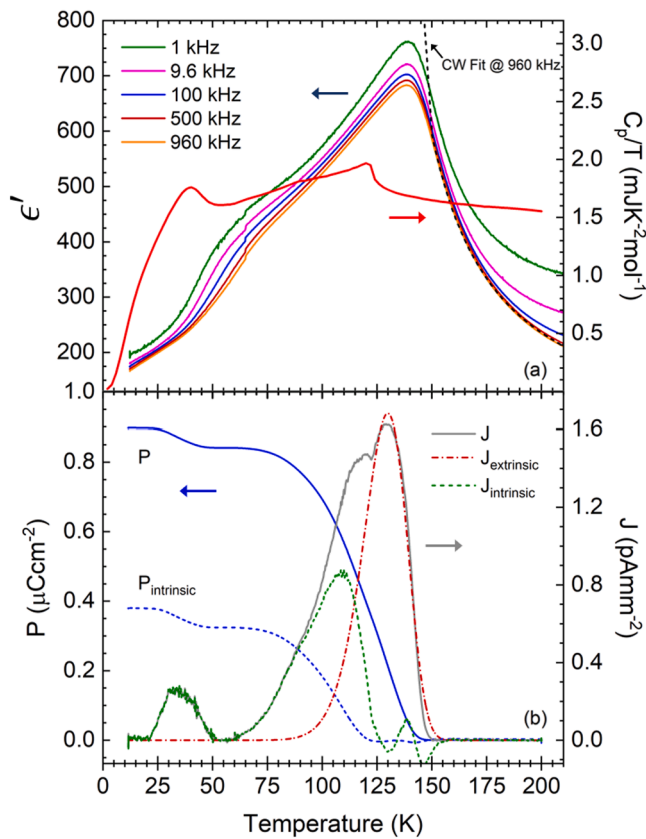


Fig. 3. (a) Temperature dependence of the real part of permittivity measured at selected frequencies and of the specific heat divided by temperature. The Curie-Weiss fit of permittivity at 960 kHz is shown as a dashed line, giving $T_C \approx 125.8$ K (see main text). (b) Temperature dependence of the TSDC density (right axis), measured with a heating rate of 0.5 Kmin^{-1} after cooling with a poling electric field of 0.7 kVcm^{-1} . The TSDC is decomposed by fitting the extrinsic component with Eq. 8 in the 125 – 200 K temperature range (see main text). The intrinsic ferroelectric polarization, $P_{\text{intrinsic}}$, was calculated from the low-temperature (green) component, $J_{\text{intrinsic}}$. The total “polarization” P , including both intrinsic and extrinsic contributions, is plotted as a solid blue line.

hint more complex mechanisms underlying the ferroelectric and anti-ferromagnetic phase transitions in this temperature range.

For these reasons, we have undertaken a careful study of the thermally stimulated depolarizing current (TSDC) density, J . As a representative example, Fig. 3b shows the temperature dependence of the $J(T)$ curve, measured with a heating rate of 0.5 K min^{-1} , after cooling the sample under a poling electric field of 0.7 kV cm^{-1} . The $J(T)$ curve displays two anomalies, a double maximum between 110 and 140 K, and another one at 32 K, with the shape and width of the highest temperature anomaly being unusual for a typical paraelectric-to-ferroelectric phase transition. The calculated electric polarization emerges below 138 K, reaching the value of $0.82 \mu\text{C cm}^{-2}$ at 60 K and $0.9 \mu\text{C cm}^{-2}$ at 10 K. Performing a similar TSDC density measurement after cooling with a poling field of 5.7 kV cm^{-1} yields a polarization of $3.7 \mu\text{C cm}^{-2}$ at 10 K (see Fig. S3 of Supporting Information). Furthermore, the polarization can be reversed by reversing the poling electric field (see Fig. S4).

The polarization values here reported are higher than the predicted values in reference [9], considering the polycrystalline character of our ceramics. Although the overall temperature dependence of permittivity and polarization qualitatively agree with those reported by Zhou et al. [8], quantitatively, we found higher values. The peak in permittivity at 138 K is almost 60% larger than in reference [8]. The enhanced permittivity seen in Fig. 3a, mainly at low frequencies and above 138 K, is assigned to the Maxwell-Wagner effect, evidencing partial extrinsic

contributions to both the electric permittivity and polarization, apparently enhancing both values [23]. In order to unravel the actual pyroelectric current, we measured the TSDC density at different heating rates ($0.1 - 25 \text{ K min}^{-1}$, see Fig. S5). The data recorded at the smallest temperature rate clearly shows two anomalies: a broader one peaking at 110 K and shaper one at 125 K. As the temperature rate increases, the higher temperature component upshifts by almost 25 K, while the lower one becomes sharper and the maxima shifts towards 128 K, and for high enough temperature rates ($> 2 \text{ Kmin}^{-1}$) it becomes a shoulder around 138 K. The higher temperature TSDC peak is associated with extrinsic thermally stimulated depolarization processes (e.g., Maxwell-Wagner relaxation [24] or other defect-induced relaxations [25,26]), which have nothing to do with the ferroelectric depolarization process as we will show in the following. The TSDC density, J , recorded between 100 K and 150 K, can be decomposed into two contributions by modeling the extrinsic peak, hereafter designated by $J_{\text{relaxation}}(T)$, using the equation: [26].

$$J_{\text{extrinsic}}(T) \approx \frac{P_e}{\tau_0} \exp\left(-\frac{E}{k_B T}\right) \exp\left[-\frac{k_B T^2}{q\tau_0 E} \exp\left(-\frac{E}{k_B T}\right)\right] \quad (8)$$

where P_e is a constant, τ_0 is the relaxation time at infinite temperature, E is the activation energy of dipolar orientation, and $q = dT/dt$ is the heating rate. A detailed description of this model is given in reference [26] and a representative example of the best fit of Eq. 8 to $J(T)$ is shown in Fig. 3b.

The intrinsic pyroelectric contribution to the TSDC density, $J_{\text{intrinsic}}$, is obtained by subtracting the extrinsic contribution from the total TSDC density, J , and its integration yields the actual ferroelectric polarization, $P_{\text{intrinsic}}(T)$ (Fig. 3b). The polarization is slightly lower than in reference 8 due to the lower poling field used in this study. It should be noted that the polarization resulting from integrating $J_{\text{intrinsic}}$ becomes non-zero below 125 K, evidencing that the ferroelectric phase transition and the G-type AFM ordering of the Cr^{3+} spin sublattice occur at the same temperature $T_{\text{FE1}} = T_{\text{N1}} = 125 \text{ K}$. This result is consistent with the $C_p(T)/T$ curve, as it exhibits an anomaly at this temperature, as expected.

The stabilization of the ferroelectric phase below $T_{\text{FE1}} = 125 \text{ K}$ is also evidenced by the hysteretic $P(E)$ loops, shown in Fig. S6. Both the coercive electric field and remnant polarization increase as temperature decreases from 120 K down to 50 K. Below 50 K, the maximum applied electric field of 10 kVcm^{-1} is not enough to induce a total domain reversal, and therefore, the measured hysteresis loops become narrower (see Fig. S6). A similar effect has been reported in other ferroelectric systems with high electrical conductivity [27,28].

The polarization increases below 50 K, i.e., approximately below T_{N2} (see Fig. 3b), most likely due to enhanced magnetoelectric coupling in the second AFM phase. Such anomaly in $P(T)$ does not necessarily require a change in crystal symmetry, as discussed in reference [8]. Furthermore, the dielectric dispersion seen near 50 K in Fig. 3a is not typical of a ferroelectric phase transition. The relaxation frequency obtained from $\epsilon''(T)$ follows the Arrhenius behavior typical for the freezing of ferroelectric domain walls or other thermally activated process (see Fig. S7 and accompanying discussion).

3.2. Displacive nature of the ferroelectric phase transition

Fig. 4a and b show the real and imaginary parts of the complex dielectric spectra, $\epsilon'(\omega)$ and $\epsilon''(\omega)$, respectively, of BMCO measured at several fixed temperatures in the THz range. At room temperature, only one polar phonon is observed at 26 cm^{-1} . As temperature decreases from 300 K towards 125 K, the phonon wavenumber shifts towards lower frequencies, while the static electric permittivity increases, and on further cooling, the phonon hardens. This temperature behavior is typical for a polar soft phonon which drives the ferroelectric phase transition. Such behavior was predicted in reference [9].

To better describe the temperature dependence of the polar soft

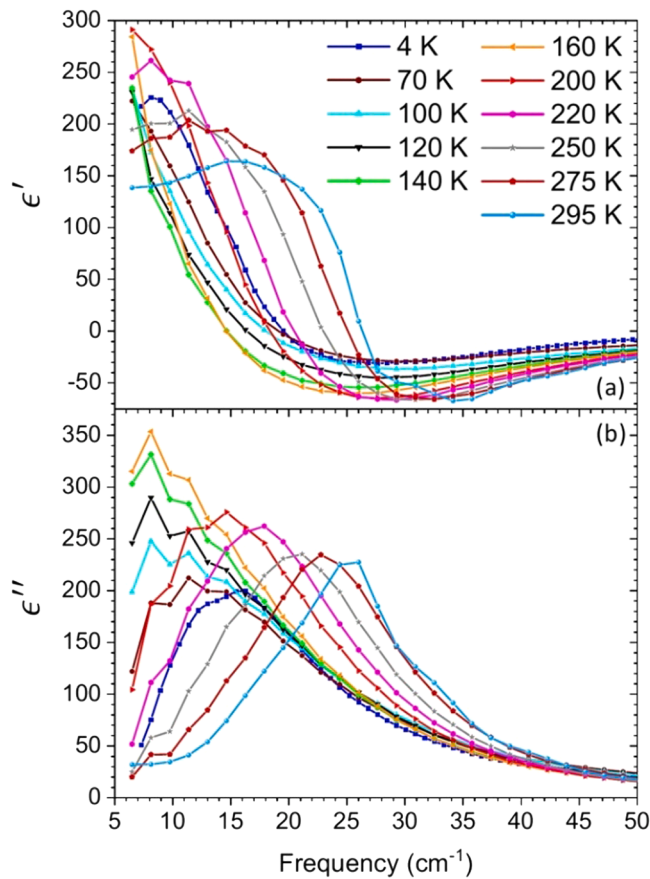


Fig. 4. (a) ϵ' and (b) ϵ'' spectra of $\text{BiMn}_3\text{Cr}_4\text{O}_{12}$ obtained by THz time-domain spectroscopy at several temperatures.

phonon and its contribution to the total permittivity, we have also probed the higher energy polar lattice excitations through temperature dependent unpolarized FTIR spectroscopy. Representative reflectivity spectra, recorded at 4 and 250 K, are shown in Fig. S8a. The spectra of the real and imaginary parts of permittivity, calculated from fitting the IR reflectivity spectra using Eqs. (3) and (5) (see Experimental Section), are also shown in Fig. S8b and S8c, respectively. The parameters of polar phonons at 4 and 250 K are listed in Table SI, together with the predicted frequency values obtained from first-principles calculations in reference [10]. Three new polar modes activate in the ferroelectric phase, due to a change of symmetry from cubic $Im\bar{3}$ to the lower symmetry phase, which has the Cm space group according to reference [9]. The factor-group analysis and the activity of phonons in IR and Raman spectra for both phases are also described in Supporting Information.

Fig. 5a and b show the temperature dependence of the soft mode wavenumber and its dielectric strength, respectively. The soft mode frequency, ω_{SM} , follows the Cochran law (Eq. 2) above 180 K. Below this temperature, $\omega_{SM}(T)$ deviates from the theoretical expectation, most likely due to enhanced anharmonicity near the ferroelectric phase transition. The critical temperature obtained from the Cochran fit to the experimental data above 180 K is $T_{FE1} = (125 \pm 1)\text{K}$, in excellent agreement with the intrinsic pyroelectric data and with the reported T_{N1} .

The dielectric strength of the soft phonon, $\Delta\epsilon_{SM}(T)$, considerably increases on cooling from 300 K towards T_{FE1} (see Fig. 5b). It is remarkable that $\Delta\epsilon_{SM}$ constitutes approximately 94% of the static electric permittivity in the THz range: $\epsilon_0 = \epsilon_\infty + \sum_j \Delta\epsilon_j$. It can also be seen in Fig. 5b that the sum rule of oscillator strengths is verified, as $\sum_j \Delta\epsilon_j \omega_{TOj}^2$ is temperature independent within the accuracy of our measurements. The

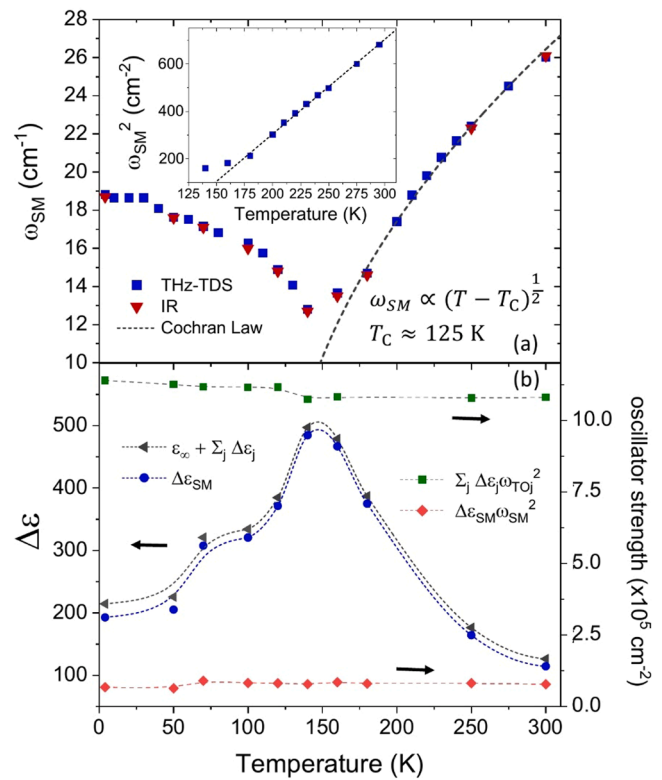


Fig. 5. (a) Temperature dependence of the soft-mode frequency in $\text{BiMn}_3\text{Cr}_4\text{O}_{12}$. The squares and triangles are soft-mode frequencies from fits of THz time-domain and IR spectra, respectively. The dashed line in (a) was calculated from the best fit of Cochran law (Eq. 2) to the soft mode frequency, in the 180–300 K temperature range. (b) Contribution of the soft mode to the static dielectric permittivity (left axis) and temperature dependence of the soft mode oscillator strength and sum of all oscillator strengths (right axis). The dashed lines in (b) are a guide for the eye.

soft phonon oscillator strength, $\Delta\epsilon_{SM}\omega_{SM}^2$ is temperature independent, meaning that it is not significantly coupled with other phonons [11]. Based on these results, we have fitted the $\epsilon'(T)$ in the paraelectric phase using the Curie-Weiss law (revisit Fig. 3a): $\epsilon'(T) = \epsilon_{HT} + C(T - T_C)^{-1}$, and we have obtained $T_C = (126 \pm 1)\text{K}$, $C = 13327\text{K}$ and $\epsilon_{HT} = 83.6$. In this way, we again confirmed that the ferroelectric phase transition occurs $\approx 10\text{K}$ below the peak in $\epsilon'(T)$. This seems unusual, but a similar behavior has been observed in relaxor-based ferroelectrics PZN-PT and PMN-PT, where some dielectric relaxation occurs above T_C [23,29,30]. In the next section, we describe the observation of a similar dielectric relaxation (central mode) in $\text{BiMn}_3\text{Cr}_4\text{O}_{12}$.

3.3. Displacive ferroelectric phase transition with order-disorder crossover

The deviation from the Cochran law ascertained below 180 K (55 K above T_{FE1}) in Fig. 5a and the broad anomaly observed in $\epsilon'(T)$ around 135 K (see Fig. 3a), are consequence of a dynamical central mode; i.e., a dielectric relaxation in the microwave range, which frequently activates near the Curie temperature in many displacive ferroelectrics due to the large lattice anharmonicity [11]. The static phonon permittivity (denoted by black triangles in Fig. 5b) being 25% lower than the radio-frequency one (Fig. 3a) supports this statement. To confirm this hypothesis, temperature dependent microwave resonance measurements were performed, and the corresponding results are shown in Fig. 6a, revealing at least three temperature-dependent resonance modes above 150 K which are well seen in the frequency-temperature S_{21} map.

The lowest-frequency component is the TE_{018} mode of the composite

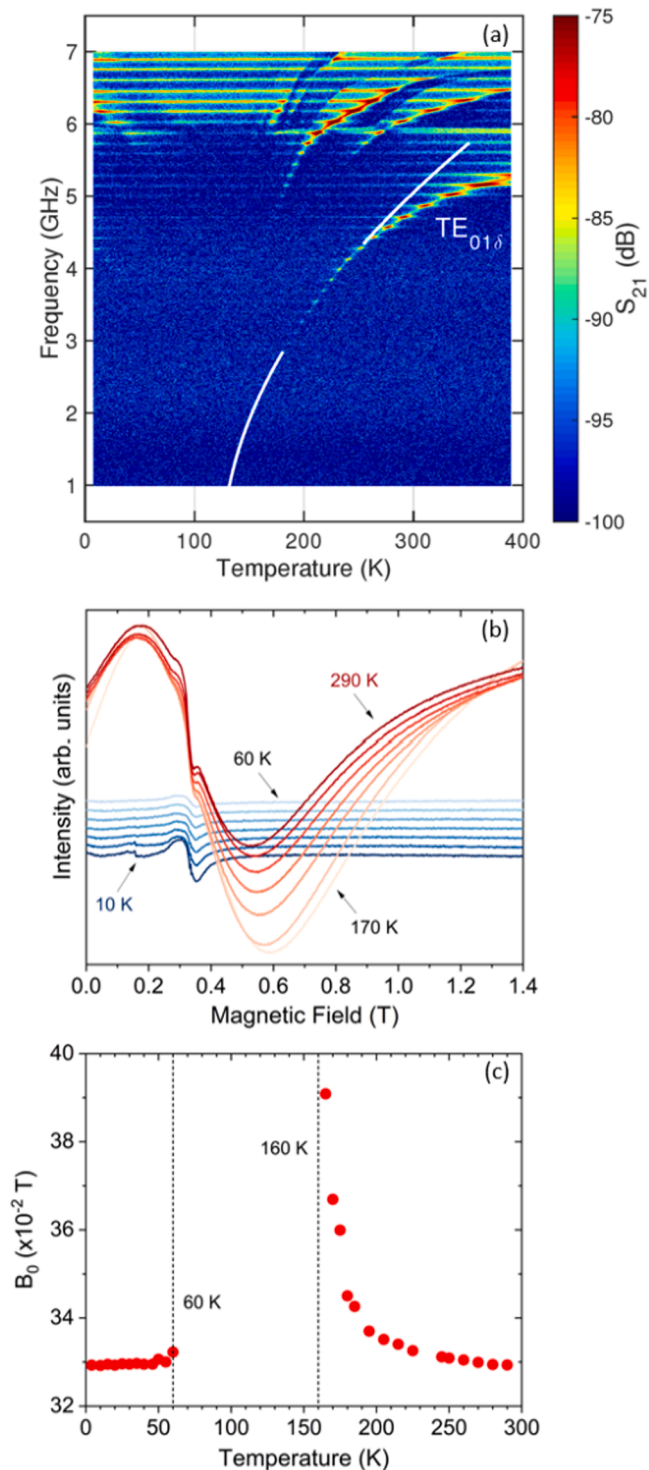


Fig. 6. (a) Frequency-temperature map of S_{21} transmission coefficient of the composite DR with $\text{BiMn}_3\text{Cr}_4\text{O}_{12}$. The colors correspond to S_{21} values. The white solid line shows a fit of the $\text{TE}_{01\delta}$ mode frequency to a Cochran-like temperature dependence, as described in the main text. This line is discontinued between 180 and 260 K so that the experimental mode signal remains visible. (b) Derivative of the EPR spectra at 9.384 GHz between 4 and 290 K. The EPR spectra could not be measured between 60 and 160 K due to enhanced microwave losses caused by the central mode. (c) Temperature dependence of the magnetic field of the center line, B_0 , which dramatically increases on cooling towards 160 K.

dielectric resonator (DR). No spectral component could be seen below 150 K, due to the high microwave losses of BMCO, probably of both magnetic and polar origin. High microwave losses in the whole temperature range are evidenced by both high insertion loss (see S_{21} scale in Fig. 6a) and low quality factor Q of the composite DR $\text{TE}_{01\delta}$ mode. The Q factor of the base DR changes from 14 000 at 10 K, to 6000 at 390 K, while that of the composite DR ranges in the 200 – 300 interval, in the 190 – 390 K temperature range, and even less below 190 K, making resonances undetectable. This result indicates the existence of a dynamical central mode close to T_{FE1} . Despite the low signal-to-noise ratio, the $\text{TE}_{01\delta}$ mode resonance maxima are well defined in the S_{21} spectra only above 160 K, allowing a reliable determination of the temperature dependence of the resonance frequency, f_{TE} . The $\text{TE}_{01\delta}$ mode slowing down on cooling is well described with the critical “Cochran-like” function: $f_{\text{TE}}(T) = f_0(T - T_c)^{1/2}$, with $f_0 = 382$ MHz and critical temperature $T_c \approx 125$ K. The critical behavior of $f_{\text{TE}}(T)$ resembles that of the soft phonon frequency, $\omega_{\text{SM}}(T)$, with the same T_c (see Fig. 5a). This is because the relation of the $\text{TE}_{01\delta}$ mode to the Curie-Weiss law (Fig. 6a) with the microwave dielectric permittivity is similar to that of the soft mode, since f_{TE} is mainly defined by the effective dielectric permittivity of the composite DR; i.e., by the electric permittivity of the base and sample [17]. Because the magnetic permeability of BMCO is $\mu' \neq 1$, the electromagnetic response, $\epsilon'\mu'$, should be considered instead of electric permittivity. [31] As the electric permittivity of the base DR is nearly temperature independent, and the relative changes in temperature of the magnetic susceptibility of BMCO are much smaller than the ones in its electrical permittivity (see Fig. S2 and reference 8), the observed slowing down of the $\text{TE}_{01\delta}$ mode should be attributed to the Curie-Weiss law for microwave dielectric permittivity (Fig. 6a), similarly to the soft mode. The deviation of f_{TE} from the critical “Cochran-like” function at high temperatures is caused by the increasing influence of the temperature independent component of the composite DR effective permittivity, i.e., the dielectric permittivity of the base. Three other resonance modes (seen above $\text{TE}_{01\delta}$ in Fig. 6a) also critically slow down on cooling. However, we cannot clearly define their type. Nevertheless, the critical temperature dependence of their frequencies above 160 K could be related to the Curie-Weiss law for the microwave dielectric permittivity of BMCO. At lower temperatures, these modes are overdamped by the high microwave magnetic and dielectric losses of the sample.

Fig. 6b shows the derivative of EPR absorption line spectra of BMCO measured down to 4 K. The temperature dependence of the magnetic field, B_0 , of the center line is shown in Fig. 6c. The EPR spectra disappear below 160 K, 35 K above T_{FE1} , as the microwave dielectric loss strongly increases. The microwave loss decreases again below 60 K due to the slowing down of ferroelectric domain wall motion and the hardening of the optical soft mode. This makes it again possible to measure the EPR spectra at lower temperatures. The broadening of the EPR lines on cooling towards 160 K is a consequence of correlated atomic shifts in the local environment of the paramagnetic Mn and Cr centers occupying the A' - and B -sites. [27,32] At 48 K, there is a change in the resonant field B_0 . This temperature roughly corresponds to T_{N2} .

The dramatic enhancement of the microwave loss below 160 K, evidenced by both microwave and EPR experiments, is explained by a dynamical central mode which is responsible for the deviation of the soft mode frequency from the Cochran law above T_{FE1} (Fig. 5a) and the fact that the phonon permittivity is 25% lower than the permittivity measured in the kHz frequency range (Fig. 3a). This means that the ferroelectric phase transition in BMCO is displacive but with a crossover with order-disorder type close to T_{FE1} . Moreover, the dynamical central peak is also responsible for the broad anomaly observed in the low-frequency $\epsilon'(T)$ and explains why the maximum value occurs above to T_{FE1} .

3.4. Spin-phonon coupling

The spin-phonon coupling was investigated using Raman spectroscopy. The unpolarized Raman spectra recorded at several temperatures in the $100 - 800 \text{ cm}^{-1}$ range are displayed in Fig. S9. The predicted Raman mode frequencies in the cubic phase, along with the experimental values observed at 10 K and 300 K, are shown in Table SII. Although expected from the symmetry point of view, no new bands could be observed below T_{FE1} within the detection limit of the spectrometer. It can be explained by their overlapping with other modes or by weak intensities due to small lattice distortion in the ferroelectric phase. The later explanation is supported by results of X-ray and neutron diffraction, where no crystal symmetry change could be detected [8].

However, a detailed inspection of the temperature dependence of some lattice modes reveals interesting features. Fig. 7 shows the temperature dependence of selected Raman mode frequencies. The solid lines were obtained from the best fit of Eq. 7 (see Experimental Section) to the experimental values in the temperature range $T > T_{\text{FE1}}$, extrapolated down to 0 K. The deviation from the expected anharmonic behavior makes it necessary to consider spin-phonon coupling. A frequency upshift (downshift) of a given phonon as a function of temperature due to the spin-phonon coupling should occur for dominant AFM (FM) interactions [33,34]. For the analyzed modes, the wavenumber follows the expected anharmonic temperature dependence from 300 K down to 125 K, but a downshift is seen below T_{N1} . Interestingly, the same modes exhibit a frequency upshift in LMCO [5]. Even though no new bands were detected, the temperature dependence of the lowest frequency phonon (see Fig. 7) exhibits a minimum at 75 K and below T_{N2} , it recovers the expected anharmonic temperature dependence of high temperature, extrapolated down to 10 K. This evidences structural changes at T_{N2} induced by magnetism.

The mechanisms underlying these lattice distortions are still unknown. These can be explained via the Dzyaloshinskii-Moriya interaction that, in non-centrosymmetric ferroelectric and AFM systems, such as BMCO, favors a spin canting of otherwise collinear (antiparallel)

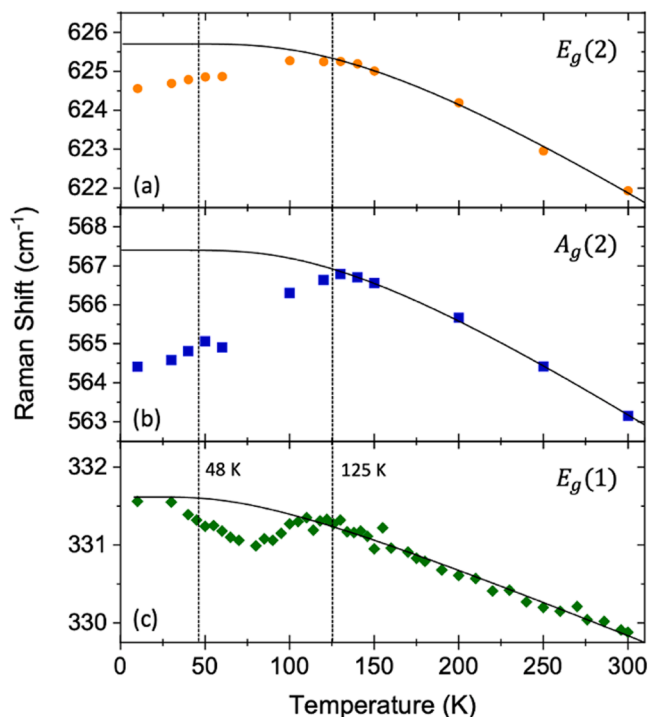


Fig. 7. Temperature dependence of the frequencies of selected Raman modes. The best fit with Eq. 7 in the paraelectric phase is represented by a solid line and is extrapolated down to 0 K.

magnetic moments, thus acting as a source of weak ferromagnetic behavior in an antiferromagnet [35]. This is possible in BMCO because, unlike LMCO, it exhibits a polar space group below T_{FE1} . Another explanation could be the influence of the structural phase transition at T_{FE1} . Since the deviation of the phonon frequencies from the anharmonic behavior described by Eq. 7 was observed also in LMCO [5], the spin-phonon coupling is a more plausible origin.

To obtain quantitative information regarding the order of the coupling term, we have analyzed the temperature dependence of the anomalous contribution to the phonon wavenumber, $\Delta\omega$, and the intensity of the magnetic neutron diffraction peaks, taken from reference 8. The $\Delta\omega$ values were determined from the difference between the extrapolated anharmonic temperature dependence of the phonon wavenumber and the experimental one. The results are displayed in Fig. 8.

Considering the two highest wavenumber phonons shown in Fig. 7, a similar temperature dependence to that observed for the magnetic peak intensity is found. As the intensity of the magnetic peak is proportional to the magnetic order parameters, a linear spin-phonon coupling is ascertained for these two phonons. The behavior of the lowest wavenumber phonon is interesting. Although it does not follow any magnetic peak diffraction temperature trend, the anomalous contribution $\Delta\omega$ changes its temperature dependence at the same temperature as the magnetic peak associated with the magnetic phase transition taking place at T_{N2} . The results here reported clearly evidence an interplay between lattice and spin systems.

4. Conclusions

The experimental results here reported give clear evidence for the displacive nature of the ferroelectric phase transition, triggered by a polar soft phonon. Following the results reported by Dai and Zhang [9], the instability of the polar soft phonon, with T_u symmetry in the cubic phase, mainly originates from the Bi^{3+} cation. However, the Bi^{3+} cation is also involved on the dynamical central peak, resulting in the ferroelectric phase transition having both displacive and order-disorder natures. This interpretation is supported by the results of Zhou et. al., [8] as the temperature dependence of the thermal parameter of Bi^{3+} shows a decrease below T_{FE1} . The existence of the dynamical central peak in the microwave spectral region explains the rather broad anomaly observed in the temperature dependence of the real part of the complex electric permittivity, around T_{FE1} .

The analysis of the temperature dependence of the TSDC density

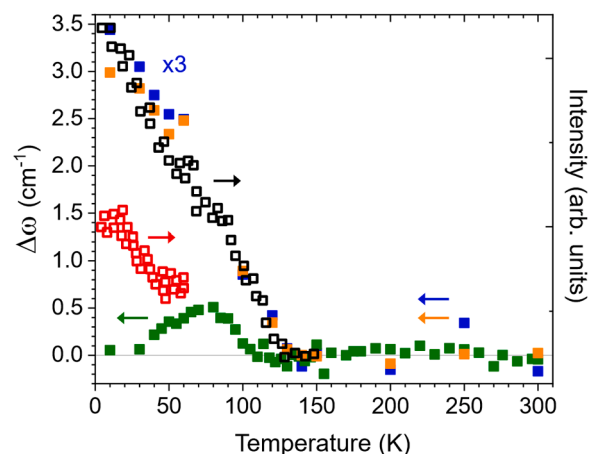


Fig. 8. Temperature dependence of the anomalous contribution to the phonon wavenumber, $\Delta\omega$, (closed symbols, left axis) and the intensity of the magnetic neutron diffraction peaks (open symbols, right axis), taken from reference 8. For comparison purposes, we have kept the same color code for the phonons as in Fig. 7.

enables to unravel the extrinsic mechanisms for polarization and subtract their contribution to the overall polarization. Moreover, the ferroelectric critical temperature, T_{FE1} , extrapolated from the Cochran and Curie-Weiss laws, matches the Néel temperature, $T_{N1} = 125$ K. Based in these results, along with the clear anomaly observed in the specific heat as a function of temperature, we propose that both the ferroelectric phase transition and the G-type AFM ordering of the B-site Cr^{3+} spins occur at the same temperature, i.e., $T_{FE1} = T_{N1} = 125$ K. Moreover, since the ferroelectric polarization is induced by the polar soft phonon, we consider polarization as the primary order parameter, which is coupled to the magnetic one. In this picture, the ferroelectric phase transition triggers the antiferromagnetic order in an originally paramagnetic/paraelectric state. Supporting this interpretation, we must consider the linear relationship between the anomalous contribution to the Raman-active phonon wavenumber and the intensity of the magnetic diffraction peaks, which clearly evidence a linear spin-lattice coupling in this compound. This interpretation makes $BiMn_3Cr_4O_{12}$ a special case of multiferroicity, although no microscopic theory exists yet. To the knowledge of the authors, there are only two theoretical papers [36,37] proposing that ferroelectricity can induce weak ferromagnetism in an originally antiferromagnetic phase, which is not applicable to this case. Nevertheless, one can expect that the structural change at T_{FE1} can modify the magnetic exchange interactions, giving rise to an AFM order at the same temperature. A phenomenological theory of ferroelectric phase transitions triggered by an instability of the crystal with respect to another phase transition parameter has already been published by Holakovský [38]. A similar theory can be applied to an AFM phase transition triggered by a structural (ferroelectric) phase transition.

Below $T_{N2} = 48$ K, the G-type antiferromagnetic ordering of Mn^{3+} spin magnetic sublattice enhances the ferroelectric polarization. Both IR and Raman spectra do not disclose new bands pointing for any additional symmetry-breaking below that temperature. A similar enhancement of ferroelectric polarization has been reported in other multiferroics like $BiFeO_3$ and $CdMn_7O_{12}$ [4,39]. However, precursor structural distortions occur above T_{N2} , as ascertained from the minimum value reached by the Raman-active phonon wavenumber, peaking at 330 cm^{-1} (see Figs. 7 and 8).

Summarizing, we reported an updated view of the phase sequence of $BiMn_3Cr_4O_{12}$. The possibility of a ferroelectric soft phonon instability triggering a G-type antiferromagnetic phase transition is proposed based on a comprehensive experimental study of this material. This is a remarkable result that will motivate a discussion on the coupling between the polar lattice instability and the magnetic order parameter.

Declaration of Competing Interest

The authors declare that they have no known competing financial interests or personal relationships that could have appeared to influence the work reported in this paper.

Acknowledgments

This work has been supported by the Czech Science Foundation (Project No. 21-06802S) and the MŠMT Project SOLID 21- CZ.02.1.01/0.0/0.0/16.019/0000760. Experiments were partly performed in MGML (mgml.eu), which is supported within the program of Czech Research Infrastructures (project no. LM2018096).

Appendix A. Supporting information

Supplementary data associated with this article can be found in the online version at [doi:10.1016/j.jeurceramsoc.2022.12.067](https://doi.org/10.1016/j.jeurceramsoc.2022.12.067).

References

- [1] Y. Tokura, S. Seki, N. Nagaosa, Multiferroics of spin origin, *Rep. Prog. Phys.* 77 (2014), 076501.
- [2] S. Dong, J.M. Liu, S.W. Cheong, Z. Ren, Multiferroic materials and magnetoelectric physics: symmetry, entanglement, excitation, and topology, *Adv. Phys.* 64 (2015) 519–626.
- [3] R.D. Johnson, et al., Giant improper ferroelectricity in the ferroaxial magnet $CaMn_7O_{12}$, *Phys. Rev. Lett.* 108 (2012), 067201.
- [4] N.J. Perks, R.D. Johnson, C. Martin, L.C. Chapon, P.G. Radaelli, Magneto-orbital helices as a route to coupling magnetism and ferroelectricity in multiferroic $CaMn_7O_{12}$, *Nat. Commun.* 3 (2012) 1–6.
- [5] X. Wang, et al., Observation of magnetoelectric multiferroicity in a cubic perovskite system: $LaMn_3Cr_4O_{12}$, *Phys. Rev. Lett.* 115 (2015), 087601.
- [6] J.S. Feng, H.J. Xiang, Anisotropic symmetric exchange as a new mechanism for multiferroicity, *Phys. Rev. B* 93 (2016), 174416.
- [7] G. Catalan, J.F. Scott, Physics and applications of bismuth ferrite, *Adv. Mater.* 21 (2009) 2463–2485.
- [8] L. Zhou, et al., Realization of large electric polarization and strong magnetoelectric coupling in $BiMn_3Cr_4O_{12}$, *Adv. Mater.* 29 (2017) 1703435.
- [9] J.Q. Dai, C.C. Zhang, Ferroelectricity driven by soft phonon and spin order in multiferroic $BiMn_3Cr_4O_{12}$, *J. Am. Ceram. Soc.* 102 (2019) 6048–6059.
- [10] J.Q. Dai, X.L. Liang, Y.S. Lu, Electronic structure, lattice dynamics, and dielectric properties in cubic perovskite $BiMn_3Cr_4O_{12}$ and $LaMn_3Cr_4O_{12}$, *Chem. Phys.* 538 (2020), 110924.
- [11] S. Kamba, Soft-mode spectroscopy of ferroelectrics and multiferroics: a review, *APL Mater.* 9 (2021), 020704.
- [12] R.H. Lyddane, R.G. Sachs, E. Teller, On the polar vibrations of alkali halides, *Phys. Rev.* 59 (1941) 673–676.
- [13] F. Izumi, T. Ikeda, A Rietveld-analysis program RIETAN-98 and its applications to zeolites, *Mater. Sci. Forum* 321–324 1 (2000) 198–204.
- [14] D.N. Astrov, The magnetoelectric effect in antiferromagnets, *Soviet Phys. JETP* 11 (1960) 708–709. http://www.jetp.ras.ru/cgi-bin/dn/e_011_03_0708.pdf.
- [15] A.A. Belik, N. Tsujii, H. Suzuki, E. Takayama-Muromachi, Magnetic properties of bulk $BiCrO_3$ studied with dc and ac magnetization and specific heat, *Inorg. Chem.* 46 (2007) 8746–8751.
- [16] K. Momma, F. Izumi, VESTA3 for three-dimensional visualization of crystal, volumetric and morphology data, *J. Appl. Crystallogr.* 44 (2011) 1272–1276.
- [17] V. Bovtun, et al., An electrode-free method of characterizing the microwave dielectric properties of high-permittivity thin films, *J. Appl. Phys.* 109 (2011), 024106.
- [18] V. Bovtun, et al., Microwave characterization of thin ferroelectric films without electrodes by composite dielectric resonator, *Integr. Ferroelectr.* 98 (2008) 53–61.
- [19] V. Skoromets, C. Kadlec, H. Némec, D. Fattakhova-Rohlfing, P. Kužel, Tunable dielectric properties of $KTaO_3$ single crystals in the terahertz range, *J. Phys. D: Appl. Phys.* 49 (2016), 065306.
- [20] F. Gervais, High-temperature Infrared reflectivity spectroscopy by scanning interferometry, *Infrared Millim. Waves: Electromagnetic Waves in Matter*, in: Academic Press, 8, 1983, p. 279.
- [21] W. Hayes, R. London, *Scattering of Light by Crystals*, Wiley-Interscience, 1979.
- [22] M. Balkanski, R.F. Wallis, E. Haro, Anharmonic effects in light scattering due to optical phonons in silicon, *Phys. Rev. B* 28 (1983) 1928–1934.
- [23] E.M. Sabolsky, S. Trolier-Mckinstry, Dielectric and piezoelectric properties of [001] fiber-textured $0.675Pb(Mg_{1/3}Nb_{2/3})O_3 - 0.325PbTiO_3$ ceramics, *J. Appl. Phys.* 93 (2003) 4072–4080, <https://doi.org/10.1063/1.1554488>.
- [24] C. De, S. Ghara, A. Sundaresan, Effect of internal electric field on ferroelectric polarization in multiferroic $TbMnO_3$, *Solid State Commun.* 205 (2015) 61–65.
- [25] S. Jachalke, et al., How to measure the pyroelectric coefficient? *Appl. Phys. Rev.* 4 (2017), 021303.
- [26] J. Vanderschueren, J. Gasiot, Field-induced thermally stimulated currents, vol. 37, Springer-Verlag, 1979.
- [27] I. Stefanik, C. Rudowicz, P. Gnutek, A. Suchocki, EPR study of Cr^{3+} and Fe^{3+} impurity ions in nominally pure and Co^{2+} -doped $YAlO_3$ single crystals, *Appl. Magn. Reson.* 36 (2009) 371–380.
- [28] E. Balashova, A.A. Levin, A. Fokin, A. Redkov, B. Krichetsov, Structural properties and dielectric hysteresis of molecular organic ferroelectric grown from different solvents, *Crystals* 11 (2021) 1278.
- [29] S.E. Park, T.R. Shrout, Ultrahigh strain and piezoelectric behavior in relaxor based ferroelectric single crystals, *J. Appl. Phys.* 82 (1997) 1804–1811.
- [30] M.L. Mulvihill, et al., The role of processing variables in the flux growth of lead zinc niobate-lead titanate relaxor ferroelectric single crystals, *Jpn. J. Appl. Phys.* 35 (1996) 3984–3990.
- [31] V. Goian, et al., Spin-phonon coupling in epitaxial $Sr_{0.6}Ba_{0.4}MnO_3$ thin film, *Phys. Rev. B* 95 (2017), 075126, <https://doi.org/10.1103/PhysRevB.95.075126>.
- [32] J.G.S. Duque, et al., Electron spin resonance (ESR) and microwave absorption studies in $TbMnO_3$ multiferroic compound, *IEEE Trans. Magn.* 42 (2006) 3084–3086.
- [33] W. Baltensperger, J.S. Helman, Influence of magnetic order in insulators on the optical phonon frequency, *Helv. Phys. Acta* 41 (1968) 668.
- [34] K. Wakamura, T. Arai, Effect of magnetic ordering on phonon parameters for infrared active modes in ferromagnetic spinel $CdCr_2S_4$, *J. Appl. Phys.* 63 (1988) 5824–5829.
- [35] T. Moriya, Anisotropic superexchange interaction and weak ferromagnetism, *Phys. Rev. Lett.* 120 (1960) 91–98.
- [36] D.L. Fox, J.F. Scott, Ferroelectrically induced ferromagnetism, *J. Phys. C: Solid State Phys.* 10 (1977) 19–22.

- [37] C.J. Fennie, Ferroelectrically induced weak ferromagnetism by design, *Phys. Rev. Lett.* 100 (2008), 167203.
- [38] J. Holakovsky, A new type of the ferroelectric phase transition, *Phys. Status Solidi B* 56 (1973) 615–619.
- [39] J.H. Lee, R.S. Fishman, Giant spin-driven ferroelectric polarization in BiFeO₃ at room temperature, *Phys. Rev. Lett.* 115 (2015), 207203.

Supporting Information

Can the Ferroelectric Soft Mode Trigger an Antiferromagnetic Phase Transition?

André Maia¹, Christelle Kadlec¹, Maxim Savinov¹, Rui Vilarinho², Joaquim Agostinho Moreira², Viktor Bovtun¹, Martin Kempa¹, Martin Míšek¹, Jiří Kaštil¹, Andriy Prokhorov¹, Jan Maňák¹, Alexei A. Belik³ and Stanislav Kamba^{1*}

¹*Institute of Physics of the Czech Academy of Sciences, Na Slovance 1999/2, 182 21 Prague, Czech Republic*

²*IFIMUP, Physics and Astronomy Department, Faculty of Sciences, University of Porto, Rua do Campo Alegre s/n, 4169-007, Porto, Portugal*

³*International Center for Materials Nanoarchitectonics (WPI-MANA), National Institute for Materials Science (NIMS), Namiki 1-1, Tsukuba, Ibaraki 305-0044, Japan*

*e-mail: kamba@fzu.cz

Sample Characterization

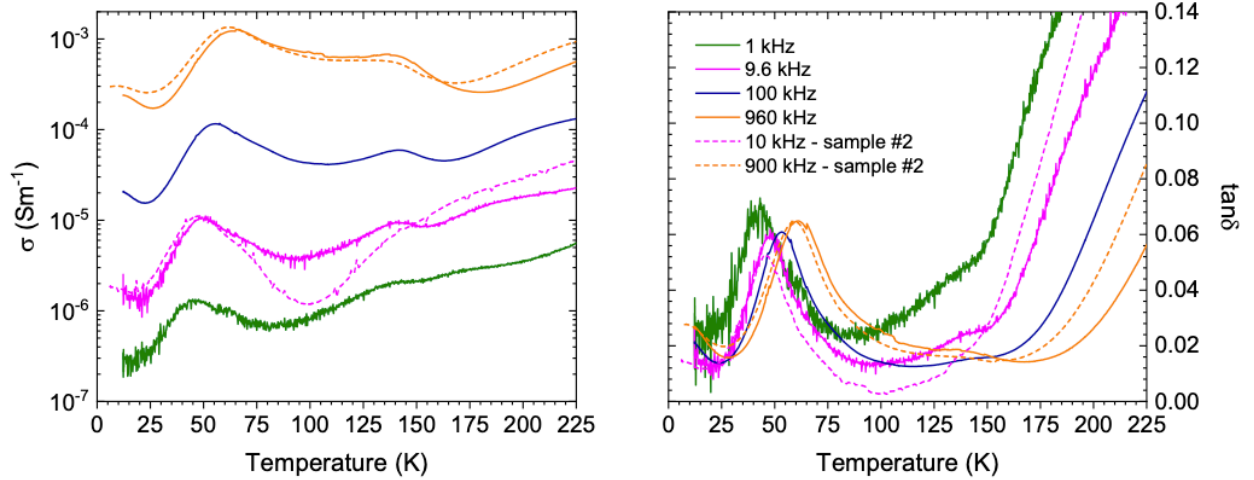


Figure S1. Temperature dependence of the conductivity and the dielectric loss measured at several frequencies. The dashed lines show results obtained at 9.6 kHz and 960 kHz on another sample (#2) with a higher impurity content (1% of $\text{Bi}_2\text{O}_2\text{CO}_3$, 3% of BiCrO_3 , and 8% Cr_2O_3). The higher quality sample has 1% of $\text{Bi}_2\text{O}_2\text{CO}_3$, 1% BiCrO_3 , and 3% Cr_2O_3 .

Factor group analysis of the lattice vibrations in the high-temperature cubic phase

In the cubic paraelectric $Im\bar{3}$ phase of $\text{BiMn}_3\text{Cr}_4\text{O}_{12}$, the Bi, Mn, Cr and O ions occupy the $2a(0,0,0)$, $6b(0.5,0.5,0)$, $8c(0.25,0.25,0.25)$ and $24g(x,y,0)$ Wyckoff positions, respectively.^{1,2} The factor-group analysis of the Γ -point optical phonons gives the following irreducible representation: $11F_u \oplus 2E_u \oplus 2A_u \oplus 2E_g \oplus 2A_g \oplus 4F_g$.^{3,4} The F_u modes are IR-active, the E_g , F_g and A_g modes are Raman-active, and the remaining E_u and A_u modes are silent. In the ferroelectric phase, assuming that BMCO crystallizes in the Cm space group, the Bi, Mn and 4 oxygen ions are in the $2a(x,0,z)$ Wyckoff position, while the Cr and the remaining 8 oxygen ions occupy the $4b(x,y,z)$ one.² Therefore, the optical modes have symmetries $15A' \oplus 12A''$ and are both IR- and Raman-active.^{3,4} There is a group-subgroup relation between the T_h and C_s point groups of the paraelectric and ferroelectric phases, and therefore, a continuous ferroelectric phase transition is possible.⁵ The proper ferroelectric polarization lies along the z -axis, the improper ferroelastic deformations u_{xx} , u_{yy} and u_{zz} are allowed and 6 types of ferroelectric domains are possible.⁵

Magnetic Studies

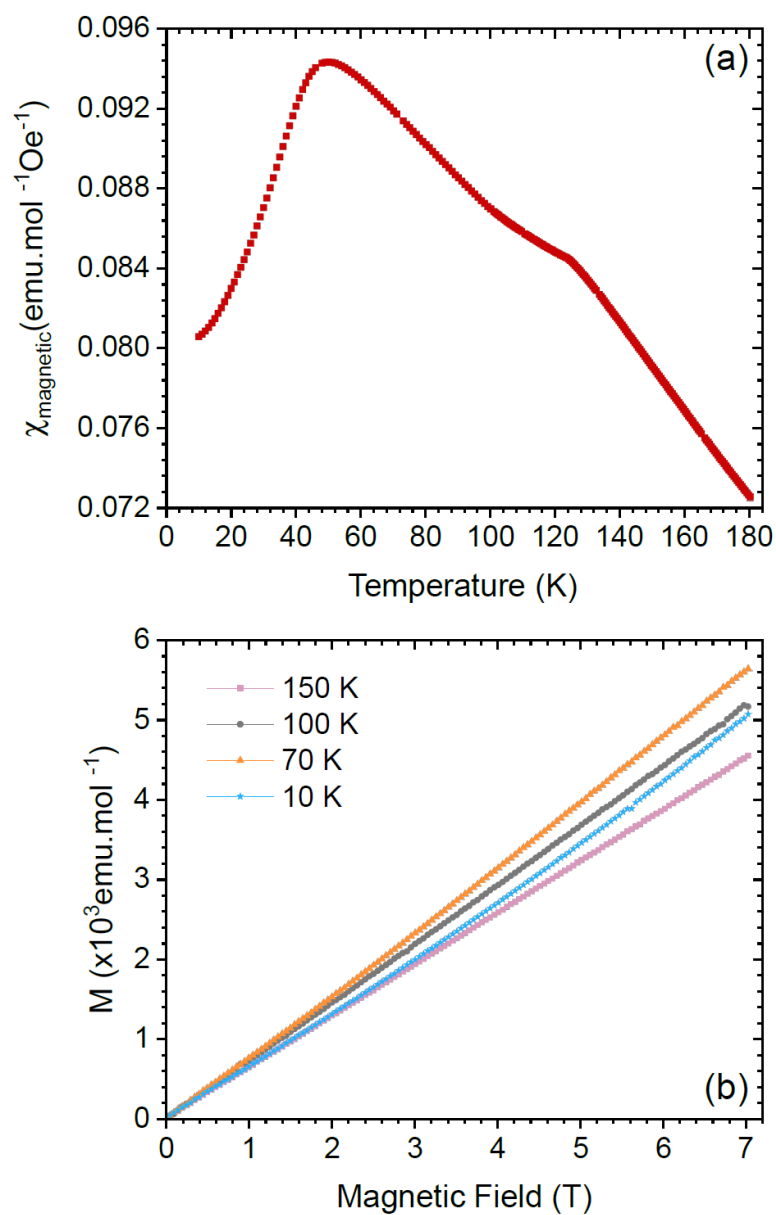


Figure S2. (a) Temperature dependence of the magnetic susceptibility of $\text{BiMn}_3\text{Cr}_4\text{O}_{12}$, measured under an applied magnetic field of 1 T. (b) Magnetic field dependence of the magnetization, measured at several temperatures. Magnetization is linearly dependent on magnetic field roughly up to 2 T, therefore $\chi_{\text{magnetic}} = M/H$ in that range.

Polar and Dielectric Studies

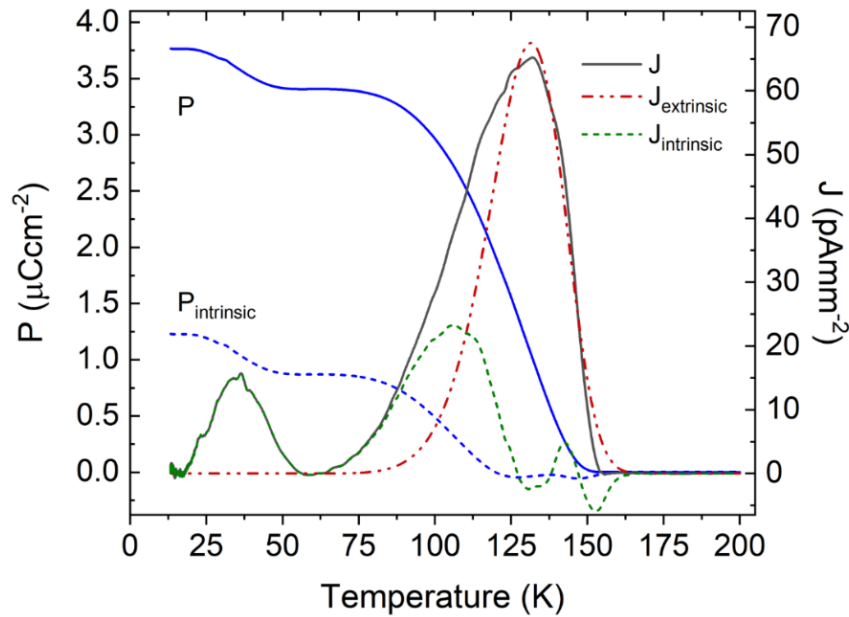


Figure S3. Temperature dependence of the thermally stimulated depolarization current (TSDC) density (right axis), measured with a heating rate of 0.5 Kmin^{-1} after cooling with a poling electric field of 5.7 kVcm^{-1} . The TSDC is decomposed by fitting the extrinsic component using Equation 3 in the 125–200 K temperature range (see main text). The intrinsic ferroelectric polarization, $P_{intrinsic}$, was calculated by integrating in time the low-temperature (green) component, $J_{intrinsic}$. The total “polarization” P , including both intrinsic and extrinsic contributions, is plotted by solid blue line.

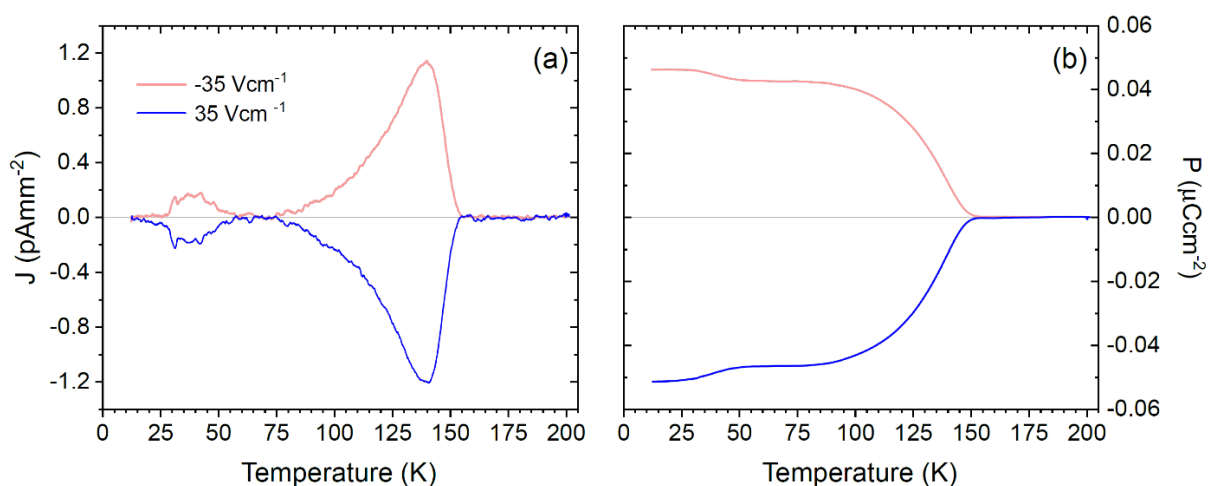


Figure S4. Temperature dependence of (a) pyro-current density and (b) polarization measured after poling with electric fields of $\pm 35 \text{ Vcm}^{-1}$, applied on cooling below 200 K. Note that even a small electric field can partially switch the polarization.

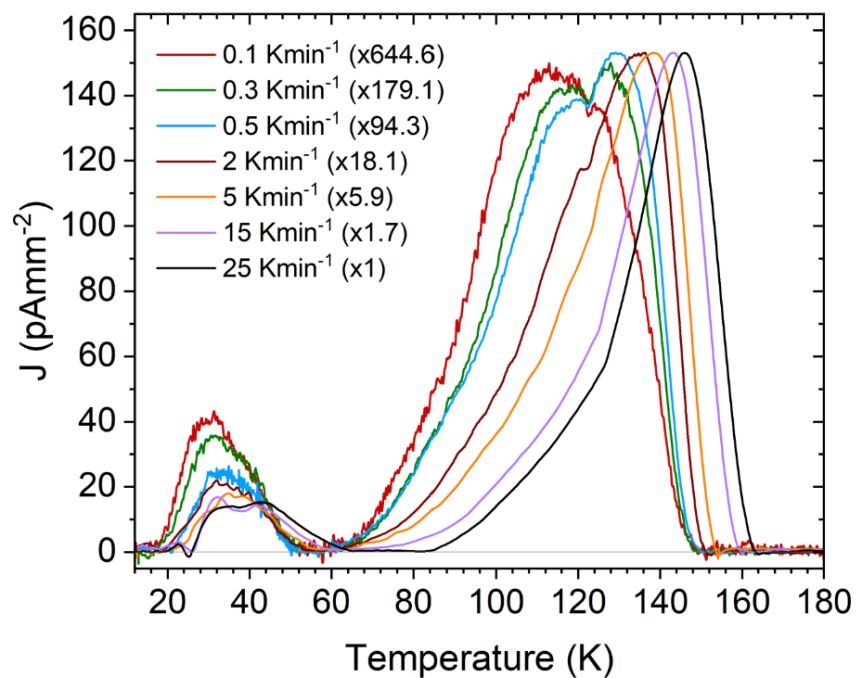


Figure S5. Temperature dependence of the TSDC density of $\text{BiMn}_3\text{Cr}_4\text{O}_{12}$ measured at several heating rates with a poling electric field of 0.7 kVcm^{-1} . For clarity, the curves were each multiplied by the factor indicated in the legend. The odd shape of the peak near 40 K in the current measured at 25 Kmin^{-1} is caused by instabilities in the temperature ramp below 60 K.

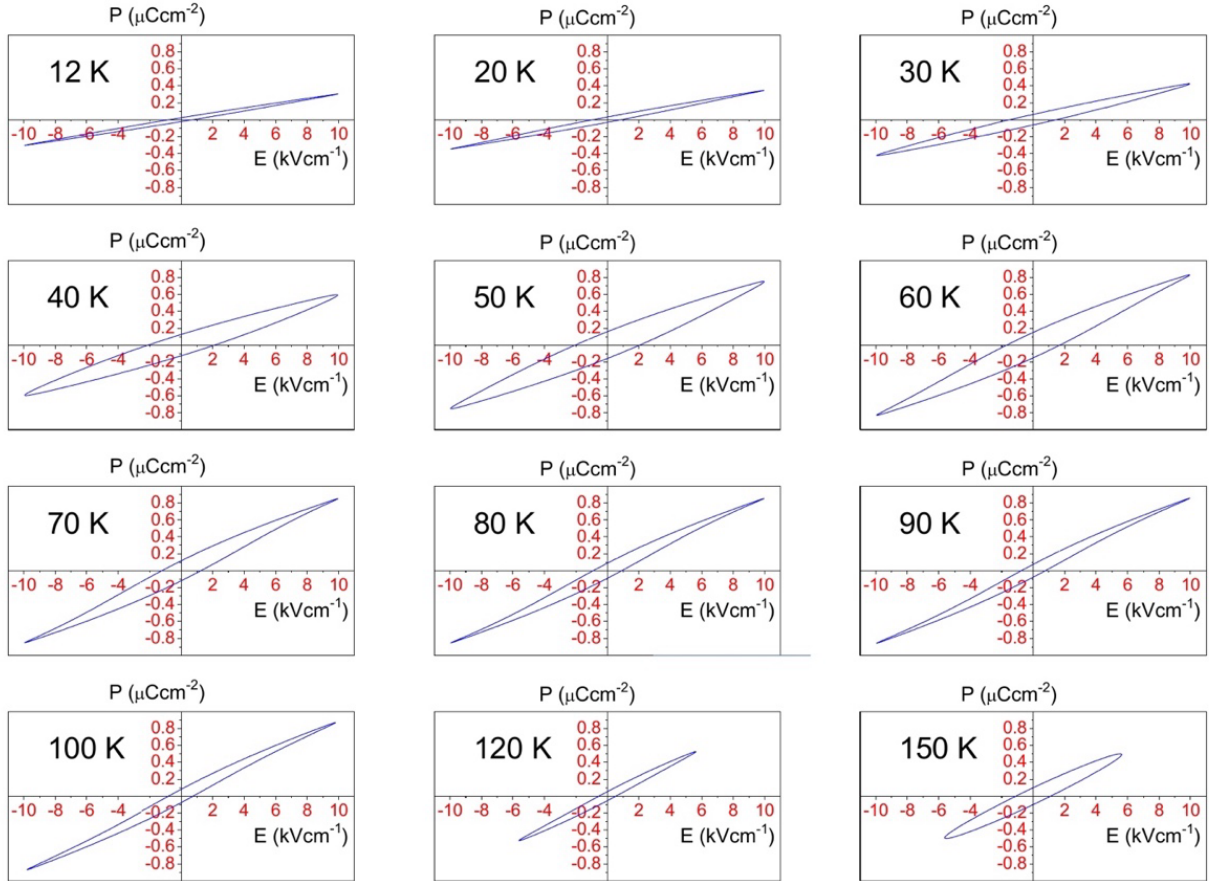


Figure S6. $P(E)$ hysteresis loops at various temperatures taken at 50 Hz. A lossy loop is seen in the paraelectric phase at 150 K, ferroelectric hysteresis loops develop below 120 K. The coercive field, E_c , and remnant polarization, P_r , increase on cooling from 120 K and then decrease below 50 K, as the maximum applied field of 10 kVcm^{-1} becomes insufficient to induce a single domain state. It was not possible to apply a higher field because the sample becomes leaky. For the same reason, the maximum applied field is lower above 100 K.

In the 30 – 70 K range, both $\epsilon'(T)$ and $\epsilon''(T)$ exhibit a frequency dependent behavior. Such behavior can be explained by a dielectric relaxation with the mean relaxation frequency, f_R , corresponding to the frequency-dependent peak in $\epsilon''(T)$ (see inset of Figure S7). The temperature dependence of the relaxation time, $\tau = 1/2\pi f_R$, in $\text{BiMn}_3\text{Cr}_4\text{O}_{12}$ is shown in Figure S7. The relaxation time follows the Arrhenius law, $\tau(T) = \tau_L \exp(U/k_B T)$, where τ_L is a pre-exponential factor and U is the activation energy. The relaxation describes most probably the thermally activated motion of ferroelectric domain walls in the ferroelectric phase.⁶ The activation energy, $U \approx 73$ meV, has a similar value to what has been reported for other ferroelectrics.⁶⁻⁸

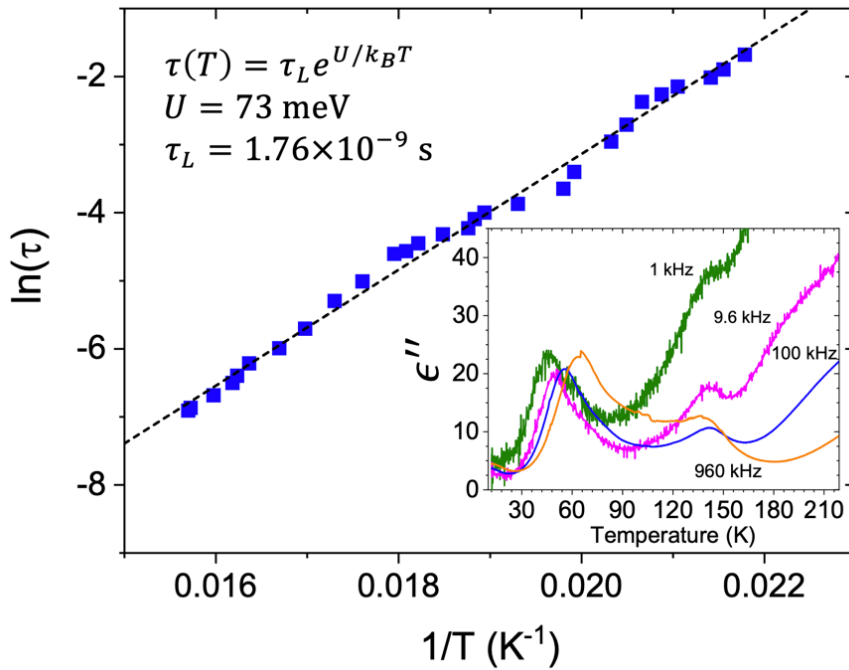


Figure S7. Temperature dependence of the relaxation time, τ , in $\text{BiMn}_3\text{Cr}_4\text{O}_{12}$. The fit with the Arrhenius law is shown as a dashed line. Inset: temperature dependence of the imaginary part of the permittivity measured at selected frequencies.

Infrared Spectra

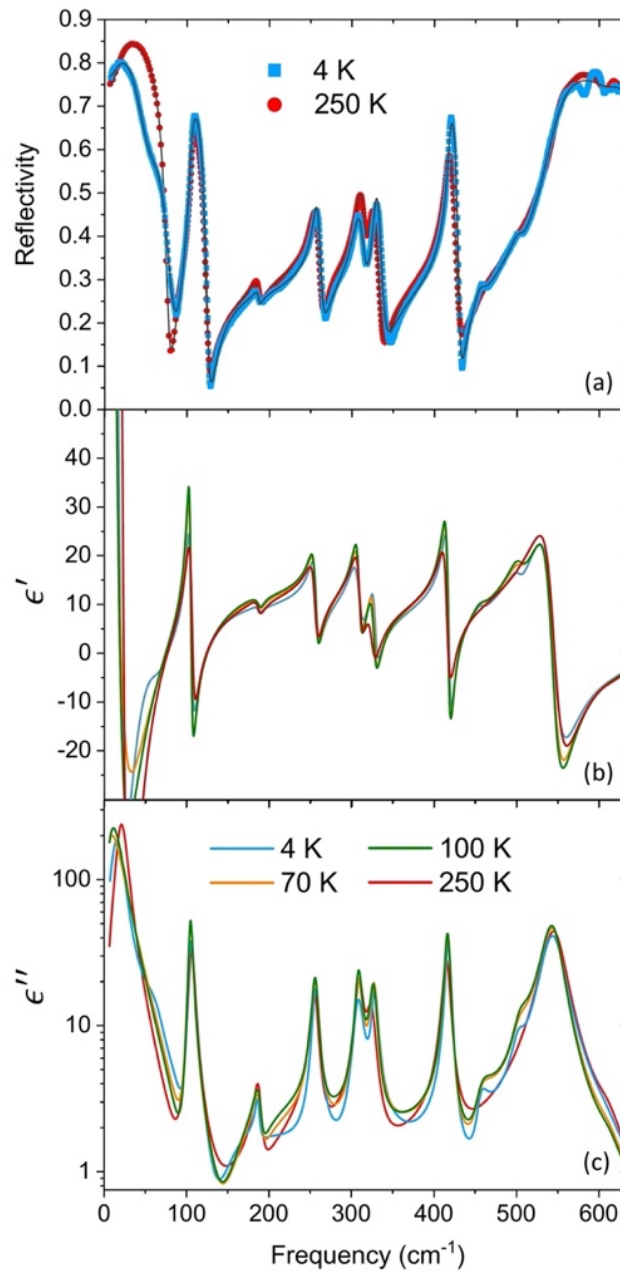


Figure S8. (a) IR reflectivity spectra of BiMn₃Cr₄O₁₂ at 4 K and 250 K. The fits of Equation 4 to the reflectivity spectra are shown as dotted lines. (b) ϵ' and (c) ϵ'' (in logarithmic scale) spectra obtained from fitting the IR reflectivity at several temperatures.

Table SI. Parameters of the IR-active modes in BiMn₃Cr₄O₁₂ obtained from the fits of IR reflectivity using Equation 3 and 4. All modes have F_u symmetry in the paraelectric phase. The values predicted from first-principles calculations in the paraelectric phase by Dai et al. are also provided.³ The oscillator strength, $S_j = \Delta\epsilon_j\omega_{TOj}^2$, is in cm⁻², while all the other parameters are in cm⁻¹.

4 K					250 K					Theory
ω_{TO}	γ_{TO}	ω_{LO}	γ_{LO}	$S (\times 10^4)$	ω_{TO}	γ_{TO}	ω_{LO}	γ_{LO}	$S (\times 10^4)$	ω_{TO}
18.7	21.6	85.2	21.9	6.73	22.3	16.3	77.6	9.6	8.16	30.74
71.5	33.4	78	26.1	3.03	72	182.9	71.6	200	0.02	–
78.5	70.3	51	38.4	0.16	–	–	–	–	–	–
105.1	7.2	125.9	7.2	4.88	106.1	8.4	125.0	9.8	2.48	106.28
186.7	5.9	187.1	5.6	0.05	187.5	10.0	188.8	8.8	0.28	180.70
256.7	9.0	263.3	10.1	3.06	255.5	10.4	261.6	9.5	3.10	250.24
308.1	13.4	315.1	15.1	4.95	309.6	10.6	314.9	11.9	4.65	300.01
328.2	8.6	337.5	13.7	3.55	324.5	13.1	334.5	11.6	3.90	313.76
417.7	7.4	430.6	6.7	10.51	415.5	10.6	428.5	11.5	10.34	416.47
456.0	15.2	457.0	17.6	0.76	–	–	–	–	–	425.12
503.1	17.2	504.5	17.4	2.70	–	–	–	–	–	–
544.0	32.6	614.0	39.9	68.70	545.7	33.0	611.0	35.1	71.85	574.50
614.4	38.0	676.5	156.0	0.24	612.5	33.6	676.5	156	1.04	590.81
686.0	144.0	701.5	19.5	0.71	686.0	144.0	701.5	19.0	0.74	614.86

Raman Spectra

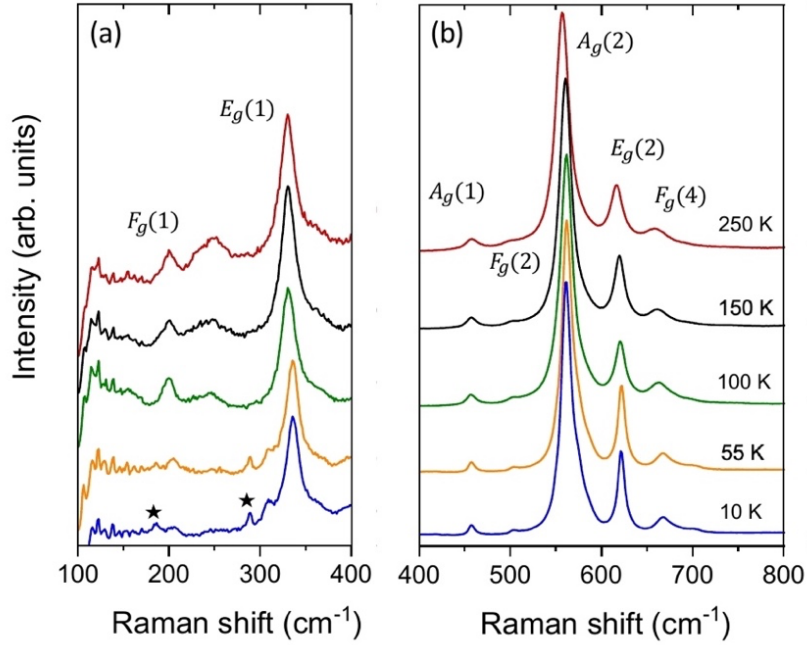


Figure S9. Unpolarized Raman spectra of $\text{BiMn}_3\text{Cr}_4\text{O}_{12}$ measured at several temperatures in the (a) $100 - 400 \text{ cm}^{-1}$ and (b) $400 - 800 \text{ cm}^{-1}$ spectral range. The spectra have been shifted and the vertical scales in panels (a) and (b) are different for clarity. The $F_g(3)$ mode near 570 cm^{-1} , is screened by the $A_g(2)$ mode. The modes marked by a star arise from BiCrO_3 impurities.⁹

Table SII. Frequencies of the Raman-active modes in $\text{BiMn}_3\text{Cr}_4\text{O}_{12}$. The symmetries in the paraelectric phase are indicated. The values predicted from first-principles calculations in the paraelectric phase by Dai et al. are also provided.³ All values are expressed in cm^{-1} .


Symmetry ($T > T_{FE1}$)	10 K	250 K	Theory
$F_g(1)$	199.8	199.7	181.59
?	246	243.5	—
$E_g(1)$	331.6	330.2	309.88
$A_g(1)$	459.7	458.2	428.45
$F_g(2)$	494.2	495.8	513.94
$A_g(2)$	564.4	564.4	556.35
$F_g(3)$	570.0	—	576.26
$E_g(2)$	624.5	622.9	613.45
$F_g(4)$	664.1	661.2	663.02

References

1. Zhou, L. *et al.* Realization of Large Electric Polarization and Strong Magnetoelectric Coupling in $\text{BiMn}_3\text{Cr}_4\text{O}_{12}$. *Adv. Mater.* **29**, 1703435 (2017).
2. Dai, J. Q. & Zhang, C. C. Ferroelectricity driven by soft phonon and spin order in multiferroic $\text{BiMn}_3\text{Cr}_4\text{O}_{12}$. *J. Am. Ceram. Soc.* **102**, 6048–6059 (2019).
3. Dai, J. Q., Liang, X. L. & Lu, Y. S. Electronic structure, lattice dynamics, and dielectric properties in cubic perovskite $\text{BiMn}_3\text{Cr}_4\text{O}_{12}$ and $\text{LaMn}_3\text{Cr}_4\text{O}_{12}$. *Chem. Phys.* **538**, 110924 (2020).
4. Rousseau, D. L., Bauman, R. P. & Porto, S. P. Normal mode determination in crystals. *J. Raman Spectrosc.* **10**, 253-290 (1981).
5. Janovec, V., Dvořák, V. & Petzelt, J. Symmetry classification and properties of equi-translation structural phase transitions. *Czechoslov. J. Phys.* **25**, 1362-1396 (1975).
6. Kamba, S. *et al.* Unusual ferroelectric and magnetic phases in multiferroic 2H- BaMnO_3 ceramics. *Phys. Rev. B* **95**, 174103 (2017).
7. Kamba, S. *et al.* Dielectric dispersion of the relaxor PLZT ceramics in the frequency range 20 Hz – 100 THz. *J. Phys. Condens. Matter* **12**, 497 (2000).
8. Han, H. *et al.* Origin of colossal permittivity in BaTiO_3 via broadband dielectric spectroscopy. *J. Appl. Phys.* **113**, 024102 (2013).
9. Araújo, B. S. *et al.* Spin-phonon coupling in monoclinic BiCrO_3 . *J. Appl. Phys.* **127**, 114102 (2020).

A.2 Two displacive ferroelectric phase transitions in multiferroic quadruple perovskite $\text{BiMn}_7\text{O}_{12}$

The paper “Two displacive ferroelectric phase transitions in multiferroic quadruple perovskite $\text{BiMn}_7\text{O}_{12}$ ”, Ref.^{A2}, is presented in this section.

Two displacive ferroelectric phase transitions in multiferroic quadruple perovskite BiMn₇O₁₂A. Maia¹, M. Kempa¹, V. Bovtun¹, R. Vilarinho², C. Kadlec¹, J. Agostinho Moreira², A. A. Belik³, P. Proschek⁴, and S. Kamba^{1,*}¹*Institute of Physics of the Czech Academy of Sciences, Na Slovance 2, 182 00 Prague 8, Czech Republic*²*IFIMUP, Physics and Astronomy Department, Faculty of Sciences, University of Porto, Rua do Campo Alegre 687, s/n 4169-007 Porto, Portugal*³*Research Center for Materials Nanoarchitectonics (MANA), National Institute for Materials Science (NIMS), Namiki 1-1, Tsukuba, Ibaraki 305-0044, Japan*⁴*Faculty of Mathematics and Physics, Charles University, Ke Karlovu 5, 121 16 Prague, Czech Republic* (Received 19 December 2023; revised 17 February 2024; accepted 1 April 2024; published 25 April 2024)

We report on the microwave, terahertz (THz), infrared, and Raman spectroscopic studies of BiMn₇O₁₂ ceramics, shedding more light onto the nature of two structural phase transitions and their possible relation with ferroelectricity in this compound. We observed a softening of one polar phonon in the THz range on cooling towards 460 and 300 K, i.e., temperatures at which BiMn₇O₁₂ undergoes subsequent structural phase transitions from monoclinic *I2/m* to polar monoclinic *Im* and triclinic *P1* phases. The soft phonon causes dielectric anomalies typical for displacive ferroelectric phase transitions. Microwave measurements performed at 5.8 GHz up to 400 K qualitatively confirmed not only the dielectric anomaly at 300 K, but also revealed two other weak dielectric anomalies near the magnetic phase transitions at 60 and 28 K. This evidences the multiferroic nature of the low-temperature phases, although the relatively high conductivity in the kHz and Hz spectral range prevented us from directly measuring the permittivity and ferroelectric polarization. Some Raman modes sense the magnetic phase transitions occurring near 60 and 25 K, showing that spin-phonon coupling is relevant in this compound and in this temperature range. The deviation of the Mn-O stretching mode frequency from the anharmonic temperature behavior was successfully explained by the spin correlation function calculated from the magnetic contribution to the specific heat.

DOI: [10.1103/PhysRevB.109.134111](https://doi.org/10.1103/PhysRevB.109.134111)

I. INTRODUCTION

A-site ordered quadruple perovskites, AA₃B₄O₁₂, exhibit several interesting physical and chemical properties [1,2], such as reentrant structural transitions [3], intersite charge transfer and disproportionation [2], giant dielectric constant [4,5], multiferroicity [6,7], and high catalytic activity [8]. AA₃B₄O₁₂ has a 12-fold-coordinated A site and a square-planar-coordinated A' site, while B sites have the usual octahedral coordination for perovskites. For manganese, it is possible to have A' = B, and the composition can be written as AMn₇O₁₂ in brief. These manganites can have spin, orbital, and charge degrees of freedom depending on the oxidation state of the A cation [1,3,6,9–12].

The quadruple perovskite BiMn₇O₁₂ exhibits three structural and two magnetic phase transitions [13]. Above $T_1 = 608$ K, BiMn₇O₁₂ crystallizes in a parent cubic structure, with space group *Im* $\bar{3}$. Between 460 and 608 K, BiMn₇O₁₂ adopts a monoclinic symmetry, with pseudo-orthorhombic metrics [denoted as *I2/m(o)*], and orbital order appears below T_1 . At $T_2 = 460$ K, BiMn₇O₁₂ undergoes a phase transition into a polar monoclinic structure, described by the *Im* space group. Finally, at $T_3 = 290$ K, a triclinic distortion takes

place and BiMn₇O₁₂ transits into another polar structure, described by the *P1* space group (assigned as *I1* in Ref. [14]). Structural analyses of BiMn₇O₁₂ are challenging because of severe domain twinning in single crystals, and anisotropic broadening and diffuse scattering in powder [13]. However, first-principles calculations confirm that noncentrosymmetric structures are more stable than centrosymmetric ones [13]. The energy difference between the *Im* and *P1* models is very small, and this fact can explain why the *Im* to *P1* transition is very gradual, and there are no differential scanning calorimetry (DSC) anomalies associated with this transition [13]. The crystal structure and phase sequence of BiMn₇O₁₂ are illustrated in Fig. 1.

In earlier studies, BiMn₇O₁₂ has been shown to exhibit two magnetic phase transitions at 55 and 25 K [16,17]. Recent magnetic and powder neutron diffraction experiments revealed three successive magnetic phase transitions [18]. Below $T_{N1} = 59$ K, B-site Mn cations order antiferromagnetically with propagation vector $\mathbf{k}_1 = (0.5, 0, -0.5)$, and at $T_{N2} = 55$ K the A'-site Mn spins order ferrimagnetically with $\mathbf{k}_2 = (0, 0, 0)$ [18]. Both magnetic orderings coincide down to $T_{N3} = 27$ K, below which both the A'-site and B-site spins reorient with modulation vector $\mathbf{k}_3 = (0, 1, 0)$. It should be noted that, in contrast to other type II multiferroics, the polar distortion of the lattice in the *P1* structure of BiMn₇O₁₂ stabilizes the E-type magnetic ordering of Mn at the B-site

*kamba@fzu.cz

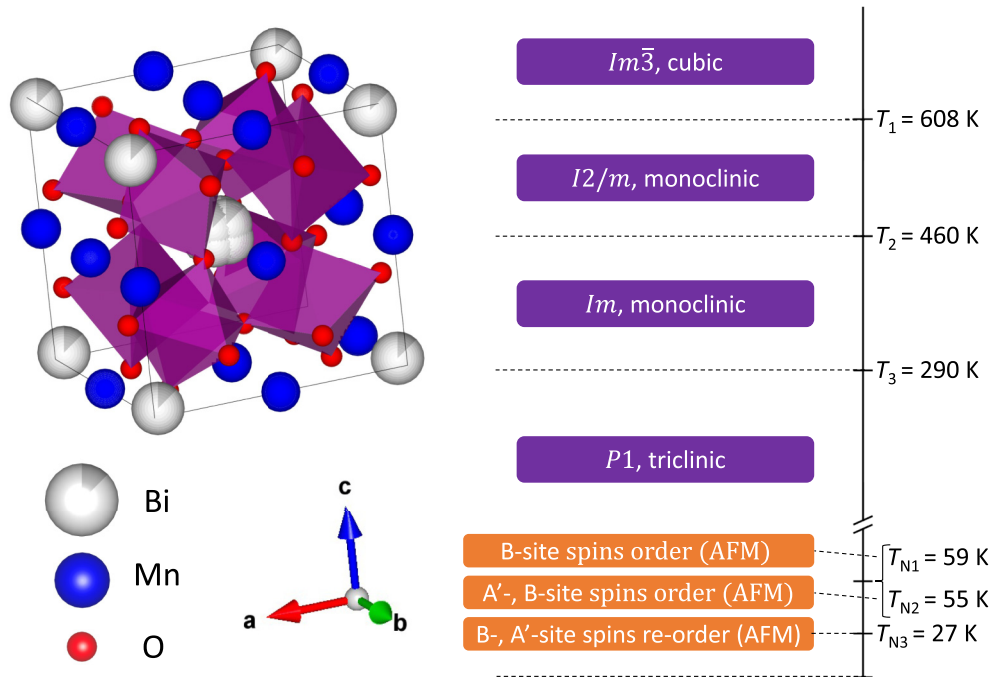


FIG. 1. Crystal structure of $\text{BiMn}_7\text{O}_{12}$ at room temperature and schematic representation of its structural (purple) and magnetic (orange) phase sequence. The illustration of the crystal structure was obtained using VESTA software [15].

perovskite positions due to trilinear coupling of two magnetic order parameters η_1 , η_2 and polarization P , i.e., $\eta_1\eta_2P$ [18]. Conversely, in $\text{BiMn}_3\text{Cr}_4\text{O}_{12}$, a different mechanism should be responsible for stabilizing the magnetic structure (probably with a quadratic coupling η^2P or ηP^2), because in this material only the Cr spins order below $T_N = T_{\text{FE}}$ [7]. Magnetoelectric coupling should be induced in both materials via inverse exchange striction ($\propto S_i \cdot S_j$). The magnetic phase sequence and the crystal structure are depicted in Fig. 1 [16–18].

The relation between the local crystal structure and the spontaneous electric polarization in $\text{BiMn}_{6.96}\text{Fe}_{0.04}\text{O}_{12}$ was recently studied using ^{57}Fe probe Mössbauer spectroscopy [19,20]. A “dynamic” Born charge model was used to develop an algorithm to construct the temperature dependence of the polarization of the crystal using structural data of the compound and the experimental values of the quadrupole splittings of the Mössbauer spectra of the ^{57}Fe probe atoms [19]. The temperature dependence of the electric polarization obtained from the Mössbauer data points out for a paraelectric to ferroelectric first-order phase transition with $T_c \approx 437$ K, close to the $I2/m$ to Im structural transition temperature T_2 , as well as a considerable increase in the electric polarization below 270 K, with extrapolated $T^* \approx 294$ K, close to the Im to $P1$ structural transition at T_3 [19]. It has also been demonstrated that light hole doping of $\text{BiMn}_7\text{O}_{12}$ with Cu ($\text{BiCu}_{0.1}\text{Mn}_{6.9}\text{O}_{12}$) can induce incommensurate helical ordering of electric dipoles [21].

Despite $\text{BiMn}_7\text{O}_{12}$ structural and magnetic properties being extensively studied in the recent past, its dielectric and possible ferroelectric properties have not yet been published due to its relatively high conductivity above 100 K. $\text{BiMn}_7\text{O}_{12}$ is sufficiently resistive to perform permittivity measurements only below 90 K, revealing dielectric anomalies at magnetic phase transitions [22,23]. This evidences for

magnetodielectric coupling and the possible multiferroic nature of the low temperature magnetic phases. However, direct electric polarization measurements have not yet been published due to the impossibility of applying a sufficiently high electric field in the measurement of ferroelectric hysteresis loops, and of poling the sample in the paraelectric phase for pyroelectric current studies, due to its high conductivity.

Spectroscopic methods that are insensitive to the conductivity of the sample are used to uncover the nature of structural and possible ferroelectric phase transitions in $\text{BiMn}_7\text{O}_{12}$. That is why we have undertaken a comprehensive temperature dependent heat capacity, infrared, THz, Raman, and microwave measurements in a broad temperature range, revealing a ferroelectric soft mode driving both ferroelectric phase transitions near 460 and 290 K, and optical phonons showing anomalies near magnetic phase transitions. In addition, we also observed dielectric anomalies at two magnetic phase transitions, indicative of magnetoelectric coupling in multiferroic phases.

II. EXPERIMENTAL DETAILS

$\text{BiMn}_7\text{O}_{12}$ polycrystalline samples were synthesized under high-pressure and high-temperature conditions from stoichiometric mixtures of Bi_2O_3 and Mn_2O_3 starting reagents, as detailed in Ref. [13]. Laboratory powder x-ray diffraction (XRD) data were taken at room temperature using a MiniFlex600 diffractometer with $\text{CuK}\alpha$ radiation (2θ range $10\text{--}80^\circ$, a step width of 0.02° , and a counting speed of $1^\circ/\text{min}$). XRD data were analyzed by the Rietveld method with RIETAN-2000 program [24]. Weight fractions of impurities were estimated by RIETAN-2000 from refined scale factors. The best ceramics contained some impurities, specifically 1% of $\text{Bi}_2\text{O}_2\text{CO}_3$ and 1% Mn_2O_3 . The ceramic disks with diameter 6 mm had thickness 1–2 mm. Scanning electron

microscope images of BiMn₇O₁₂ ceramics revealed grains with the size 2–5 μm (see Fig. S1 in the Supplemental Material [25]). The microwave response at 5.8 GHz was measured using the composite dielectric resonator method [27,28]. The TE_{01δ} resonance frequency, quality factor, and insertion loss of the base cylindrical dielectric resonator with and without the sample were recorded during heating from 10 to 400 K with a temperature rate of 0.5 K/min in a Janis closed-cycle He cryostat. The sample without electrodes (2 × 2 mm plate, 0.32 mm thick) was placed on top of the base dielectric resonator. The resonators were measured in the cylindrical shielding cavity using the transmission setup with a weak coupling by an Agilent E8364B network analyzer. The complex refractive index $n = \sqrt{\epsilon\mu}$ of the sample(s) was calculated from the acquired resonance frequencies and quality factors of the base and composite resonators.

The magnetic properties were measured via vibrating sample magnetometer (VSM, Quantum Design) using a Quantum Design physical properties measurement system (PPMS) in various temperature ranges (down to 2 K) and magnetic field (up to 9 T). The heat capacity measurements were performed by using the heat capacity option in the PPMS in various ranges of temperature (down to 2 K).

The THz complex transmittance was measured using a custom-made time-domain spectrometer powered by a Ti:sapphire femtosecond laser with 35-fs-long pulses centered at 800 nm. The system is based on coherent generation and subsequent coherent detection of ultrashort THz transients. The detection scheme consists of an electro-optic sampling of the electric field of the transients within a 1-mm-thick, (110)-oriented ZnTe crystal as a sensor [29]. This allows measuring the time profile of the THz transients transmitted through the sample. The BiMn₇O₁₂ sample was highly absorbing in the THz region due to a strong optical soft mode, therefore we glued it on a sapphire substrate and polished it down to 38 μm. The bare sapphire substrate (thickness 0.543 mm) was measured as a reference.

Low-temperature unpolarized IR reflectivity measurements of one-sided optically polished ceramics (thickness ~1.5 mm) were performed using a Bruker IFS-113v Fourier-transform IR spectrometer equipped with a liquid-He-cooled Si bolometer (1.6 K) serving as a detector. For both the THz complex transmittance and IR reflectivity measurements, the temperature control was done through an Oxford Instruments Optistat optical continuous He-flow cryostats with mylar and polyethylene windows, respectively. A commercial high-temperature cell Specac P/N 5850 was used for IR and THz studies above room temperature. The samples were heated in vacuum up to 580 K. We were concerned about heating the samples to higher temperatures to prevent degradation of the samples. The IR spectra were fitted using one Lorentz oscillator for each phonon mode. The complex dielectric function is given by

$$\epsilon(\omega) = \epsilon_\infty + \sum_j \frac{\Delta\epsilon_j \omega_{0j}^2}{\omega_{0j}^2 - \omega^2 - i\gamma_j \omega}, \quad (1)$$

where ϵ_∞ is the contribution from electronic transitions to the dielectric function, and the j th phonon is described by an eigenfrequency ω_{0j} , an oscillator strength $\Delta\epsilon_j$, and

damping γ_j . These parameters were fitted so that the reflectivity at normal incidence, given by $R(\omega) = \left| \frac{\sqrt{\epsilon(\omega)} - 1}{\sqrt{\epsilon(\omega)} + 1} \right|^2$, matches the experimental data. The eigenfrequencies ω_{0j} correspond to the transverse optical phonon frequencies. The high-frequency permittivity ϵ_∞ was obtained from the room-temperature frequency-independent reflectivity tail above the phonon frequencies and was assumed temperature independent.

Unpolarized Raman spectra were recorded using a Renishaw inVia Qontor spectrometer with a 785-nm linearly polarized diode-pumped laser and an edge filter. Measurements were done at fixed temperatures from 10 to 600 K using a THMS600 Linkam stage cooled by a nitrogen flow down to 80 K and a custom-made closed-cycle helium cryostat down to 10 K. The laser power (2.3 mW) was chosen adequately to prevent heating the sample. The wave number at a given temperature $\omega(T)$ of each Raman mode is obtained by the best fit of the Raman spectra with a sum of damped oscillators [30]:

$$I(\omega, T) = [1 + n(\omega, T)] \sum_j \frac{A_{0j} \Omega_{0j}^2 \Gamma_{0j} \omega}{(\Omega_{0j}^2 - \omega^2)^2 + \Gamma_{0j}^2 \omega^2}, \quad (2)$$

where $n(\omega, T)$ is the Bose-Einstein factor and A_{0j} , Ω_{0j} , Γ_{0j} are the strength, wave number, and damping coefficient of the j th oscillator, respectively. In the temperature range where no anomalous behavior is observed, the temperature dependence of the wave number of the phonon frequencies is well described by the normal anharmonic temperature effect due to volume contraction as temperature decreases [31]:

$$\omega(T) = \omega_0 + C \left[1 + \frac{2}{e^x - 1} \right] + D \left[1 + \frac{3}{e^y - 1} + \frac{3}{(e^y - 1)^2} \right] \quad (3)$$

with $x \equiv \hbar\omega_0/2k_B T$, $y \equiv \hbar\omega_0/3k_B T$, and where ω_0 , C , and D are model constants, \hbar is the reduced Planck constant, and k_B is the Boltzmann constant.

Deviations to the normal anharmonic temperature effect were interpreted on the basis of the spin-phonon coupling as [32]

$$\Delta\omega(T) = \omega(T) - \omega_0 \propto \frac{\partial^2 J}{\partial u^2} \langle \mathbf{S}_i \cdot \mathbf{S}_j \rangle \approx R \langle \mathbf{S}_i \cdot \mathbf{S}_j \rangle \quad (4)$$

where J is the magnetic exchange integral, u is the normal coordinate of the vibrational mode, and R is the difference of the second derivatives of the ferro- and antiferromagnetic exchange integrals with respect to the normal coordinate, where the approximation assumes the same spin correlation function, $\langle \mathbf{S}_i \cdot \mathbf{S}_j \rangle$, for both.

III. RESULTS AND DISCUSSION

A. Polar soft phonon in the THz range

Figures 2(a) and 2(b) show the real and imaginary parts of the complex dielectric spectra, $\epsilon'(\omega)$ and $\epsilon''(\omega)$ of BiMn₇O₁₂, respectively, measured at several fixed temperatures in the THz spectral range. At 580 K, only one polar phonon is observed at 28 cm⁻¹. As the temperature decreases towards $T_2 = 460$ K, the phonon frequency shifts towards lower frequencies, while the static permittivity increases, and on further

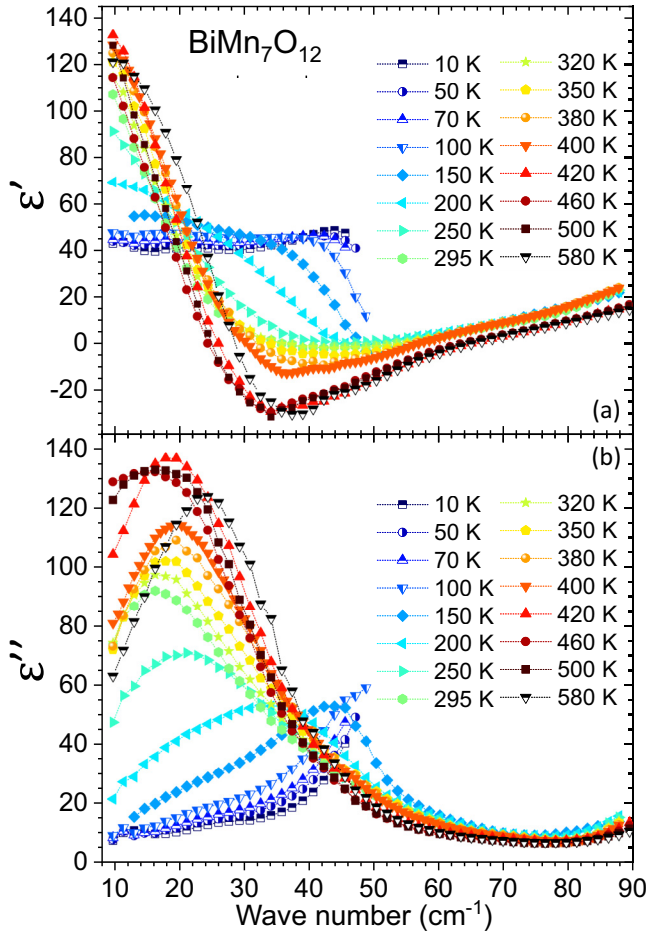


FIG. 2. (a) $\varepsilon'(\omega)$ and (b) $\varepsilon''(\omega)$ spectra of $\text{BiMn}_7\text{O}_{12}$ obtained by THz time-domain spectroscopy at several temperatures.

cooling to 380 K, the phonon hardens. This temperature behavior is typical of a polar soft phonon driving a displacive ferroelectric phase transition. Below 380 K, the phonon softens once again down to 300 K. This phonon anomaly at 300 K is in the vicinity of the structural phase transition from the *Im* to *P1* structure, in which the ferroelectric polarization is predicted to move out of the *ac* plane [18]. Below 300 K, the phonon frequency smoothly increases down to 10 K. This behavior is best seen in the temperature dependence of the soft mode wave number and its dielectric strength, depicted in Figs. 3(a) and 3(b), respectively. The dielectric strength of the soft phonon, $\Delta\varepsilon_{\text{SM}}(T)$, considerably increases on cooling from 580 K towards 460 K [see Fig. 3(b)] due to the conservation law of the oscillator strength $f_j = \Delta\varepsilon_j(T)\omega_{0j}^2(T) = \text{const}$ (valid for all uncoupled polar phonons, including the soft mode). It is noteworthy that at 580 K, $\Delta\varepsilon_{\text{SM}}$ constitutes approximately 90% of the static electric permittivity in the THz range: $\varepsilon_0 = \varepsilon_\infty + \sum_j \Delta\varepsilon_j$. Cooling from 380 K, $\Delta\varepsilon_{\text{SM}}(T)$ decreases and exhibits a broad plateaulike behavior down to 300 K, below which it smoothly decreases down to 20% of the static electric permittivity at the lowest measured temperature.

The temperature dependence of the relative changes of real and imaginary parts of the dielectric permittivity measured at

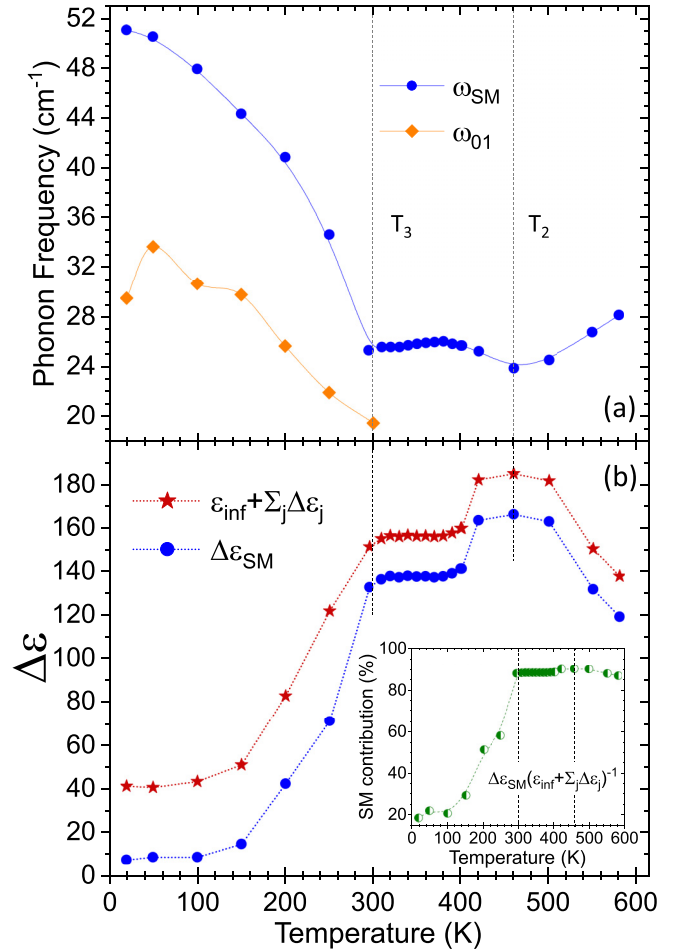


FIG. 3. (a) Temperature dependence of the frequency of two components of the soft mode in $\text{BiMn}_7\text{O}_{12}$, $\omega_{02} = \omega_{\text{SM}}$ and ω_{01} , where the latter is discernable only below room temperature. (b) Temperature dependence of dielectric strength of the soft mode and the sum of the contributions of all phonons to the static permittivity. The dashed lines are a guide for the eye. Inset: Contribution (in %) of the SM to the total static permittivity.

5.8 GHz, is shown in Figs. 4(a) and 4(b), respectively. A broad anomaly at 300 K is clearly visible, which is qualitatively consistent with the phonon anomaly in Fig. 3 near T_3 . Its absolute value is smaller than ε in Fig. 3, most likely due to lower accuracy of the microwave (MW) measurements, because the rectangular sample plate is much smaller than base dielectric resonator while the exact calculation of ε requires the same diameter of the cylindrical sample and base resonator [27]. The anomalies seen at magnetic phase transitions near 60 and 28 K (see also our magnetic moment measurements in Fig. S2 [25]) can come from both magnetic permeability μ and electric permittivity ε , but it should be mentioned that dielectric measurements at 100 kHz revealed similar anomalies in $\varepsilon(T)$ [23] and also in the Hz frequency range (see Fig. S3 of the Supplemental Material [25]), so we assume that the anomalies observed at low temperatures in Fig. 4 also come from $\varepsilon(T)$ and not from $\mu(T)$. The existence of dielectric anomalies at the magnetic phase transition temperatures is also in agreement with Ref. [18] which, based on a detailed analysis of

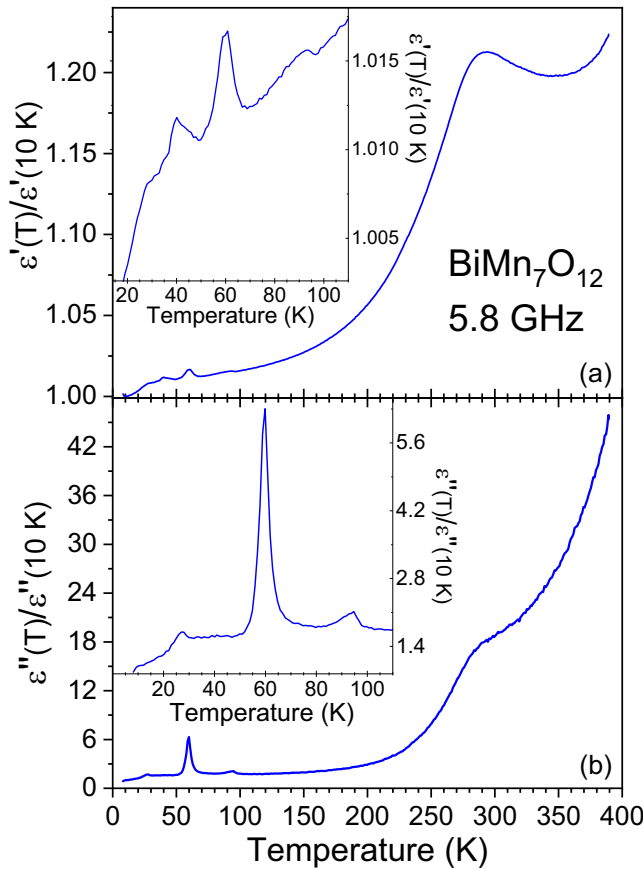


FIG. 4. Relative changes of the (a) real and (b) imaginary parts of the dielectric permittivity measured at 5.8 GHz.

neutron powder diffraction data, revealed that the magneto-electric coupling via inverse exchange striction, expressed by trilinear coupling of the order parameters, uniquely stabilizes a polar collinear magnetic structure.

It should be mentioned that the dielectric anomalies seen at the magnetic phase transitions in the temperature dependence of permittivity, both in the microwave (Fig. 4) and low-frequency spectral range (Fig. S3 [25]), are not detected in the THz spectra, as the measurements were performed each 10 K, not exactly coinciding with the temperatures of the magnetic phase transitions. Moreover, the permittivity anomalies have values of 1–2 (see Fig. S3 [25]), which are comparable to the accuracy of the THz measurements.

Unfortunately, due to the experimental limitations of our MW setup, it was not possible to measure above 400 K, so the effect of the higher temperature structural transitions (T_1 and T_2) in the MW permittivity are not ascertained [15]. The origin of the small anomaly around 95 K is unknown, but it should be noted that, at the same temperature, a small anomaly in the temperature dependence of the magnetization was observed (see Fig. S2b [25]), but no anomaly in specific heat was seen near 95 K (see Fig. 7).

B. Polar phonons

To better describe the temperature dependence of the polar soft phonon and its contribution to the total permittivity, we

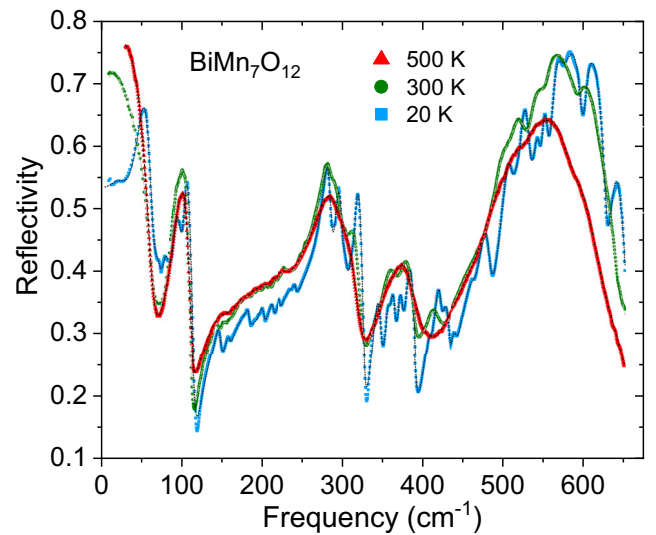


FIG. 5. Unpolarized IR reflectivity spectra of $\text{BiMn}_7\text{O}_{12}$ ceramics recorded at 20, 300, and 500 K. The corresponding fits are shown as dotted lines. The reflection band below 50 cm^{-1} corresponds to the soft mode.

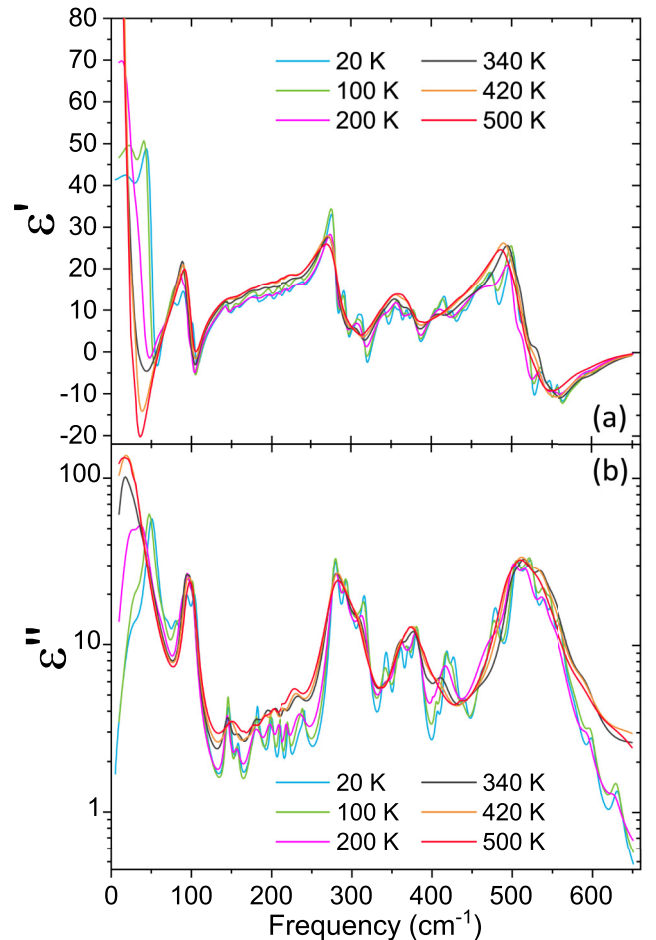


FIG. 6. (a) ϵ' and (b) ϵ'' (in logarithmic scale) spectra of $\text{BiMn}_7\text{O}_{12}$ obtained from fitting the IR reflectivity at several temperatures.

TABLE I. Factor-group analysis of the Γ -point phonons in $\text{BiMn}_7\text{O}_{12}$ [33–35]. The Wyckoff positions were taken from Ref. [13].

Temperature	Space group	IR-active modes	Raman-active modes	Silent modes	Acoustic modes
$T > T_1$	$Im\bar{3}$	$13T_u$	$3A_g \oplus 3E_g \oplus 7T_g$	$3A_u \oplus 3E_u$	$1T_u$
$T_2 < T < T_1$	$I2/m$	$19A_u \oplus 23B_u$	$13A_g \oplus 11B_g$		$1A_u \oplus 2B_u$
$T_3 < T < T_2$	Im	$32A' \oplus 25A''$	$32A' \oplus 25A''$		$2A' \oplus 1A''$
$T < T_3$	$P1$	$57A$	$57A$		$3A$

have also probed the higher energy polar lattice excitations through temperature dependent unpolarized Fourier transform infrared spectroscopy. Representative unpolarized reflectivity spectra, recorded at 20, 300, and 500 K, are shown in Fig. 5. The MIR spectrum at 300 K is shown in Fig. S4, and the fit parameters are listed in Table SI of the Supplemental Material [25]. The spectra of the real and imaginary parts of permittivity, calculated from fitting the IR reflectivity spectra using Eq. (1), are also shown in Figs. 6(a) and 6(b), respectively.

The factor-group analysis and the optical activity of phonons for the different structural phases is presented in Table I. The primitive cell contains only one formula unit $\text{BiMn}_7\text{O}_{12}$ in all crystal phases. From a symmetry point of view, 15 new polar modes and 33 new Raman modes become active due to a change of symmetry from monoclinic $I2/m$ to the lower symmetry monoclinic Im at 460 K. When changing from Im symmetry to $P1$ at 300 K, no new IR or Raman modes are expected. However, it should be emphasized that in the ferroelectric Im and $P1$ phases all phonons are both IR and Raman active.

It should be noted that the $I2/m$ structure contains 69 modes (including acoustic modes), although there are only 60 modes in the Im and $P1$ phases, at lower temperatures. This apparent discrepancy is due to the Bi cation being at Wyckoff position $8j$ with $1/4$ occupancy in the $I2/m$ phase [13], so nine more modes are allowed than at lower temperatures. According to Ref. [13], in the cubic phase the Bi cation is in the Wyckoff position $16f$ with an occupation of only $1/8$ and is therefore also predicted to have a higher number of degrees of freedom, and modes, than at lower temperatures. The partial occupation of atomic positions influences the increased damping of the corresponding phonons in the high-temperature phases.

The significant increase in the number of polar modes with cooling can be seen both in Figs. 5 and 6. Experimentally, we detected 41 IR-active modes at 20 K ($P1$ phase), 31 modes at 300 K (Im phase), and 28 modes at 500 K ($I2/m$ phase). This is below the number of modes expected from the factor-group analysis. Both the high number of modes and the temperature ranges of the phase transitions leading to a higher damping of the modes explain the lower number of detected modes. Furthermore, many of those modes can have an intensity that is below our detection limit.

The soft mode should have T_u symmetry in the cubic phase and should split in the monoclinic $I2/m$ phase below 608 K into three components with $A_u + 2B_u$ symmetries. Since $\text{BiMn}_7\text{O}_{12}$ chemically decomposes at high temperatures, it was possible to perform THz measurements only up to 580 K, when the soft mode must already be split into three components. The phonons with frequencies $\omega_{01}-\omega_{03}$ are very likely the three components of the soft mode, although the mode ω_{03} is not seen at 500 K (see Table SI [25]) due to its low strength

and strong damping and only resolves below 380 K in Im phase. The two components of the soft mode with frequencies ω_{01} and ω_{02} lie below 30 cm^{-1} , but are overlapped above T_3 , so that they can only be resolved in the $P1$ phase below 300 K, when they harden and their damping decreases with cooling (see Fig. 3).

C. Specific heat

The specific heat, divided by temperature, as a function of temperature, is shown in Fig. 7. Two anomalies are clearly observed in the temperature dependence of the specific heat at 59 and at 24 K, respectively. The temperatures at which these anomalies occur are in good agreement with the reported values of the critical temperatures of the magnetic phase transitions occurring at $T_{N1} = 59\text{ K}$ and at $T_{N3} = 23\text{ K}$, respectively, associated with the paramagnetic to the E -type antiferromagnetic ordering of the B -site Mn^{3+} spins, and a change of spin ordering of both A' - and B -site Mn sublattices. As in previous reports, the specific heat does not reveal any anomalous temperature dependence at T_{N2} nor at the structural phase transitions occurring below 300 K. The analysis of the specific heat versus temperature, by means of the fitting of Debye's equation to the experimental data, enabled us to calculate the magnetic contribution to the specific heat, shown in Fig. 7 (neglecting the electronic contribution only relevant

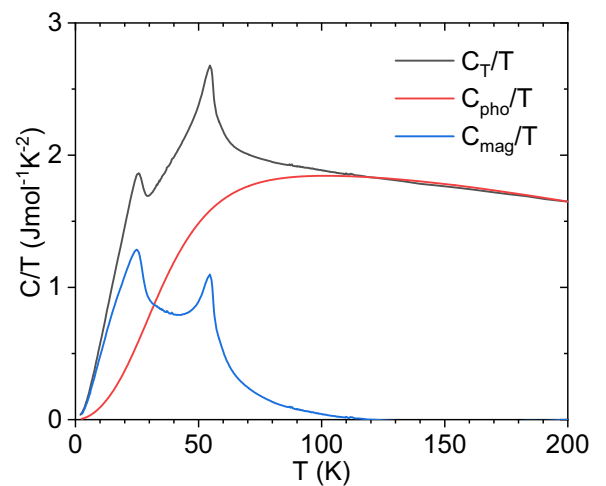


FIG. 7. Temperature dependence of the specific heat divided by temperature of $\text{BiMn}_7\text{O}_{12}$. Solid red line was determined by the best fit of Debye equation to the experimental data recorded above 120 K. Temperature dependence of the magnetic contribution to the specific heat, calculated from the difference of the experimental data and the extrapolated lattice contribution described by Debye behavior, extrapolated to 2 K.

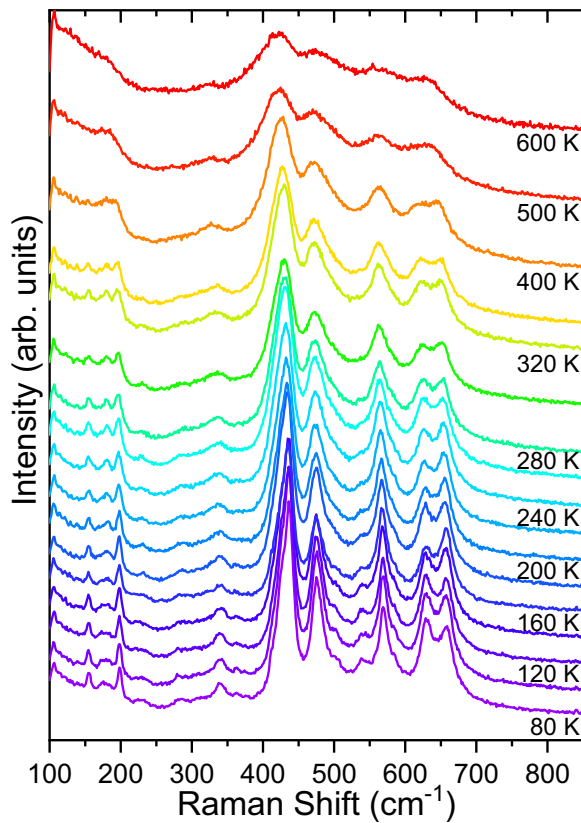


FIG. 8. Unpolarized Raman spectra of $\text{BiMn}_7\text{O}_{12}$ ceramics recorded at several fixed temperatures. The spectra are vertically offset from each other for better resolution.

below 10 K) [25]. The magnetic contribution to the specific heat increases just below 150 K, due to precursor magnetic effects. The existence of precursor effects well above the magnetic phase transition has been observed also in rare-earth orthomanganites, like GdMnO_3 [36].

D. Raman scattering and spin-phonon coupling

Figure 8 shows the unpolarized Raman spectra recorded at different fixed temperatures, in the 100–850 cm^{-1} spectral range. The energies of the Raman modes determined in three crystal phases are listed in Table SII [25]. The high temperature Raman spectra reveal rather broad bands, due to thermal effects. The Raman spectrum recorded at 600 K is properly simulated with seven bands in this spectral range. According to group theory arguments and published crystallographic data [13], in the $Im\bar{3}$ cubic symmetry only phonons involving vibrations of oxygen atoms are Raman active. As expected, on cooling, the Raman bands become narrower and shift towards higher wave numbers, according to Eq. (3). The phase transition at $T_1 = 608$ K impacts certain spectral features, with the most evident being the splitting of the band located at 175 and 633 cm^{-1} , at 600 K, and the appearance of sharp bands at 158 cm^{-1} in the spectrum recorded at 380 K. The spectrum recorded at 400 K is described by 12 bands. The structural phase transition from Im to $P1$, at 290 K is revealed by the appearance of weak bands, better observed in the 470–550 cm^{-1} range. However, the number of new

bands is smaller than the number of predicted new modes in the Raman spectra recorded in the monoclinic and triclinic phases; this discrepancy is explained by a weak intensity of modes and partial/total band overlap. Nevertheless, a detailed analysis of the temperature dependencies of the frequency of some phonons reveals interesting results, which we will address in the following.

Figure 9(a) shows the temperature dependence of the phonon frequency, observed at 153 cm^{-1} at 440 K. This phonon is only observed below $T_2 = 460$ K, and its frequency exhibits a cusplike anomaly at ~ 294 K, exactly at the Im to $P1$ structural phase transition. In rare-earth orthomanganites and rare-earth orthoferrites, low frequency phonons lying in this spectral range are assigned to the A -site atomic vibrations. The appearance of this band at the cubic ($Im\bar{3}$) to the monoclinic ($I2/m$) phase transition at T_2 reveals the Raman activation of vibrations involving other than just oxygen movements. Although no mode assignment is available to the best of our knowledge, we tentatively assign the phonon seen near 150 cm^{-1} to the A - or A' -site cation vibration, likely associated with Mn oscillations. This mode assignment is also supported by the current interpretation of the Raman spectra recorded in $\text{LaMn}_7\text{O}_{12}$ [37]. The ferroelectric polarization is caused mainly by displacement of Bi cations, but in the A perovskite positions there is not only Bi, but also three Mn cations which should sense the displacement of Bi cations, and therefore, the vibration of these Mn cations could also show a change in frequency at the ferroelectric phase transition from the Im to the $P1$ phase. The same phonon displays, above room temperature, an increasing damping when heating to $T_2 = 460$ K (Fig. S6 [25]). Since this phonon is highly damped above T_2 , it is not possible to accurately determine its frequency in the $I2/m$ phase. A mode with a similar frequency is seen in the IR spectra, but its value shows a strong increase with heating (Fig. S6 [25]). Also, its attenuation is high at high temperatures, so its frequency is burdened with a large error, making it impossible to determine whether it is the same mode as in the Raman spectra (which is allowed by the selection rules in Table I) or a different mode entirely.

The magnetic phase transition occurring at $T_{N1} = 59$ K is also reflected by the anomalous temperature dependence of some internal vibrations. As a representative example, we present in Figs. 9(a) and 9(b) the temperature dependence of the modes at 559 cm^{-1} (value at 400 K) and 633 cm^{-1} (value at 600 K), respectively. These two modes are known to involve the oxygen vibrations and, consequently, they account for the changes in bond angle O-Mn-O and length Mn-O, respectively. Therefore, these vibrations probe the magnetic exchange interactions. On cooling, the wave number of these two modes increases, following the anharmonic temperature behavior described by the solid lines, determined by the fit of Eq. (3) to the experimental data above 200 K and extrapolated to low temperatures. No clear anomalies are ascertained in the structural phase transitions, but a detailed inspection of the temperature dependence of the wave number of these two modes shows a clear deviation from the extrapolated anharmonic temperature behavior. The deviation is clear at $T_{N1} = 59$ K; for further cooling, an anomalous increase is observed, due to spin-phonon coupling in this compound. As representative example, we focus on the Mn-O vibration at

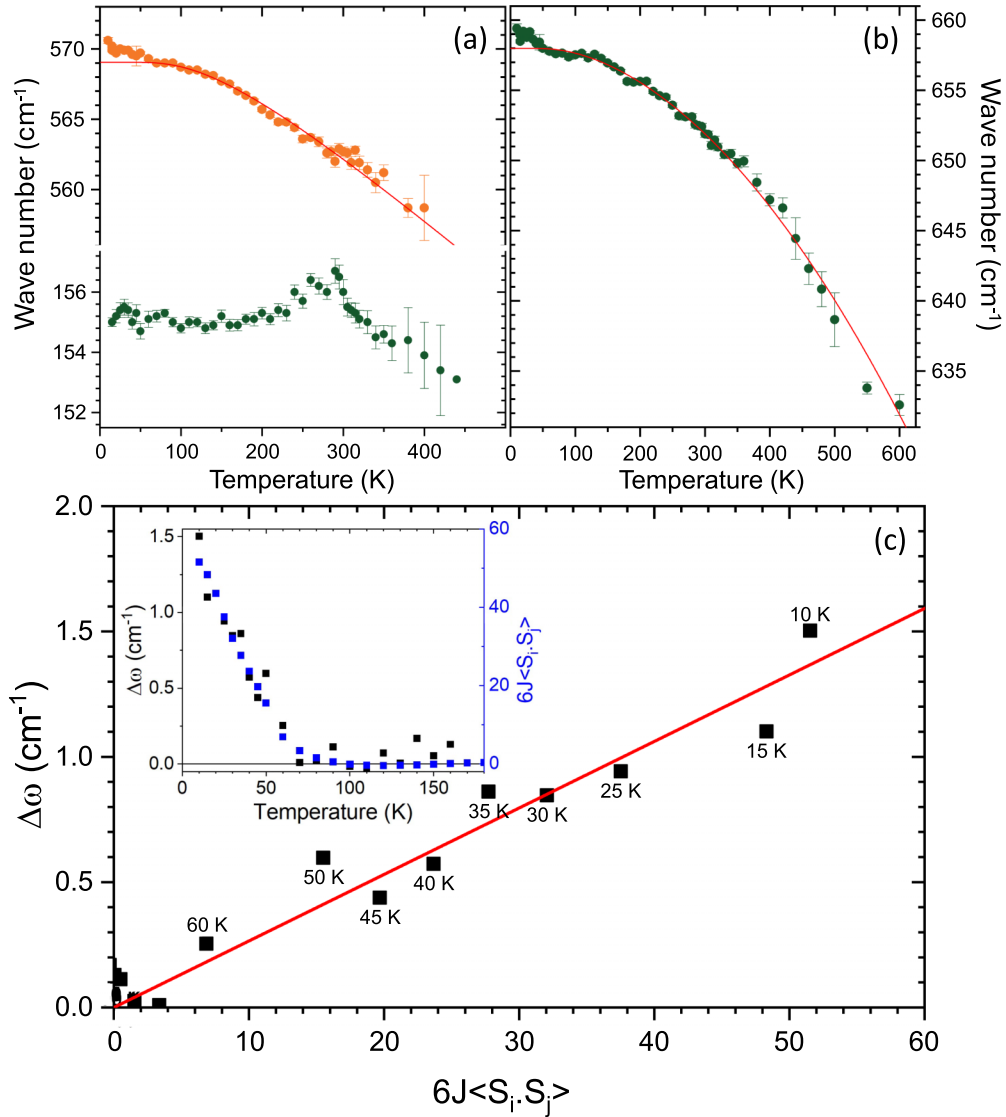


FIG. 9. (a),(b) Temperature dependence of the wave number of selected Raman modes. The best fit with Eq. (3) in the paraelectric phase is represented by a solid line and is extrapolated down to 0 K. (c) The deviation, $\Delta\omega$, of the highest phonon frequency seen near 650 cm^{-1} from the anharmonic temperature behavior [Eq. (3)] as a function of the spin-spin correlation function, $6J\langle S_i \cdot S_j \rangle$, obtained from integrating the magnetic contribution to the specific heat, shown in Fig. 7. Inset: temperature dependencies of $\Delta\omega$ and $6J\langle S_i \cdot S_j \rangle$.

$\sim 559\text{ cm}^{-1}$ (value at 400 K), shown in Fig. 9(a), which better senses the magnetic phase transition at T_{N1} . According to spin-phonon coupling theory presented in Eq. (4), the anomalous temperature dependence of the wave number must be a linear function of the spin-spin correlation function, $\langle S_i \cdot S_j \rangle$, which can be calculated from the integral of the magnetic contribution to the specific heat shown in Fig. 9 [32]. In this case, the anomalous temperature dependence of the wave number of the aforementioned Mn-O vibration is a linear function of the spin-spin correlation function, as shown in Fig. 9(c), providing clear evidence for the coupling between lattice vibrations and the magnetic momenta in $\text{BiMn}_7\text{O}_{12}$. Note that the spin-spin correlation function calculated from the magnetic contribution to the specific heat increases linearly below T_{N1} and saturates at low temperatures below 10 K [see inset of Fig. 9(c)].

The detailed temperature dependence of other Raman-active phonons is shown in Fig. S5 [25]. The classical anharmonic behavior, according to Eq. (3), is observed for most phonons, except the mode at 340 cm^{-1} which exhibits an anomalous temperature behavior, likely caused by a short-range magnetic order above T_{N1} .

IV. CONCLUSIONS

We observed the softening of a phonon in the THz range on cooling towards $T_2 = 460\text{ K}$, a temperature at which $\text{BiMn}_7\text{O}_{12}$ undergoes a structural phase transition from monoclinic $I2/m$ to a noncentrosymmetric monoclinic Im phase. At 300 K, this phonon also has an anomaly coinciding with another structural phase transition to the $P1$ phase, in which the polarization is predicted to move out of the ac plane. The observed behavior of the optical phonon is typical for

displacive ferroelectric phase transitions. Also, the microwave permittivity shows a peak at $T_3 = 290$ K, indicating the ferroelectric nature of the phase transition at this temperature. For experimental reasons, it was not possible to measure the microwave permittivity above 400 K, i.e., not near T_2 or T_1 . Unfortunately, neither the polarization hysteresis loops nor the pyrocurrent could be measured due to the conductivity of the sample above 100 K, but the soft mode in THz and IR spectra clearly indicates signs of successive displacive ferroelectric phase transitions in the two polar phases Im and $P1$.

The results here presented are consistent with the recently reported temperature dependence of the polarization calculated from Mössbauer data for $\text{BiMn}_{6.96}\text{Fe}_{0.04}\text{O}_{12}$, showing a paraelectric to ferroelectric phase transition around 437 K, and a considerable increase in polarization below 270 K, with an extrapolated Curie temperature of 294 K [19].

The dielectric anomalies, measured at 5.8 GHz and in the 1–10 Hz range, observed near T_{N1} and T_{N3} are indicative of a strong magnetoelectric coupling at the magnetic phase transitions. This supports the conclusions of Ref. [18] that the

polar magnetic phases are stabilized by trilinear magnetoelectric coupling via inverse exchange striction.

The Raman mode seen near 155 cm^{-1} senses the structural phase transition at 300 K. Furthermore, some Raman modes sense the magnetic phase transitions occurring at 59, 55, and 27 K, showing that spin-phonon coupling is relevant in this compound in this temperature range. The highest-frequency mode observed near 660 cm^{-1} exhibits a clear deviation from anharmonic temperature dependence, which is linearly correlated with the spin correlation function $(S_i \cdot S_j)$.

ACKNOWLEDGMENTS

The authors thank J. Maňák and M. Savinov, respectively, for SEM characterization of the ceramic grains and permittivity measurements in the Hz range below 100 K. This work was supported by the VEGA 2/0137/19 project and the Czech Science Foundation (Project No. 21–06802S).

The authors declare no competing interests.

-
- [1] A. N. Vasil'ev and O. S. Volkova, New functional materials $\text{AC}_3\text{B}_4\text{O}_{12}$ (Review), *Low Temp. Phys.* **33**, 895 (2007).
- [2] I. Yamada, High-pressure synthesis, electronic states, and structure-property relationships of perovskite oxides, $\text{ACu}_3\text{Fe}_4\text{O}_{12}$ (A: Divalent alkaline earth or trivalent rare-earth ion), *J. Ceram. Soc. Jpn.* **122**, 846 (2014).
- [3] A. A. Belik, Y. Matsushita, and D. D. Khalyavin, Reentrant structural transitions and collapse of charge and orbital orders in quadruple perovskites, *Angew. Chem.* **56**, 10423 (2017).
- [4] J. Li, M. A. Subramanian, H. D. Rosenfeld, C. Y. Jones, B. H. Toby, and A. W. Sleight, Clues to the giant dielectric constant of $\text{CaCu}_3\text{Ti}_4\text{O}_{12}$ in the defect structure of “ $\text{SrCu}_3\text{Ti}_4\text{O}_{12}$ ”, *Chem. Mater.* **16**, 5223 (2004).
- [5] C. C. Homes, T. Vogt, S. M. Shapiro, S. Wakimoto, and A. P. Ramirez, Optical response of high-dielectric-constant perovskite-related oxide, *Science* **293**, 673 (2001).
- [6] R. D. Johnson, L. C. Chapon, D. D. Khalyavin, P. Manuel, P. G. Radaelli, and C. Martin, Giant improper ferroelectricity in the ferroaxial magnet $\text{CaMn}_7\text{O}_{12}$, *Phys. Rev. Lett.* **108**, 067201 (2012).
- [7] A. Maia, C. Kadlec, M. Savinov, R. Vilarinho, J. A. Moreira, V. Bovtun, M. Kempa, M. Míšek, J. Kaštil, A. Prokhorov, J. Maňák, A. A. Belik, and S. Kamba, Can the ferroelectric soft mode trigger an antiferromagnetic phase transition? *J. Eur. Ceram. Soc.* **43**, 2479 (2023).
- [8] I. Yamada, Novel catalytic properties of quadruple perovskites, *Sci. Technol. Adv. Mater.* **18**, 541 (2017).
- [9] A. Prodi, E. Gilioli, A. Gauzzi, F. Licci, M. Marezio, F. Bolzoni, Q. Huang, A. Santoro, and J. W. Lynn, Charge, Orbital and spin ordering phenomena in the mixed valence manganese $\text{NaMn}_3^{3+}(\text{Mn}_2^{3+}\text{Mn}_2^{4+})\text{O}_{12}$, *Nat. Mater.* **3**, 48 (2004).
- [10] A. Prodi, A. Daoud-Aladine, F. Gozzo, B. Schmitt, O. Lebedev, G. van Tendeloo, E. Gilioli, F. Bolzoni, H. Aruga-Katori, H. Takagi, M. Marezio, and A. Gauzzi, Commensurate structural modulation in the charge- and orbitally ordered phase of the quadruple perovskite $(\text{NaMn}_3)\text{Mn}_4\text{O}_{12}$, *Phys. Rev. B* **90**, 180101(R) (2014).
- [11] M. Marezio, P. D. Dernier, J. Chenavas, and J. C. Joubert, High pressure synthesis and crystal structure of $\text{NaMn}_7\text{O}_{12}$, *J. Solid State Chem.* **6**, 16 (1973).
- [12] B. Bochu, J. Chenavas, J. C. Joubert, and M. Marezio, High pressure synthesis and crystal structure of a new series of perovskite-like compounds $\text{CMn}_7\text{O}_{12}$ (C = Na, Ca, Cd, Sr, La, Nd), *J. Solid State Chem.* **11**, 88 (1974).
- [13] A. A. Belik, Y. Matsushita, Y. Kumagai, Y. Katsuya, M. Tanaka, S. Y. Stefanovich, B. I. Lazoryak, F. Oba, and K. Yamaura, Complex structural behavior of $\text{BiMn}_7\text{O}_{12}$ quadruple perovskite, *Inorg. Chem.* **56**, 12272 (2017).
- [14] W. A. Sławiński, H. Okamoto, and H. Fjellvåg, Triclinic crystal structure distortion of multiferroic $\text{BiMn}_7\text{O}_{12}$, *Acta Crystallogr. B: Struct. Sci. Cryst. Eng. Mater.* **73**, 313 (2017).
- [15] K. Momma and F. Izumi, VESTA 3 for three-dimensional visualization of crystal, volumetric and morphology data, *J. Appl. Crystallogr.* **44**, 1272 (2011).
- [16] A. Gauzzi, G. Rousse, F. Mezzadri, G. L. Calestani, G. André, F. Bourée, M. Calicchio, E. Gilioli, R. Cabassi, F. Bolzoni, A. Prodi, P. Bordet, and M. Marezio, Magnetoelectric coupling driven by inverse magnetostriction in multiferroic $\text{BiMn}_3\text{Mn}_4\text{O}_{12}$, *J. Appl. Phys.* **113**, 043920 (2013).
- [17] F. Mezzadri, M. Buzzi, C. Pernechele, G. Calestani, M. Solzi, A. Migliori, and E. Gilioli, Polymorphism and multiferroicity in $\text{Bi}_{1-x/3}(\text{Mn}_5^{\text{III}})(\text{Mn}_{4-x}^{\text{III}}\text{Mn}_x^{\text{IV}})\text{O}_{12}$, *Chem. Mater.* **23**, 3628 (2011).
- [18] D. Behr, A. A. Belik, D. D. Khalyavin, and R. D. Johnson, $\text{BiMn}_7\text{O}_{12}$: Polar antiferromagnetism by inverse exchange striction, *Phys. Rev. B* **107**, L140402 (2023).
- [19] V. I. Nitsenko, A. V. Sobolev, A. A. Belik, Y. S. Glazkova, and I. A. Presnyakov, Electric polarization in the $\text{BiMn}_7\text{O}_{12}$ quadruple manganite: A ^{57}Fe probe Mössbauer investigation, *J. Exp. Theor. Phys.* **136**, 620 (2023).

- [20] A. V. Sobolev, V. I. Nitsenko, A. A. Belik, I. S. Glazkova, M. S. Kondratyeva, and I. A. Presniakov, Jahn–Teller ordering dynamics in the paraelectric $\text{BiMn}_7\text{O}_{12}$ phase: ^{57}Fe probe Mössbauer diagnostics, *J. Exp. Theor. Phys.* **137**, 404 (2023).
- [21] D. D. Khalyavin, R. D. Johnson, F. Orlandi, P. G. Radaelli, P. Manuel, and A. A. Belik, Emergent helical texture of electric dipoles, *Science* **369**, 680 (2020).
- [22] N. Imamura, M. Karppinen, T. Motohashi, D. Fu, M. Itoh, and H. Yamauchi, Positive and negative magnetodielectric effects in A-site ordered $(\text{BiMn}_3)\text{Mn}_4\text{O}_{12}$ perovskite, *J. Am. Chem. Soc.* **130**, 14948 (2008).
- [23] N. Imamura, K. Singh, D. Pelloquin, C. Simon, T. Sasagawa, M. Karppinen, H. Yamauchi, and A. Maignan, Magnetodielectric response of square-coordinated MnO_2 unit in cubic $\text{BiMn}_7\text{O}_{12}$, *Appl. Phys. Lett.* **98**, 072903 (2011).
- [24] F. Izumi and T. Ikeda, *A Rietveld-analysis Program RIETAN-98 and its Applications to Zeolites*, Materials Science Forum Vol. 321-324 (Trans Tech, Ltd, 2000), p. 198.
- [25] See Supplemental Material at <http://link.aps.org/supplemental/10.1103/PhysRevB.109.134111> for additional data on SEM images, magnetization, permittivity, and MIR spectrum. It also contains Refs. [22,23,26].
- [26] F. Mezzadri, G. Calestani, M. Calicchio, E. Gilioli, F. Bolzoni, R. Cabassi, M. Marezio, and A. Migliori, Synthesis and characterization of multiferroic $\text{BiMn}_7\text{O}_{12}$, *Phys. Rev. B* **79**, 100106(R) (2009).
- [27] V. Bovtun, V. Pashkov, M. Kempa, S. Kamba, A. Eremenko, V. Molchanov, Y. Poplavko, Y. Yakymenko, J. H. Lee, and D. G. Schlom, An electrode-free method of characterizing the microwave dielectric properties of high-permittivity thin films, *J. Appl. Phys.* **109**, 024106 (2011).
- [28] V. Bovtun, S. Veljko, A. Axelsson, S. Kamba, N. Alford, and J. Petzelt, Microwave characterization of thin ferroelectric films without electrodes by composite dielectric resonator, *Integr. Ferroelectr.* **98**, 53 (2008).
- [29] V. Skoromets, C. Kadlec, H. Němec, D. Fattakhova-Rohlfing, and P. Kužel, Tunable dielectric properties of KTaO_3 single crystals in the terahertz range, *J. Phys. D: Appl. Phys.* **49**, 065306 (2016).
- [30] W. Hayes and R. Loudon, *Scattering of Light by Crystals* (Wiley-Interscience, New York, 1978), Vol. 47.
- [31] M. Balkanski, R. F. Wallis, and E. Haro, Anharmonic effects in light scattering due to optical phonons in silicon, *Phys. Rev. B* **28**, 1928 (1983).
- [32] A. B. Sushkov, O. Tchernyshyov, W. Ratcliff II, S. W. Cheong, and H. D. Drew, Probing spin correlations with phonons in the strongly frustrated magnet ZnCr_2O_4 , *Phys. Rev. Lett.* **94**, 137202 (2005).
- [33] M. I. Aroyo, J. M. Perez-Mato, D. Orobengoa, E. Tasci, G. De La Flor, and A. Kirov, Crystallography online: Bilbao crystallographic server, *Bulg. Chem. Commun.* **43**, 183 (2011).
- [34] M. I. Aroyo, J. M. Perez-Mato, C. Capillas, E. Kroumova, S. Ivantchev, G. Madariaga, A. Kirov, and H. Wondratschek, Bilbao crystallographic server: I. Databases and crystallographic computing programs, *Z. Kristallogr. Cryst. Mater.* **221**, 15 (2006).
- [35] M. I. Aroyo, A. Kirov, C. Capillas, J. M. Perez-Mato, and H. Wondratschek, Bilbao crystallographic server. II. Representations of crystallographic point groups and space groups, *Acta Crystallogr., Sect. A* **62**, 115 (2006).
- [36] R. Vilarinho, E. C. Queirós, A. Almeida, P. B. Tavares, M. Guennou, J. Kreisel, and J. A. Moreira, Scaling spin–phonon and spin–spin interactions in magnetoelectric $\text{Gd}_{1-x}\text{Y}_x\text{MnO}_3$, *J. Solid State Chem.* **228**, 76 (2015).
- [37] V. S. Bhadram, B. Joseph, D. Delmonte, E. Gilioli, B. Baptiste, Y. Le Godec, R. P. S. M. Lobo, and A. Gauzzi, Pressure-induced structural phase transition and suppression of Jahn-Teller distortion in the quadruple perovskite structure, *Phys. Rev. Mater.* **5**, 104411 (2021).

Supplemental Information

Two displacive Ferroelectric Phase Transitions in Multiferroic Quadruple Perovskite $\text{BiMn}_7\text{O}_{12}$

A. Maia¹, C. Kadlec¹, M. Kempa¹, V. Bovtun¹, R. Vilarinho², J. Agostinho Moreira², Alexei A. Belik³, P. Proschek⁴, S. Kamba^{1*}

¹*Institute of Physics of the Czech Academy of Sciences, Na Slovance 2, 182 21 Prague 8, Czech Republic*

²*IFIMUP, Physics and Astronomy Department, Faculty of Sciences, University of Porto, Rua do Campo Alegre 687, s/n- 4169-007 Porto, Portugal*

³*International Center for Materials Nanoarchitectonics (WPI-MANA), National Institute for Materials Science (NIMS), Namiki 1-1, Tsukuba, Ibaraki 305-0044, Japan*

⁴*Faculty of Mathematics and Physics, Charles University, Ke Karlovu 5, 121 16 Prague, Czech Republic*

*e-mail: kamba@fzu.cz

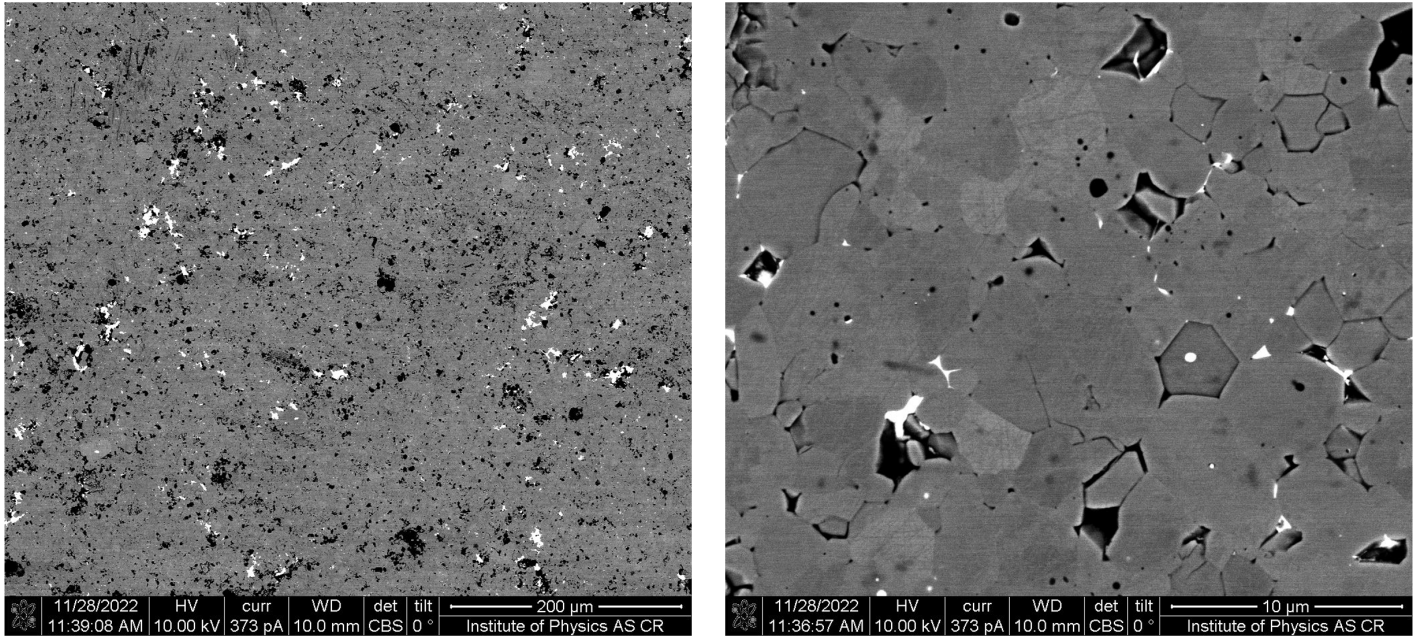


Figure S1. Scanning electron microscope (SEM) images of $\text{BiMn}_7\text{O}_{12}$ ceramics at different scales, indicated in the lower right corner of each panel. Grains with a diameter of several μm are visible. Measured using ThermoFisher FEI Quanta 3D SEM microscope.

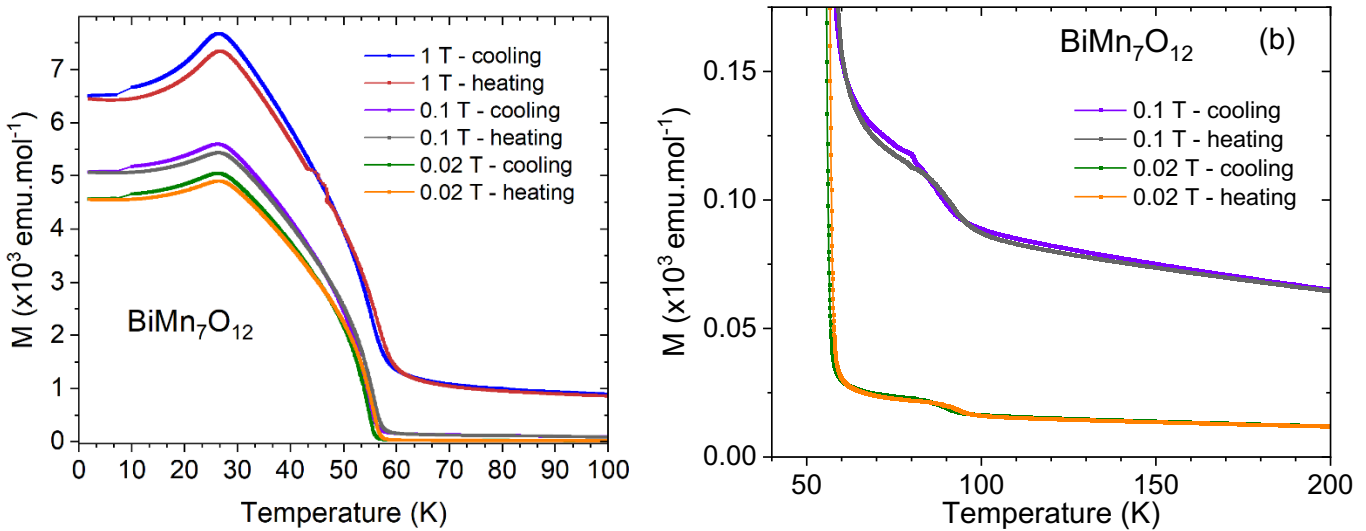


Figure S2. (a) Temperature dependence of magnetization of $\text{BiMn}_7\text{O}_{12}$, measured in heating and cooling runs under several static magnetic fields. Similar magnetic anomalies were published in References [1-3]. (b) Detail of the temperature dependence of magnetization in a weak magnetic field showing a weak anomaly around 90 K. The origin of this anomaly is unknown, but at this temperature the weak dielectric anomaly in Figure 4 (main text) is also visible.

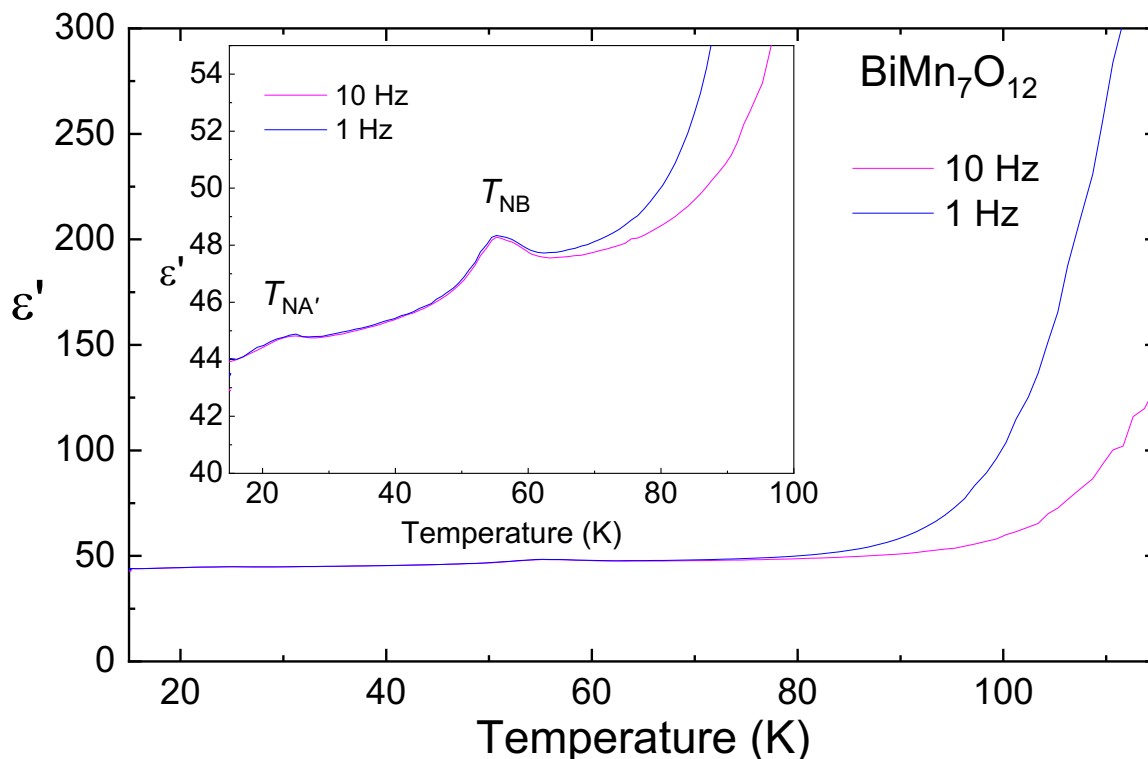


Figure S3. Temperature dependence of dielectric permittivity near magnetic phase transitions. The same anomalies are seen in microwave permittivity at 5.8 GHz (see Figure 4 in the main text). The permittivity tends to very large values above 100 K due to inhomogeneous conductivity in the ceramics and grains (Maxwell-Wagner polarization).

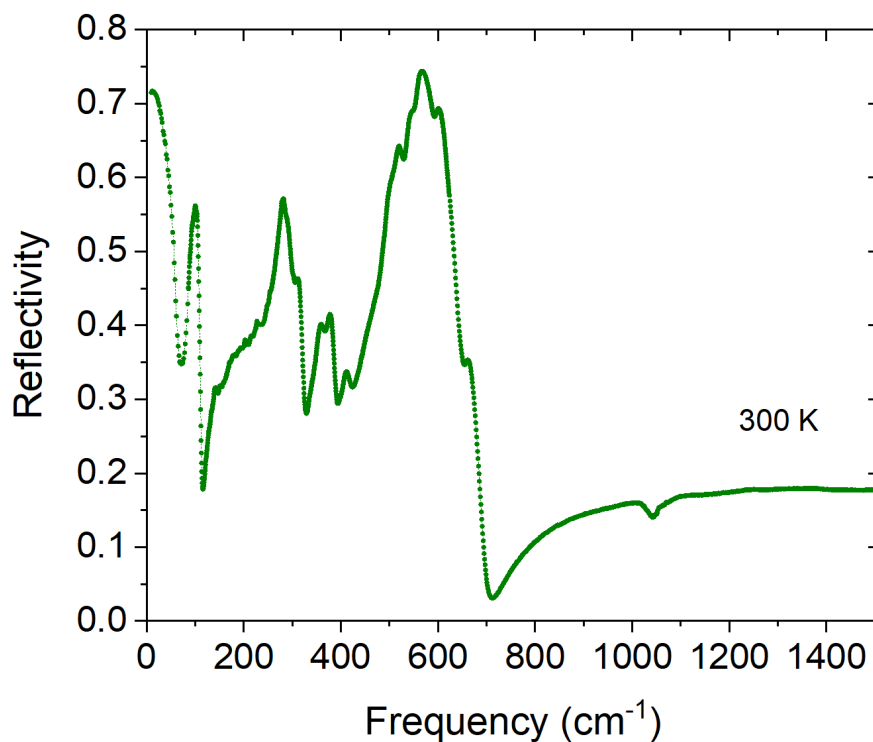


Figure S4. Representative example of the IR reflectivity spectra of $\text{BiMn}_7\text{O}_{12}$ recorded at 300 K, measured up to 1500 cm^{-1} . The anomaly around 1050 cm^{-1} is artificially induced by water in the KBr beam splitter used for middle IR measurement.

Table SI. Parameters used to fit the IR spectra of BiMn₇O₁₂ with the 3-parameter model, at 20 K, 300 K and 500 K. A temperature independent $\epsilon_{\infty} = 6.80$ was used.

Fit Parameters (cm ⁻¹)	Temperature (K)		
	20	300	500
$\Delta\epsilon_1$	7.57	78.52	--
ω_{01}	29.5	19.5	--
γ_1	27.2	20.1	--
$\Delta\epsilon_2$	15.18	19.16	119.80
$\omega_{02} = \omega_{SM}$	51.1	32.5	25.8
γ_2	14.3	22.7	25.4
$\Delta\epsilon_3$	0.66	7.25	--
ω_{03}	70.4	49.1	--
γ_3	11.6	31.2	--
$\Delta\epsilon_4$	0.93	1.78	2.28
ω_{04}	80.5	93.2	96.6
γ_4	11.8	9.2	13.9
$\Delta\epsilon_5$	1.99	1.00	0.84
ω_{05}	94.0	98.6	101.5
γ_5	12.7	7.3	10.1
$\Delta\epsilon_6$	1.18	0.63	0.055
ω_{06}	104.1	103.1	107.3
γ_6	8.7	8.6	7.2
$\Delta\epsilon_7$	0.16	0.065	0.38
ω_{07}	146.5	144.0	152.0
γ_7	7.9	5.9	32.6
$\Delta\epsilon_8$	0.045	0.078	0.0024
ω_{08}	158.2	153.8	165.5
γ_8	6.3	10.5	3.8
$\Delta\epsilon_9$	0.024	--	--
ω_{09}	182.1	--	--
γ_9	3.4	--	--
$\Delta\epsilon_{10}$	0.30	0.13	0.098
ω_{010}	182.4	181.0	177.1
γ_{10}	23.7	16.8	18.7
$\Delta\epsilon_{11}$	0.0755	0.073	0.12
ω_{011}	200.1	194.2	191.8
γ_{11}	7.1	11.7	19.0
$\Delta\epsilon_{12}$	0.053	0.10	0.083
ω_{012}	212.0	205.76	202.8
γ_{12}	5.8	11.6	14.2
$\Delta\epsilon_{13}$	0.032	0.028	0.026
ω_{013}	222.1	217.0	213.8
γ_{13}	4.6	6.1	8.5
$\Delta\epsilon_{14}$	0.20	0.22	0.33
ω_{014}	238.9	232.5	228.7
γ_{14}	23.5	18.7	27.7
$\Delta\epsilon_{15}$	0.014	--	--
ω_{015}	242.0	--	--

γ_{15}	3.1	--	--
$\Delta\epsilon_{16}$	1.03	1.43	2.31
ω_{016}	280.7	280.7	283.3
γ_{16}	10.1	16.1	31.7
$\Delta\epsilon_{17}$	0.60	0.83	0.39
ω_{017}	294.4	291.4	299.1
γ_{17}	9.7	18.9	24.5
$\Delta\epsilon_{18}$	0.15	0.096	0.29
ω_{018}	303.1	302.3	309.8
γ_{18}	9.5	11.2	22.9
$\Delta\epsilon_{19}$	0.13	--	--
ω_{019}	310.4	--	--
γ_{19}	8.9	--	--
$\Delta\epsilon_{20}$	0.47	0.64	0.0081
ω_{020}	316.9	312.0	322.6
γ_{20}	9.5	19.1	10.2
$\Delta\epsilon_{21}$	0.21	0.057	0.0018
ω_{021}	343.9	340.0	337.4
γ_{21}	10.2	16.2	3.4
$\Delta\epsilon_{22}$	0.028	--	--
ω_{022}	355.4	--	--
γ_{22}	4.6	--	--
$\Delta\epsilon_{23}$	0.028	0.41	0.30
ω_{023}	357.8	359.6	359.7
γ_{23}	5.2	20.7	28.5
$\Delta\epsilon_{24}$	0.13	0.068	0.062
ω_{024}	362.2	368.4	367.3
γ_{24}	7.6	16.8	12.5
$\Delta\epsilon_{25}$	0.10	0.24	0.41
ω_{025}	371.4	377.3	378.4
γ_{25}	7.3	16.1	23.4
$\Delta\epsilon_{26}$	0.33	0.20	0.018
ω_{026}	382.5	382.3	372.9
γ_{26}	12.0	17.7	7.3
$\Delta\epsilon_{27}$	0.022	0.0042	0.019
ω_{027}	407.3	398.2	390.6
γ_{27}	6.3	5.6	10.9
$\Delta\epsilon_{28}$	0.12	0.28	0.33
ω_{028}	418.8	414.1	399.4
γ_{28}	8.4	26.7	47.5
$\Delta\epsilon_{29}$	0.15	--	--
ω_{029}	428.0	--	--
γ_{29}	11.3	--	--
$\Delta\epsilon_{30}$	0.039	--	--
ω_{030}	441.4	--	--
γ_{30}	9.0	--	--
$\Delta\epsilon_{31}$	0.13	--	--
ω_{031}	462.6	--	--
γ_{31}	17.4	--	--
$\Delta\epsilon_{32}$	0.38	0.34	0.0081
ω_{032}	479.5	467.8	436.4

γ_{32}	14.0	50.6	10.6
$\Delta\epsilon_{33}$	0.70	0.52	0.21
ω_{033}	506.3	499.5	493.2
γ_{33}	14.1	17.1	22.0
$\Delta\epsilon_{34}$	0.22	--	--
ω_{034}	516.5	--	--
γ_{34}	13.0	--	--
$\Delta\epsilon_{35}$	0.54	1.96	2.24
ω_{035}	523.9	513.7	510.4
γ_{35}	12.9	32.2	43.4
$\Delta\epsilon_{36}$	0.30	0.37	0.56
ω_{036}	540.0	536.5	533.4
γ_{36}	14.4	17.2	33.9
$\Delta\epsilon_{37}$	0.12	--	--
ω_{037}	549.5	--	--
γ_{37}	8.9	--	--
$\Delta\epsilon_{38}$	0.20	0.52	0.34
ω_{038}	560.8	551.8	550.3
γ_{38}	12.9	31.5	45.2
$\Delta\epsilon_{39}$	0.10	--	--
ω_{039}	576.0	--	--
γ_{39}	25.4	--	--
$\Delta\epsilon_{40}$	0.028	0.058	0.087
ω_{040}	600.5	592.1	588.4
γ_{40}	12.6	24.2	42.1
$\Delta\epsilon_{41}$	0.017	0.23	0.19
ω_{041}	632.0	671.8	636.6
γ_{41}	14.8	86.8	89.9

Table SII. Frequencies of the Raman modes of BiMn₇O₁₂ at 20 K, 300 K and 500 K.

Wavenumber (cm ⁻¹)	Temperature (K)		
	20	300	500
ω_{01}	155.2	156.0	147.3
ω_{02}	185.1	180.8	180.2
ω_{03}	198.8	197.1	192.9
ω_{04}	287.5	283.0	271.4
ω_{05}	323.2	313.8	302.3
ω_{06}	343.1	336.1	324.9
ω_{07}	366.5	231.3	200.0
ω_{08}	429.2	421.3	418.2
ω_{09}	438.0	432.9	432.1
ω_{010}	475.9	473.4	469.2
ω_{011}	504.8	497.5	489.1
ω_{012}	539.1	533.3	--
ω_{013}	569.7	562.7	--
ω_{014}	574.2	568.1	563.6
ω_{015}	631.1	623.8	609.8
ω_{016}	659.2	651.9	638.7

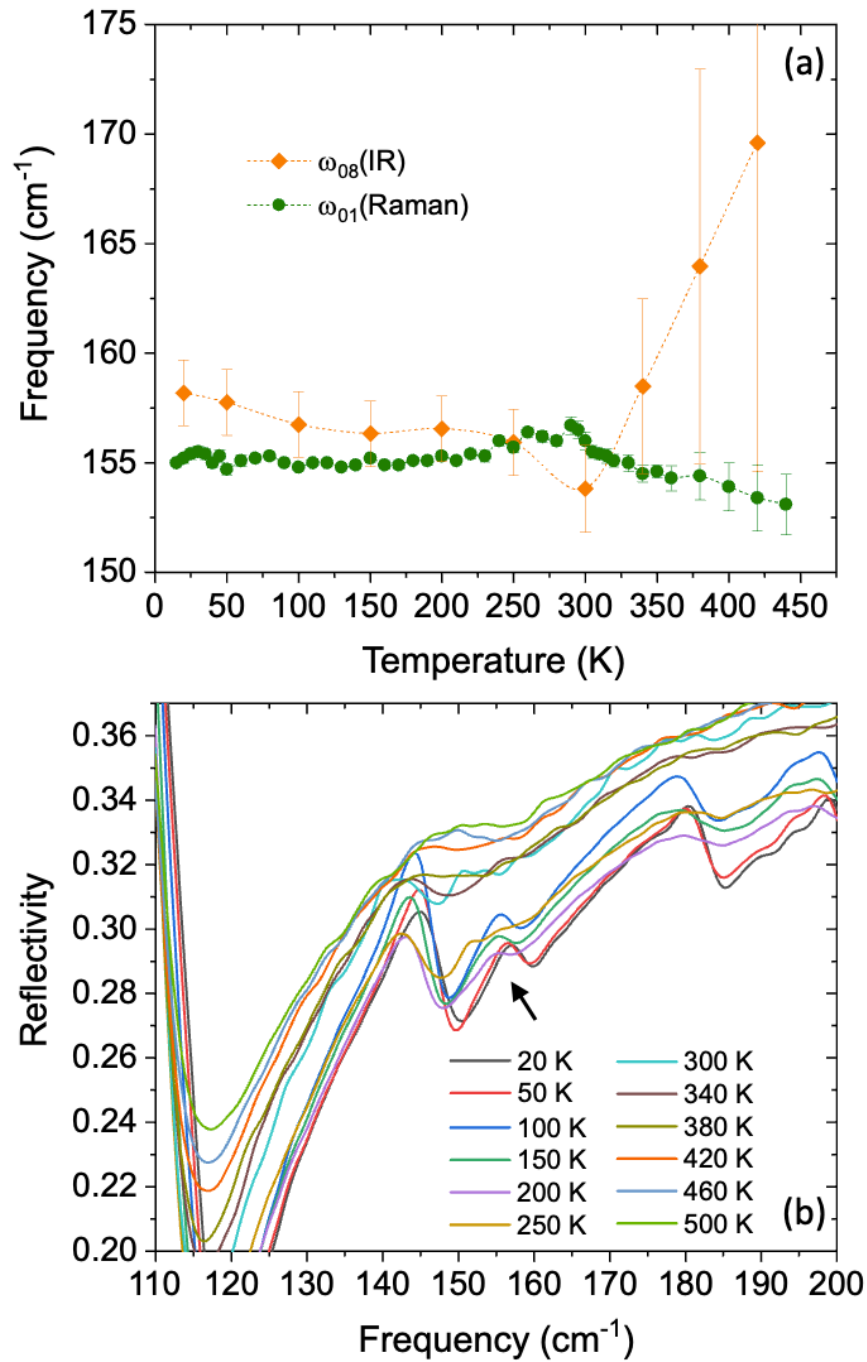


Figure S5. (a) Temperature dependence of the frequencies of the ω_{08} mode in IR spectra and of the ω_{01} mode in the Raman spectra of BiMn₇O₁₂. (b) IR spectra in the 110-200 cm⁻¹ range, where the ω_{08} mode (indicated by an arrow) is clearly visible at low temperatures and becomes heavily damped above room temperature.

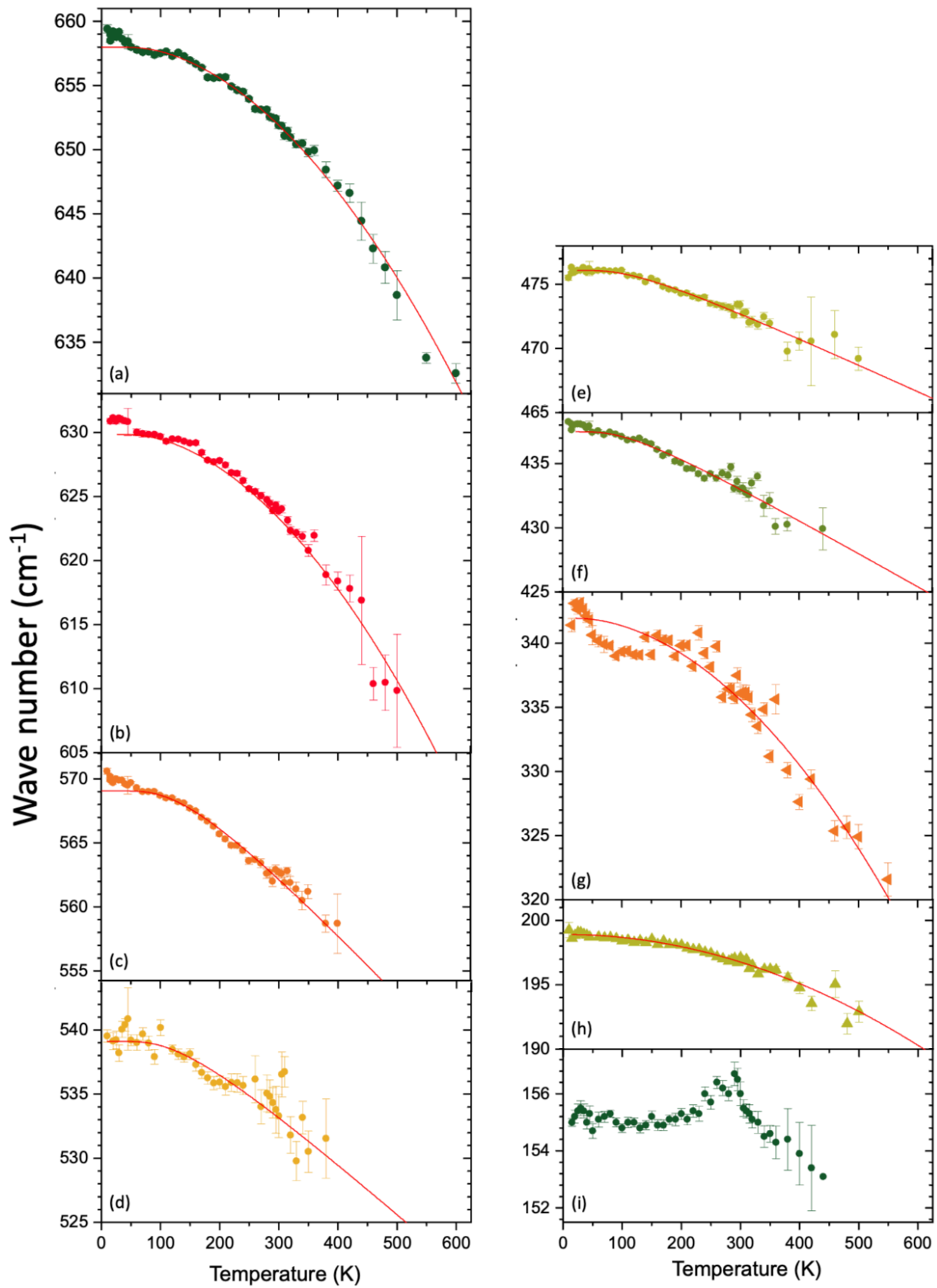






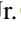




Figure S6. Temperature dependence of the frequencies of selected Raman modes. The best fit with Equation 3 (in the main text) in the paraelectric phase is represented by a solid line and is extrapolated down to 0 K.

References

- [1] F. Mezzadri, G. Calestani, M. Calicchio, E. Gilioli, F. Bolzoni, R. Cabassi, M. Marezio, and A. Migliori, Synthesis and characterization of multiferroic $\text{BiMn}_7\text{O}_{12}$, *Phys. Rev. B* **79**, 100106 (2009).
- [2] N. Imamura, M. Karppinen, T. Motohashi, D. Fu, M. Itoh, and H. Yamauchi, Positive and negative magnetodielectric effects in *A*-site ordered $(\text{BiMn}_3)\text{Mn}_4\text{O}_{12}$ perovskite, *J. Am. Chem. Soc.* **130**, 14948-9 (2008)
- [3] N. Imamura, K. Singh, D. Pelloquin, Ch. Simon, T. Sasagawa, M. Karppinen, H. Yamauchi, and A. Maignan, Magnetodielectric response of square-coordinated MnO_2 unit in cubic $\text{BiMn}_7\text{O}_{12}$, *Appl. Phys. Lett.* **98**, 072903 (2011)

A.3 Modifying the magnetoelectric coupling in TbMnO₃ by low-level Fe³⁺ substitution

The paper “Modifying the magnetoelectric coupling in TbMnO₃”, Ref.^{A3}, is presented in this section.

Modifying the magnetoelectric coupling in TbMnO₃ by low-level Fe³⁺ substitutionA. Maia ¹, R. Vilarinho ², C. Kadlec ¹, M. Lebeda ¹, M. Mihalik, Jr. ³, M. Zentková ³, M. Mihalik ³,
J. Agostinho Moreira ^{2,*} and S. Kamba ^{1,†}¹*Institute of Physics of the Czech Academy of Sciences, Na Slovance 2, 182 21 Prague 8, Czech Republic*²*IFIMUP, Physics and Astronomy Department, Faculty of Sciences, University of Porto, Rua do Campo Alegre 687, s/n- 4169-007 Porto, Portugal*³*Institute of Experimental Physics of the Slovak Academy of Sciences, Watsonova 47, Kosice, Slovak Republic*

(Received 31 December 2022; accepted 21 February 2023; published 10 March 2023)

We report a comprehensive study of the low-level substitution of Mn³⁺ by Fe³⁺ effect on the static and dynamic magnetoelectric coupling in TbMn_{1-x}Fe_xO₃ ($x = 0, 0.02, \text{ and } 0.04$). The cationic substitution has a large impact on the balance between competitive magnetic interactions and, as a result, on the stabilization of the magnetic structures and ferroelectric phase at low temperatures. Low-lying electromagnon excitation is activated in the cycloidal modulated antiferromagnetic and ferroelectric phase in TbMnO₃, while it is observed up to T_N in the Fe-substituted compounds, pointing at different mechanisms for static and dynamic magnetoelectric coupling. A second electrically active excitation near 40 cm^{-1} is explained by means of Tb³⁺ crystal-field effects. This excitation is observed up to room temperature, and exhibits a remarkable 15 cm^{-1} downshift on cooling in Fe-substituted compounds. Both electromagnon and crystal-field excitations are found to be coupled to the polar phonons with frequencies up to 250 cm^{-1} . Raman spectroscopy reveals a spin-phonon coupling below T_N in pure TbMnO₃, but the temperature where the coupling starts to be relevant increases with Fe concentration and reaches 100 K in TbMn_{0.96}Fe_{0.04}O₃. The anomalies in the T dependence of magnetic susceptibility above T_N are well accounted for by spin-phonon coupling and crystal-field excitation, coupled to oxygen motions.

DOI: [10.1103/PhysRevB.107.104410](https://doi.org/10.1103/PhysRevB.107.104410)**I. INTRODUCTION**

Magnetoelectric multiferroics are outstanding materials as they exhibit coupled ferroelectric and magnetic orderings in the same thermodynamic phase [1,2]. The case of type-II multiferroics is more interesting, since ferroelectricity is a consequence of a particular magnetic ordering that breaks the spatial inversion symmetry of the crystal, leading to a large magnetoelectric coupling [1,3]. TbMnO₃ is a typical representative of type-II multiferroics [4]. This material exhibits the GdFeO₃-type lattice distortion, as well as additional MnO₆ octahedra distortion arising from the cooperative Jahn-Teller effect associated with the Mn³⁺ cation [5]. Above $T_N = 41 \text{ K}$, TbMnO₃ is known to be a paramagnet and paraelectric material [4]. At T_N , it undergoes a transition into an antiferromagnetic phase in which the Mn³⁺ magnetic momenta order in the ab plane with a collinear sinusoidal incommensurate modulated structure, with wave vector along the b axis [6,7]. Below $T_C = 28 \text{ K}$, the spin structure transits into a cycloidal incommensurate antiferromagnetic, with the Mn³⁺ spins lying in the bc plane and the wave vector keeping the b direction [6,7]. This magnetic structure induces ferroelectricity via the inverse Dzyaloshinskii-Moriya mechanism [8,9]. The ferroelectric polarization develops along the c axis and can be rotated towards the a axis when a magnetic field higher

than 5.5 T is applied along the b axis, as it rotates the spin cycloidal to the ab plane [4]. The Tb³⁺ magnetic momenta order antiferromagnetically below $T'_N = 7 \text{ K}$ [4].

The dynamic magnetoelectric coupling in TbMnO₃ leads to the existence of electrically active magnons, called electromagnons [10], which have been studied by inelastic neutron scattering [11–13], Raman [14,15], IR [16–18], and terahertz (THz) [10,19–23] spectroscopies. Electromagnons in TbMnO₃ are excited by the electric field component of the THz radiation, \mathbf{E}^ω , polarized parallel to the a axis, regardless of the cycloidal plane orientation [19,24]. For this reason, the electromagnon activation is attributed to exchange striction, despite that the static ferroelectric polarization originates from the inverse Dzyaloshinskii-Moriya mechanism [24,25]. Therefore, the static and dynamic magnetoelectric couplings in TbMnO₃ have different origins. However, Dzyaloshinskii-Moriya-activated electromagnons are also present, although with a much weaker dielectric strength [23,26,27]. These are observed in the $\mathbf{E}^\omega \parallel c$ -polarized spectra, after rotating the spin cycloid by applying an external magnetic field along the b axis [9].

Despite extensive literature on this material, an abnormal temperature dependence of some physical quantities in the paramagnetic and paraelectric phase has been reported, well above T_N , which is still a matter of controversy [28,29]. The deviation of the paramagnetic susceptibility from the Curie-Weiss behavior around 200 K [28] and the anomalous temperature dependence of specific heat at this temperature [30] have been interpreted as manifestations of short-range

*jamoreir@fc.up.pt

†kamba@fzu.cz

magnetic interactions. Moreover, a negative thermal expansion along the a axis up to 150 K [29], along with anomalies in the thermal conduction coefficient at 150 K [30] and in the frequency of polar phonons assigned to both stretching and bending vibrations of MnO_6 octahedra [31,32], are considered a result of the crystal-field effect. Recent muon spin spectroscopy (μSR) experiments rule out any short-range magnetic interaction above T_N [33]. It is worth stressing that a similar negative thermal expansion has been observed in TbFeO_3 around 200 K, evidencing that such effect should arise from only the Tb^{3+} and O^{2-} ions [34].

The partial isovalent substitution of Jahn-Teller-active Mn^{3+} cation by the non-Jahn-Teller Fe^{3+} , with the same ionic radius for the sixth coordination, is a way to tune the symmetry-adapted lattice distortions, and therefore, the exchange interactions in the $\text{TbMn}_{1-x}\text{Fe}_x\text{O}_3$ solid solution [35]. Focusing on the low-level substitution, $x < 0.05$, the phase sequence remains nearly the same, with the T_N and T_C values decreasing with increasing x , while T'_N is x independent [36]. As x increases from 0 to 0.04, the lowest-temperature magnitude of the ferroelectric polarization decreases, which has been ascribed to the gradual fading out of the cycloidal magnetic ordering with increasing Fe^{3+} content, eventually leading to the suppression of ferroelectricity for $x \geq 0.05$ [35]. This hints at a strong effect of the low-level substitution of Mn^{3+} by Fe^{3+} on the static magnetoelectric coupling. These results stimulate new experimental studies in order to unravel the effect of low-level substitution on both the dynamical magnetoelectric and elementary excitations coupling.

In this work, we report the experimental study of the dynamical magnetoelectric coupling, spin-phonon coupling, and crystal-field effects on both the macroscopic and microscopic properties in oriented single-crystalline $\text{TbMn}_{1-x}\text{Fe}_x\text{O}_3$ samples, with $x = 0, 0.02$, and 0.04 , by means of polarized THz, IR, and Raman-scattering spectroscopies. Our aim is to characterize the anisotropic magnetic and polar properties of the solid solutions, to study both the static and the dynamical magnetoelectric couplings as a function of x , and to evidence the crystal-field effects as the main driver inducing non-symmetry-breaking anomalous temperature dependence of several physical properties above T_N .

This paper is organized as follows. The description of the experimental details and data analysis is provided in Sec. II. The experimental results concerning the characterization of the macroscopic magnetic and polar properties, the temperature dependence of both electromagnon, crystal-field excitations, and Brillouin-zone center lattice vibrations are presented in Sec. III. Finally, the discussion of the Fe-substitution effects on both macroscopic and microscopic properties is provided in Sec. IV. The paper ends with a summary of the main outcomes.

II. EXPERIMENT DETAILS

Crystalline $\text{TbMn}_{1-x}\text{Fe}_x\text{O}_3$ samples with $x = 0, 0.02$, and 0.04 were prepared by the floating-zone method in air atmosphere in an FZ-T-4000 (Crystal Systems Corporation) mirror furnace. As starting materials oxides of MnO_2 , Tb_4O_7 (both, purity 3N; supplier: Alpha Aesar), and Fe_2O_3 (purity 2N, supplier: Sigma-Aldrich) were used. The starting materials

were mixed in a Tb:Mn:Fe stoichiometric ratio as intended for the final compound, cold pressed into rods, and sintered at 1100 °C for 12–14 h in air [36]. The single crystals were all oriented (error below 5°), cut, and polished, when necessary, for each measurement along each crystallographic axis.

Low-field DC-induced magnetization measurements were carried out using a commercial Quantum Design superconducting quantum interference device magnetometer under an applied magnetic field of 40 Oe and with a resolution better than 5×10^{-7} emu.

The complex transmittance in the THz range (6–90 cm^{-1}) was measured using a custom-made time-domain spectrometer powered by a Ti:sapphire femtosecond laser with 35-fs-long pulses centered at 800 nm. The detection is performed via electro-optic sampling of the electric field of the transients within a 1-mm-thick, (110)-oriented ZnTe crystal as a sensor [37]. Low-temperature IR reflectivity measurements in the 50–650 cm^{-1} frequency range were performed using a Bruker IFS-113v Fourier-transform IR spectrometer. The detector is a Si bolometer, cooled to 1.6 K using liquid He. For both the THz complex transmittance and IR reflectivity measurements, the temperature was controlled by Oxford Instruments Optistat optical continuous He-flow cryostats, with Mylar and polyethylene windows, respectively. The IR spectra were fitted using a generalized-oscillator model with the factorized form of the complex permittivity:

$$\epsilon(\omega) = \epsilon'(\omega) + i\epsilon''(\omega) = \epsilon_\infty \prod_j \frac{\omega_{LOj}^2 - \omega^2 + i\omega\gamma_{LOj}}{\omega_{TOj}^2 - \omega^2 + i\omega\gamma_{TOj}}, \quad (1)$$

where ω_{TOj} and ω_{LOj} stand for transverse and longitudinal frequencies of the j th polar phonon, respectively, and γ_{TOj} and γ_{LOj} are the corresponding damping constants. The high-frequency permittivity, ϵ_∞ , originating from electronic absorption processes, was obtained from the room-temperature frequency-independent reflectivity tail above the phonon frequencies and was assumed temperature independent. The dielectric strength, $\Delta\epsilon_j$, of the j th mode is [38]

$$\Delta\epsilon_j = \frac{\epsilon_\infty}{\omega_{TOj}^2} \frac{\prod_k \omega_{LOk}^2 - \omega_{TOj}^2}{\prod_{k \neq j} \omega_{TOk}^2 - \omega_{TOj}^2}. \quad (2)$$

The complex permittivity, $\epsilon(\omega)$, is related to the reflectivity, $R(\omega)$, by

$$R(\omega) = \left| \frac{\sqrt{\epsilon(\omega)} - 1}{\sqrt{\epsilon(\omega)} + 1} \right|^2. \quad (3)$$

The unpolarized Raman spectra were measured using a Renishaw inVia Qontor spectrometer with a 532 nm linearly polarized diode-pumped laser and an edge filter. The spot size of the focused laser on the sample surface is estimated to be 2 μm diameter. The temperature was controlled through a closed-cycle helium cryostat. The laser power was set at 3.3 mW to prevent heating the sample. The temperature dependence of the frequency of a given Raman mode, $\omega(T)$, was obtained through the best fit of the Raman spectra with a sum of damped oscillators [39]:

$$I(\omega, T) = [1 + n(\omega, T)]^{-1} \sum_j \frac{\omega A_{0j} \Omega_{0j}^2 \Gamma_{0j}}{(\Omega_{0j}^2 - \omega^2)^2 + \omega^2 \Gamma_{0j}^2}, \quad (4)$$

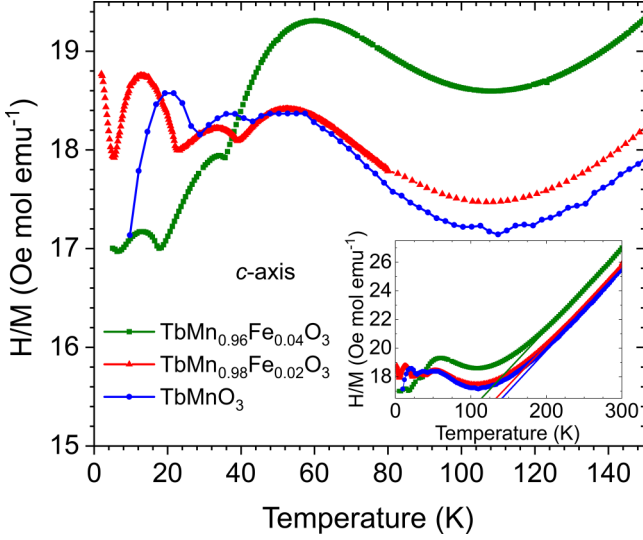


FIG. 1. Temperature dependence of the H/M ratio, measured in ZFC conditions, with a 40 Oe strength magnetic field applied along the c axis, for TbMnO_3 , $\text{TbMn}_{0.98}\text{Fe}_{0.02}\text{O}_3$, and $\text{TbMn}_{0.96}\text{Fe}_{0.04}\text{O}_3$. Inset: H/M in the 0–300 K range. Dashed lines were determined from the best fit of the Curie-Weiss law above 200 K and extrapolated to intercept the temperature axis. The data for TbMnO_3 were obtained from Ref. [28].

where $n(\omega, T)$ is the Bose-Einstein factor and A_{0j} , Ω_{0j} , and Γ_{0j} are, respectively, the strength, wave number, and damping coefficient of the j th oscillator. In the temperature range where no anomalous behavior is observed, $\omega(T)$ can be well described by the normal anharmonic temperature effect due to volume contraction as temperature decreases [5]:

$$\omega(T) = \omega_0 + C \left[1 + \frac{2}{e^x - 1} \right], \quad (5)$$

with $x \equiv \hbar\omega_0/2k_B T$ and where ω_0 and C are model constants, \hbar is the reduced Planck constant, and k_B is the Boltzmann constant.

III. EXPERIMENT RESULTS

A. Temperature dependence of magnetization and electric polarization

Figure 1 shows the temperature dependence of the ratio between the applied magnetic field H strength and the induced magnetization M , H/M , of $\text{TbMn}_{1-x}\text{Fe}_x\text{O}_3$ ($x = 0, 0.02$, and 0.04) measured in zero-field conditions (ZFC), with a magnetic field of 40 Oe applied along the c axis. The magnetic phase sequence is well ascertained from the anomalies in the temperature dependence of H/M below 50 K. Following Ref. [35], the paramagnetic-collinear sinusoidal incommensurate antiferromagnetic phase transition occurs at $T_N = 41$ K for TbMnO_3 , 39 K for $\text{TbMn}_{0.98}\text{Fe}_{0.02}\text{O}_3$, and 35 K for $\text{TbMn}_{0.96}\text{Fe}_{0.04}\text{O}_3$. On further cooling, the compounds exhibit another magnetic phase transition into a cycloidal modulated spin structure, which allows for ferroelectric polarization developing at $T_C = 28$ K in TbMnO_3 , 22 K in $\text{TbMn}_{0.98}\text{Fe}_{0.02}\text{O}_3$, and 18 K in $\text{TbMn}_{0.96}\text{Fe}_{0.04}\text{O}_3$. The lowest

TABLE I. Critical temperatures and Curie-Weiss temperature, Θ_p , of $\text{TbMn}_{1-x}\text{Fe}_x\text{O}_3$ ($0 \leq x \leq 0.04$) ascertained from the temperature dependence of the c component of magnetization. Data for TbMnO_3 were obtained from Ref. [28].

x	T_N (K)	T_C (K)	T'_N (K)	Θ_p (K)
0.00	41	28	7	-150
0.02	39	22	7	-165
0.04	35	18	5	-180

temperature anomalies observed in each curve in Fig. 1 are assigned to the ordering of the Tb^{3+} spins, occurring at $T'_N = 7$ K for $\text{TbMn}_{0.98}\text{Fe}_{0.02}\text{O}_3$, and at 5 K for $\text{TbMn}_{0.96}\text{Fe}_{0.04}\text{O}_3$.

The Curie-Weiss law is fulfilled above 200 K, as it can be seen in the inset of Fig. 1. The Curie-Weiss temperature, Θ_p , determined through the best fit of the Curie-Weiss law to the H/M data in the 200–300 K range, is found to be a decreasing function of x : $\Theta_p = -150$ K for TbMnO_3 , -165 K for $\text{TbMn}_{0.98}\text{Fe}_{0.02}\text{O}_3$, and -180 K for $\text{TbMn}_{0.96}\text{Fe}_{0.04}\text{O}_3$. The ratio $T_N/|\Theta_p|$ decreases as x increases, revealing that the ferromagnetic exchange interactions between the antiferromagnetic sublattices are reinforced, meaning that the antiferromagnetic ordering becomes less stable as x increases. Table I summarizes the critical temperatures, ascertained from the temperature anomalous dependence of H/M , and the Θ_p values.

Between T_N and 200 K, the $H/M = \chi^{-1}(T)$ data depart from the expected Curie-Weiss law observed above 200 K. Moreover, a broad minimum of $H/M(T)$ is observed at around 110 K. These abnormal temperature dependences are x independent, in agreement with previous reports for these compounds [40,41]. We will discuss the mechanism underlying this temperature behavior later on.

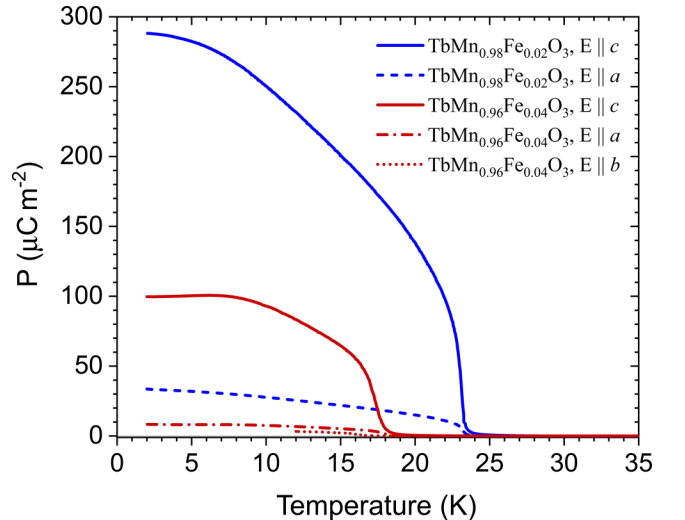


FIG. 2. Temperature dependence of the electric polarization of $\text{TbMn}_{0.98}\text{Fe}_{0.02}\text{O}_3$ and $\text{TbMn}_{0.96}\text{Fe}_{0.04}\text{O}_3$ measured along the a -, b -, and c axes.

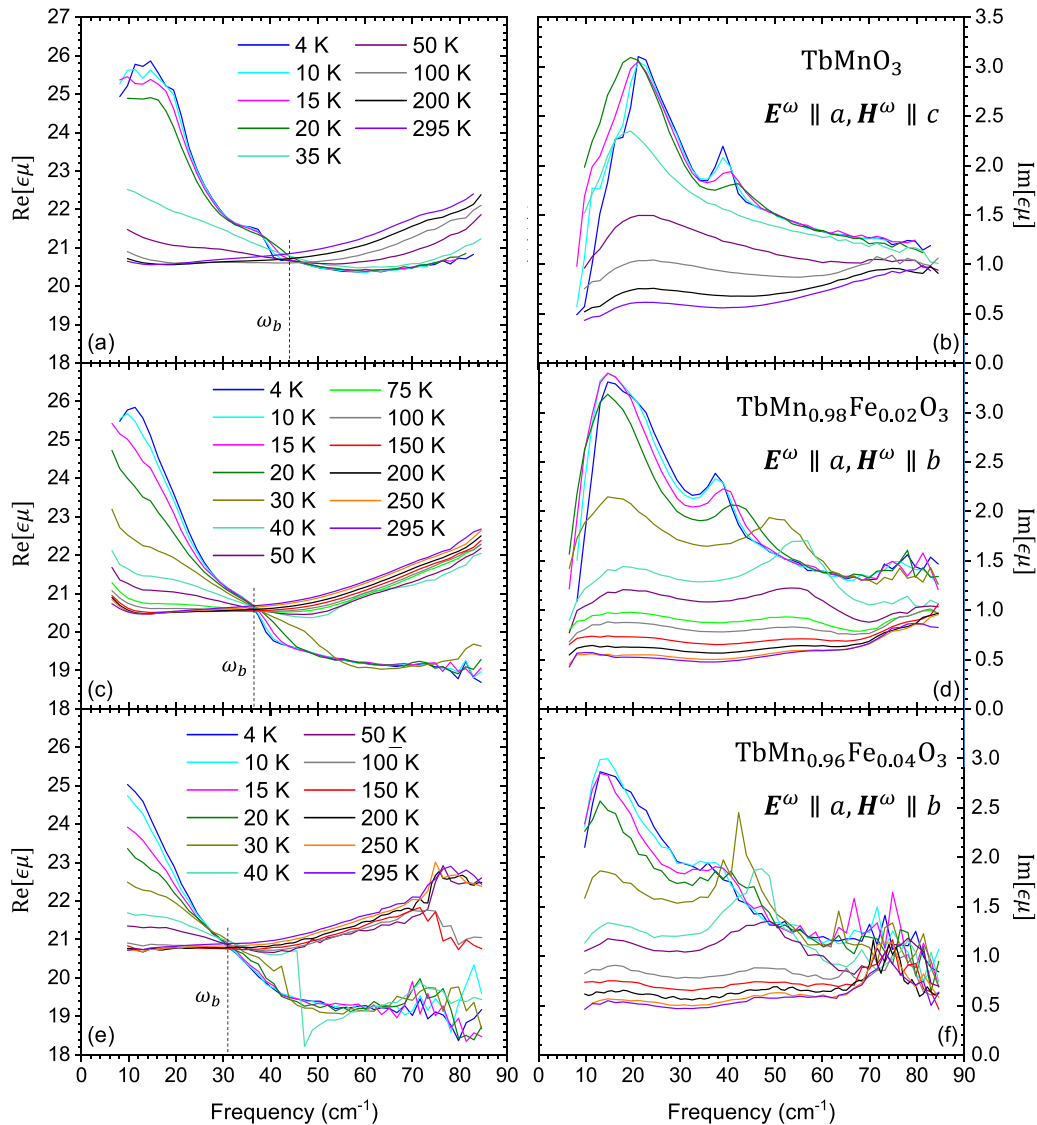


FIG. 3. $\text{Re}[\epsilon\mu]$ and $\text{Im}[\epsilon\mu]$ THz spectra for $E^\omega \parallel a$ and $H^\omega \parallel c$ of TbMnO_3 , and for $E^\omega \parallel a$ and $H^\omega \parallel b$ of $\text{TbMn}_{0.98}\text{Fe}_{0.02}\text{O}_3$ and $\text{TbMn}_{0.96}\text{Fe}_{0.04}\text{O}_3$, measured at several temperatures.

Figure 2 shows the temperature dependence of the electric polarization of $\text{TbMn}_{0.98}\text{Fe}_{0.02}\text{O}_3$ and $\text{TbMn}_{0.96}\text{Fe}_{0.04}\text{O}_3$, measured along the a and c axes. The emergence of the electric polarization occurs at 23 K and at 18 K in $\text{TbMn}_{0.98}\text{Fe}_{0.02}\text{O}_3$ and $\text{TbMn}_{0.96}\text{Fe}_{0.04}\text{O}_3$, respectively, and these values agree with the corresponding T_C 's ascertained from the anomalies in the $H/M(T)$ curves (see Table I). Below T_C , the value of the electric polarization along the a or b axis is about 9% of the corresponding values along the c axis. Assuming that the magnetic ordering in these compounds is similar to that of TbMnO_3 in the ferroelectric phase, the values of the electric polarization measured along the a and b axes most likely originate from leakage from the c axis, due to slight orientation misalignments of 5° at most.

As already observed in ceramic samples [35], the ferroelectric phase transition temperature, T_C , and the electric polarization magnitude, $|\mathbf{P}|$, decrease with increasing Fe content up to $x = 0.04$.

B. Time-domain THz spectroscopy

Figure 3 shows, respectively, the polarized THz spectra for $E^\omega \parallel a$ and $H^\omega \parallel c$ of TbMnO_3 , and for $E^\omega \parallel a$ and $H^\omega \parallel b$ of $\text{TbMn}_{0.98}\text{Fe}_{0.02}\text{O}_3$ and $\text{TbMn}_{0.96}\text{Fe}_{0.04}\text{O}_3$, recorded at several fixed temperatures in the 4–300 K range. The THz spectra of $\text{TbMn}_{0.96}\text{Fe}_{0.04}\text{O}_3$ for all possible E^ω - and H^ω -polarization configurations of the THz radiation are shown in Fig. S1 of Supplemental Material [42]. The absorption at THz frequencies is strongest in the $E^\omega \parallel a$ polarization, independently of the H^ω polarization, as it can be concluded from the results shown in Fig. S1. This result agrees with the one reported for TbMnO_3 [16,24] and other orthorhombic rare-earth manganites [22,26].

The $\text{Re}[\epsilon\mu]$ spectra can be divided into two main spectral ranges by a specific frequency, ω_b [see Figs. 3(a), 3(c), and 3(e)], which decreases from 44 cm^{-1} for TbMnO_3 , to 31 cm^{-1} in $\text{TbMn}_{0.96}\text{Fe}_{0.04}\text{O}_3$. Below 50 K, few degrees above T_N , $\text{Re}[\epsilon\mu]$ strongly increases for $\omega < \omega_b$, while it decreases

for $\omega > \omega_b$. Such behavior evidences an oscillator strength transfer mechanism from higher-frequency excitations to excitations in the $\omega < \omega_b$ range.

In diamagnetic paraelectrics, the dielectric loss, $\epsilon''(\omega)$, should be, in general, linearly dependent on frequency [$\epsilon''(\omega) \propto \omega$] far below phonon frequencies and $\lim_{\omega \rightarrow 0} \epsilon''(\omega) = 0$ [43]. The absorption background observed in Figs. 3(b), 3(d), and 3(f), is already seen in the loss spectra at room temperature as one (in case of TbMnO_3 , located at 22 cm^{-1}) or two (in case of $\text{TbMn}_{0.98}\text{Fe}_{0.02}\text{O}_3$ and $\text{TbMn}_{0.96}\text{Fe}_{0.04}\text{O}_3$, located at around $18\text{--}20$ and $50\text{--}55 \text{ cm}^{-1}$, respectively) broad and weak bands, whose intensity continuously increase on cooling. The absorption band in TbMnO_3 above T_C has been ascribed to a Debye-like relaxation [20,21]. The shape of the two bands in the THz spectra of the other two compounds cannot be described by an oscillator formula, neither by a Debye relaxation model. Instead, the absorption evidences more overdamped excitations. In TbMnO_3 , the absorption background rapidly increases on cooling below 50 K, and develops into two absorption bands, peaking near 20 and 40 cm^{-1} , respectively, below T_C . These bands are only observed in the $E^\omega \parallel a$ -polarized spectra, independently of magnetic H^ω orientation [10,16,19]. Similar temperature evolution is seen in the loss spectra of $\text{TbMn}_{1-x}\text{Fe}_x\text{O}_3$, $x = 0.02$ and 0.04 . The main difference is that the higher frequency band is present at all temperatures and its frequency exhibits larger temperature variation. According to Refs. [25,44], the lowest frequency excitation, seen near 20 cm^{-1} , is assigned to an electrically active Brillouin-zone boundary magnon (electromagnon), with wave vector $q = 2\pi/b$. [7,10] The results clearly evidence that the electromagnon persists in the Fe-substituted compounds, but with different properties relatively to that detected in TbMnO_3 , as it is already observed below T_N . The electromagnon character of this excitation is noticeable in the $\text{Re}[\epsilon\mu]$ spectra, which exhibit an increase at lower frequencies and decrease at higher frequencies, evidencing the dielectric strength transfer from polar phonons above 80 cm^{-1} to the electromagnon. These phonons are observed in the IR spectra and will be addressed later.

The highest frequency excitation needs a more detailed analysis. This excitation is observed in the paramagnetic phase, where no magnons are expected. Paraelectromagnons can exist in systems with short-range magnetic order [45], but recent muon spin relaxation studies (μSR) in $\text{TbMn}_{1-x}\text{Fe}_x\text{O}_3$, $x = 0$ and 0.02 , and neutron scattering experiments on $x = 0.02$ do not reveal any short-range magnetic correlations above T_N [33]. A more plausible explanation for the absorption near 40 cm^{-1} is the crystal-field excitation of the F_6 electron levels in Tb^{3+} . This crystal-field excitation was observed in inelastic neutron scattering [11,12,46] and in middle-IR studies [40]. Moreover, magnons seen in inelastic neutron-scattering pattern recorded at 17 K have frequencies of 50 and 65 cm^{-1} at $q = 2\pi/b$ [11] (i.e., wave vector of the predicted electromagnon), excluding the hypothesis that this band, seen near 40 cm^{-1} , originates from an electromagnon. While this excitation is weakly frequency dependent on TbMnO_3 , its frequency decreases from 55 to 40 cm^{-1} on cooling from 50 to 4 K, giving evidence for a gradual change

of crystalline environment of the Tb^{3+} cations. This change is also seen in the anomalous temperature dependence of lattice parameters [29,30].

The $E^\omega \perp a$ -polarized $\text{Re}[\epsilon\mu]$ spectra recorded at several temperatures, shown in Fig. 4, display a different temperature dependence. No spectral weight transfer is observed, unlike for $E^\omega \parallel a$. $\text{Re}[\epsilon\mu]$ decreases on cooling, especially below 60 cm^{-1} , but with different temperature rates which increase with increasing x . For $\text{TbMn}_{0.96}\text{Fe}_{0.04}\text{O}_3$, the $\text{Re}[\epsilon\mu]$ spectra exhibit a low-frequency band (peaking at around 12 cm^{-1} at 295 K), whose intensity decreases on cooling and eventually disappears below 75 K. The $\text{Im}[\epsilon\mu]$ spectra are nearly temperature independent above 100 K and below 50 K (see Fig. S2), respectively, while in the $50\text{--}100$ K range, a steep drop is observed, becoming more pronounced with increasing x (see Fig. S2).

An overdamped band, already observed at room temperature, develops near 18 cm^{-1} in the $E^\omega \perp a$ -polarized $\text{Im}[\epsilon\mu]$ spectra. Such band was reported in the paramagnetic phase of TbMnO_3 and other orthorhombic rare-earth manganites, having been assigned to a Debye-like relaxation [21]. Interestingly, the temperature evolution of this band is x dependent. In TbMnO_3 , on cooling, the band narrows and its intensity increases below 30 K; i.e, in the ferroelectric phase. The origin of this band in the $E^\omega \parallel c$ absorption spectra of TbMnO_3 [see Fig. 4(b)] is ascribed to a leakage from $E^\omega \parallel a$ spectra due to a small misorientation during the sample preparation. However, this band is very strong in the absorption spectra of $\text{TbMn}_{0.96}\text{Fe}_{0.04}\text{O}_3$, with an amplitude of the same order of magnitude as the low-frequency electromagnon band observed in the $E^\omega \parallel a$ -polarization spectra [see Fig. 3(f)], which excludes any leakage effect due to the sample misorientation. Moreover, another overdamped band develops at 52 cm^{-1} at room temperature and fades out on cooling, eventually disappearing below 50 K. This result is puzzling, because the disappearance of this second excitation occurs in the magnetically ordered phases. Interestingly, these bands becomes more intense as Fe content increases. Further studies are needed to understand the origin of this band.

C. Γ -point optical phonons

At room conditions, TbMnO_3 crystallizes in the orthorhombic $Pbnm$ structure. The irreducible representation decomposition for the Brillouin-zone center phonons is $\Gamma_{\text{phonon}} = 7A_g \oplus 8A_u \oplus 5B_{1g} \oplus 10B_{1u} \oplus 7B_{2g} \oplus 8B_{2u} \oplus 5B_{3g} \oplus 10B_{3u}$. The $9B_{1u}$, $9B_{3u}$, and $7B_{2u}$ modes are IR active for the electric field E^ω of IR radiation parallel to the a , b , and c axes, respectively, while the $7A_g$, $5B_{1g}$, $7B_{2g}$, and $5B_{3g}$ modes are Raman active and the remaining $8A_u$ modes are silent [18]. The low-level substitution of Mn by Fe locally breaks the symmetry while keeping the same overall $Pbnm$ space group for the mean crystallographic structure. Therefore, we shall assume the same decomposition of the irreducible representations of the Γ -point phonons for the Fe-substituted compounds.

1. Polar phonons in $\text{TbMn}_{0.98}\text{Fe}_{0.02}\text{O}_3$

In this subsection, we present the B_{1u} symmetry ($E^\omega \parallel a$ -polarized) infrared spectra of $\text{TbMn}_{0.98}\text{Fe}_{0.02}\text{O}_3$. We have

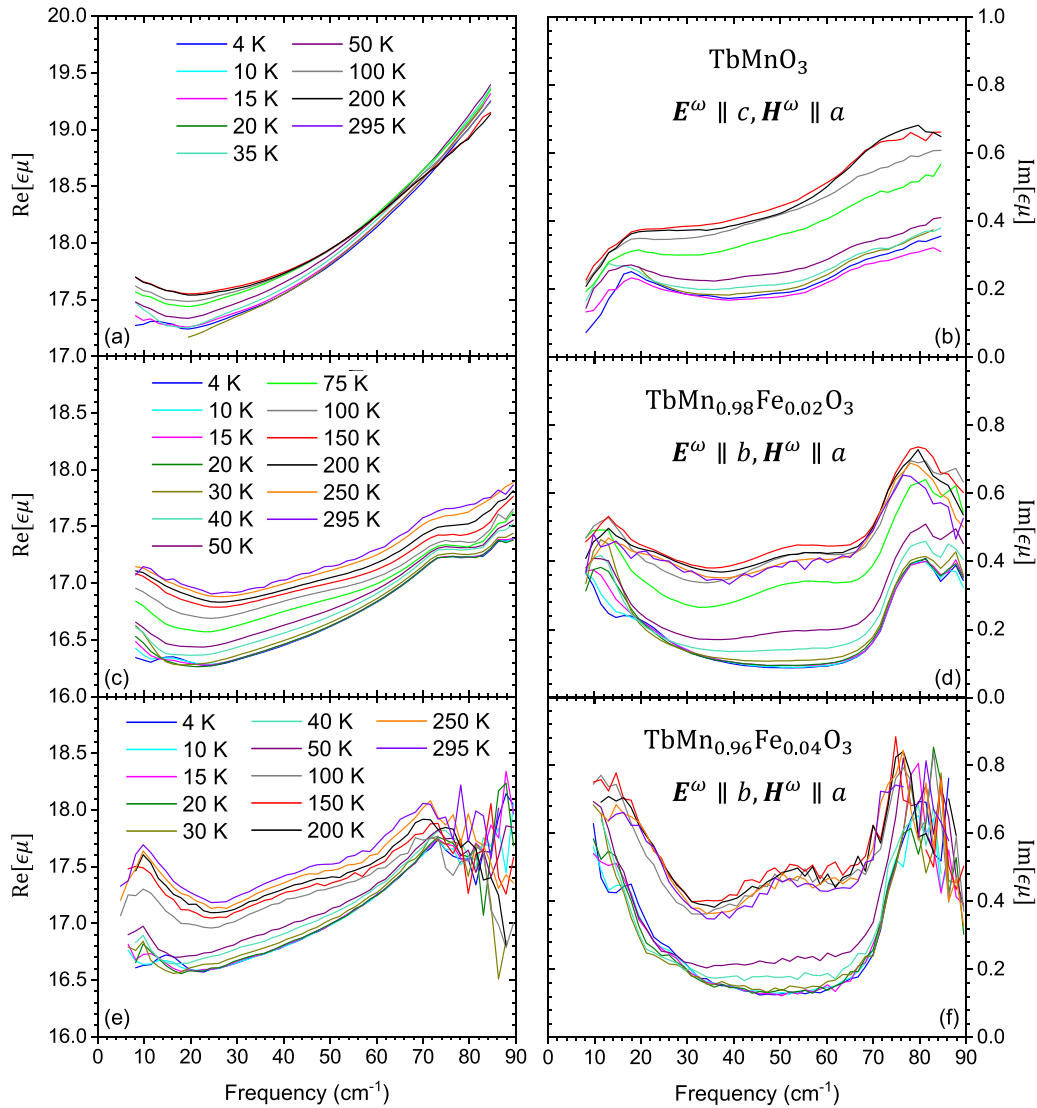


FIG. 4. Temperature dependence of the $\text{Re}[\epsilon\mu]$ and $\text{Im}[\epsilon\mu]$ spectra of TbMnO_3 (a), (b); $\text{TbMn}_{0.98}\text{Fe}_{0.02}\text{O}_3$ (c), (d); and $\text{TbMn}_{0.96}\text{Fe}_{0.04}\text{O}_3$ (e), (f). Spectra of TbMnO_3 were measured for the $\mathbf{E}^\omega \parallel c$ and $\mathbf{H}^\omega \parallel a$ polarization, while those of $\text{TbMn}_{0.98}\text{Fe}_{0.02}\text{O}_3$ and $\text{TbMn}_{0.96}\text{Fe}_{0.04}\text{O}_3$ correspond to the $\mathbf{E}^\omega \parallel b$ and $\mathbf{H}^\omega \parallel a$ polarization.

chosen this polarization as electromagnons are observed in THz spectra with the same polarization; consequently, the oscillator strength transfer from polar optical phonons to low-frequency excitations can be better studied. Since the $\mathbf{E}^\omega \parallel a$ -polarized THz spectra are independent of \mathbf{H}^ω polarization, the excitations in that frequency range contribute to permittivity and not to permeability. Therefore, in this section, we present the real (ϵ') and imaginary (ϵ'') parts of the complex dielectric spectra without considering the contribution of $\mu(\omega)$ to the IR signature.

Representative $\mathbf{E}^\omega \parallel a$ -polarized reflectivity spectra of $\text{TbMn}_{0.98}\text{Fe}_{0.02}\text{O}_3$ recorded at 4 and 250 K are shown in Fig. 5(a). The reflectivity spectra recorded in $\text{TbMn}_{0.98}\text{Mn}_{0.02}\text{O}_3$ resemble very well the ones observed for TbMnO_3 , evidencing the similar mean crystallographic structure for both compounds [17,18]. The plotted reflectivity below 85 cm^{-1} was calculated from the measured complex permittivity data in the THz range, through Eq. (3), while the higher-frequency IR spectra were directly measured.

Above 85 cm^{-1} , nine main reflectivity bands are observed, as expected from group theory, corresponding to the B_{1u} -symmetry phonons. However, four additional weak modes are needed to improve the quality of the fits; these additional modes are due to B_{2u} - and B_{3u} -symmetry phonons that appear in the spectra due to a slight misorientation of the sample. Two additional spectral components in the $125\text{--}155\text{-cm}^{-1}$ range, below 100 K, are assigned to crystal-field excitations [40]. The spectra of the real (ϵ') and imaginary (ϵ'') parts of the complex permittivity, obtained from the fits of Eq. (1) to the IR reflectivity spectra, are shown in Figs. 5(b) and 5(c), respectively. The peaks in $\epsilon''(\omega)$ correspond to the transverse optical phonons, at frequencies ω_{TO} , or to other polar excitations (e.g., crystal-field excitations or electromagnons).

Figure 6 shows the contour plot of the $\mathbf{E}^\omega \parallel a$ -polarized $\epsilon''(\omega)$ spectra of $\text{TbMn}_{0.98}\text{Mn}_{0.02}\text{O}_3$, which better evidences the temperature evolution of the polar excitations. On cooling from 300 K, several transversal optical phonons exhibit

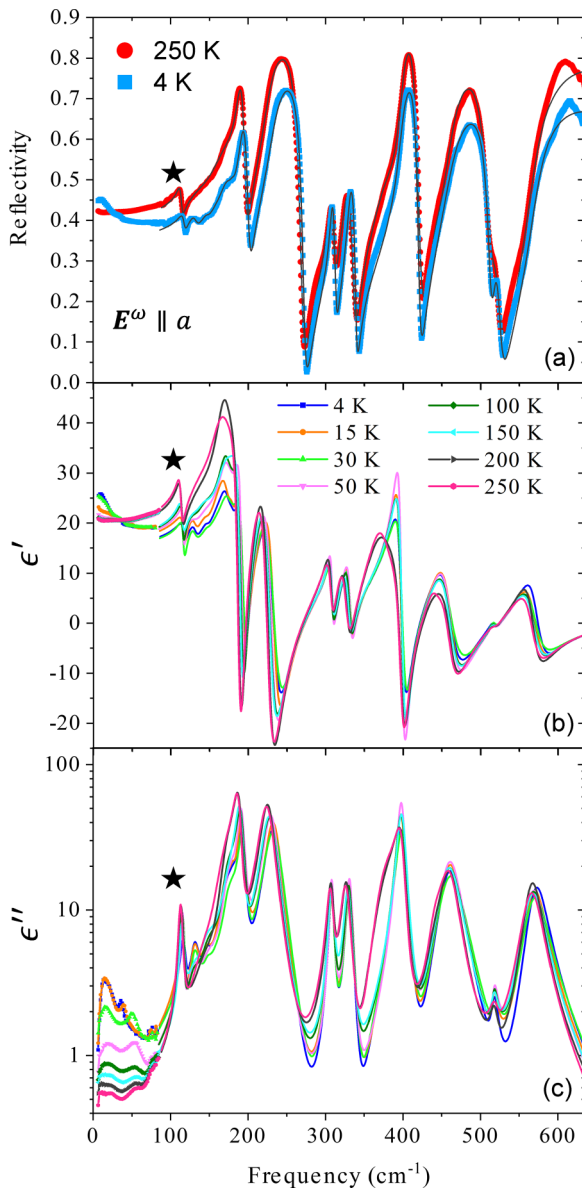


FIG. 5. (a) IR reflectivity spectra of $\text{TbMn}_{0.98}\text{Fe}_{0.02}\text{O}_3$ recorded at 4 and 250 K, for $E^\omega \parallel a$. Reflectivity below 85 cm^{-1} was calculated from the THz spectra. The corresponding fits are shown as dotted lines. (b) ϵ' and (c) ϵ'' spectra of $\text{TbMn}_{0.98}\text{Fe}_{0.02}\text{O}_3$ obtained from fitting the IR reflectivity at several temperatures. Low-frequency data seen below 85 cm^{-1} correspond to the experimental THz spectra. Polar phonon around 115 cm^{-1} is indicated by a star.

interesting changes. The collinear sinusoidal modulated antiferromagnetic magnetic phase transition at T_N is well signaled by the intensity decrease (about one order of magnitude) of the polar phonons observed in the $160\text{--}250\text{-}$ and $350\text{--}400\text{-cm}^{-1}$ spectral ranges. Interestingly, the phonon at around 400 cm^{-1} recovers intensity below $T_C = 18 \text{ K}$. A 50% dielectric strength reduction below T_N has been also reported for the lowest-frequency phonon in TbMnO_3 ($\sim 114 \text{ cm}^{-1}$ at 300 K), while the phonon at 404 cm^{-1} reduces its oscillator strength on cooling towards T_N , where the minimum value is reached, increasing its value on further cooling [16]. Although not clearly evident in Fig. 6, the polar phonon around 115 cm^{-1}

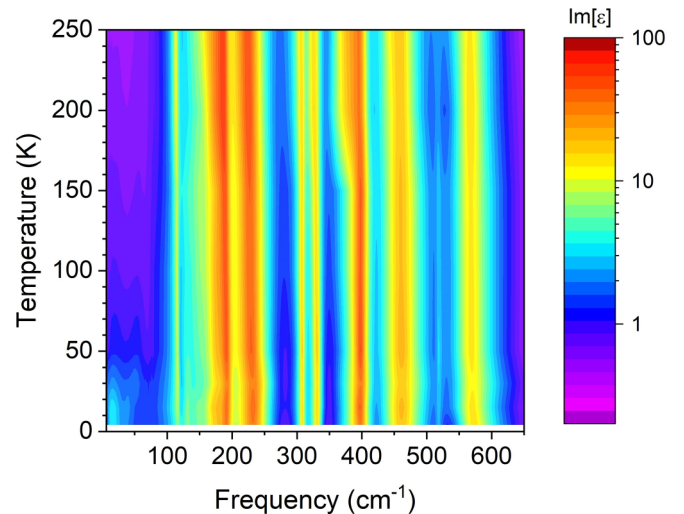


FIG. 6. Temperature evolution of the ϵ'' spectra of $\text{TbMn}_{0.98}\text{Fe}_{0.02}\text{O}_3$ for $E^\omega \parallel a$.

also decreases its dielectric strength on cooling below 100 K [see Fig. 5(c)]. These results give evidence for the dielectric strength transfer below 100 K from the polar phonons observed up to 250 cm^{-1} to the electromagnon and crystal-field excitations in $\text{TbMn}_{0.98}\text{Mn}_{0.02}\text{O}_3$. This evidences the coupling of all these excitations, which exhibit change of strength with temperature. Unfortunately, no lattice dynamic calculations of polar phonons in TbMnO_3 are reported to the best of our knowledge. So, considering their frequencies, we tentatively assign the bands showing decrease of dielectric strength to vibrations involving the oxygen atoms and the Mn/Fe cations. These results point towards distortions of the crystal lattice in the magnetic phase transitions, likely involving oxygen shifts.

Interesting changes in the IR spectra are also evident in the paramagnetic phase of $\text{TbMn}_{0.98}\text{Mn}_{0.02}\text{O}_3$. These are best observed in the $250\text{--}500\text{-cm}^{-1}$ range, where polar phonons involving vibrations of the oxygen atoms are expected. The main changes observed concern the oscillator strength changes; modes at 280 and 350 cm^{-1} decrease their oscillator strength below 175 K, while that of the mode at 398 cm^{-1} increases below this temperature. It is worth to stress that it is precisely this last mode that loses strength on entering in the collinear sinusoidal incommensurate modulated antiferromagnetic phase. The aforementioned results evidence oxygen octahedra distortions well above T_N , which is a well-known feature of TbMnO_3 , and therefore, independent of Fe substitution.

2. Raman modes

Representative unpolarized Raman spectra of $\text{TbMn}_{1-x}\text{Fe}_x\text{O}_3$, $x = 0, 0.02$, and 0.04 , recorded at 10 K in the $100\text{--}800\text{-cm}^{-1}$ spectral range, are shown in Fig. 7. The unpolarized Raman spectra recorded at several temperatures in the $10\text{--}300 \text{ K}$ range are found in Figs. S3, S4, and S5 (see Supplemental Material) [42]. The Raman signature of the three compositions here studied is rather similar, as a consequence of the similar structure of these compounds, as previously evidenced. The Raman mode assignment for

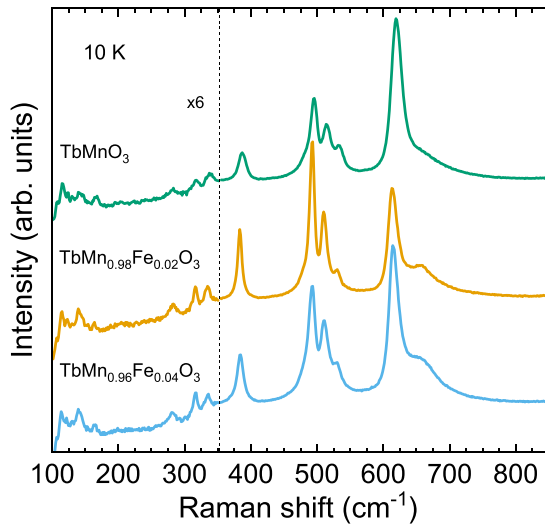


FIG. 7. Unpolarized Raman spectra of TbMnO_3 , $\text{TbMn}_{0.98}\text{Fe}_{0.02}\text{O}_3$, and $\text{TbMn}_{0.96}\text{Fe}_{0.04}\text{O}_3$ recorded at 10 K. Spectra below 354 cm^{-1} are multiplied by 6 for clarity.

TbMnO_3 has been published by various groups [47–49], and can be summarized as follows: the Raman-active phonons below 200 cm^{-1} are mainly characterized by vibrations of the heavy rare-earth ions and, above 300 cm^{-1} , by motions of the oxygen ions. The B -site atoms do not contribute for the phonons observed by Raman light scattering. The activation of new Raman bands is not observed in the ferroelectric phase transition at T_C , as it is common in magnetically driven ferroelectric materials. However, a detailed quantitative analysis of the Raman spectra reveals interesting temperature dependences of some phonon frequencies.

Figure 8 shows the temperature dependence of some selected Raman-active phonon frequencies in the three compositions here studied, which better mirror the structural deformations induced by temperature and the effect of the Fe substitution on their temperature dependence. The solid lines presented in Fig. 8 were determined from the best fit of Eq. (5) to the experimental data above 120 K and extrapolated to low temperatures. The low-frequency Raman bands at ~ 141 and $\sim 166\text{ cm}^{-1}$ are assigned to Tb oscillations along the a and c axes, respectively [47–49]. These phonons do not display anomalous temperature dependence in TbMnO_3 in all temperature ranges studied. On the contrary,

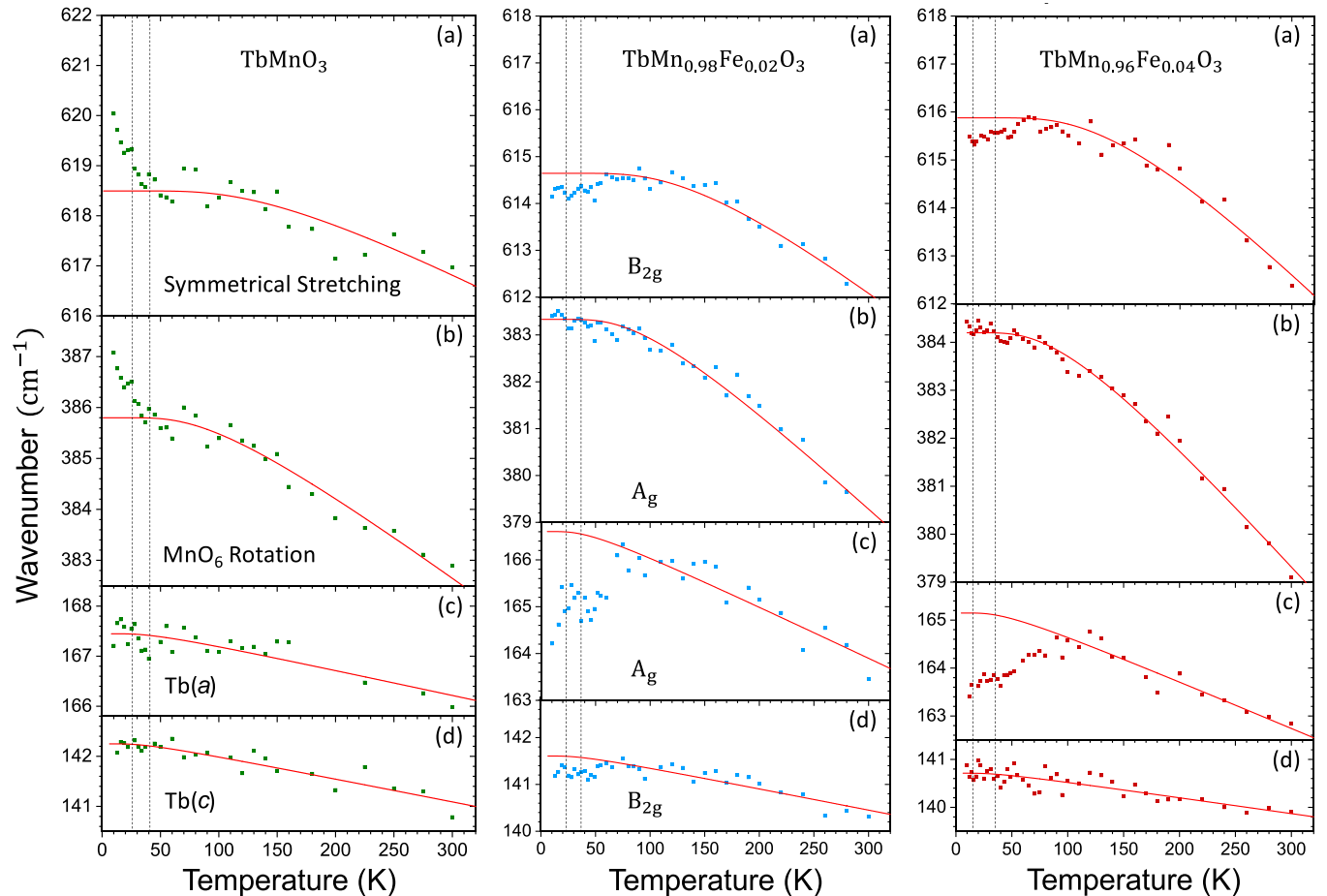


FIG. 8. Temperature dependence of the Raman mode frequencies for TbMnO_3 (left panel), $\text{TbMn}_{0.98}\text{Fe}_{0.02}\text{O}_3$ (middle panel), and $\text{TbMn}_{0.96}\text{Fe}_{0.04}\text{O}_3$ (right panel). Best fit with Eq. (5) in the temperature range where no anomalous behavior is observed is represented by a solid line and is extrapolated down to 0 K. $\text{Tb}(a)$ and $\text{Tb}(c)$ denote the Raman Tb^{3+} oscillations along the a and c axes, respectively. In each panel, the dashed line at the lowest temperature marks T_C while the other marks T_N .

both MnO_6 octahedra rotation (located near 379 cm^{-1}) and symmetrical stretching (located near 611 cm^{-1}) modes in TbMnO_3 show an upward deviation relatively to the anharmonic temperature behavior below T_N . In $\text{TbMn}_{0.98}\text{Fe}_{0.02}\text{O}_3$ and $\text{TbMn}_{0.96}\text{Fe}_{0.04}\text{O}_3$, a clear downward deviation from the anharmonic temperature dependence is ascertained for the $\text{Tb}(a)$ oscillations, just below 75 and 100 K, respectively. Moreover, the BO_6 octahedra rotation mode follows the normal temperature dependence in all temperature ranges, while the symmetrical stretching mode shows a downward deviation below 75 K. The BO_6 symmetrical stretching mode is known to be sensitive to the magnetic exchange integrals, as it involves changes in the $B\text{--O}2$ bond lengths. The upward/downward deviation demonstrates the relative balance between the ferromagnetic and antiferromagnetic interactions [50,51]. Regarding TbMnO_3 , the upward frequency shift has been interpreted as a manifestation of the prevalence of the antiferromagnetic interactions over the ferromagnetic ones [50,51]. Following the model, in Fe-substituted compounds the downshift observed is a consequence of the reinforcement of the ferromagnetic interactions against the antiferromagnetic ones.

IV. DISCUSSION

A. Reinforcement of the ferromagnetic interactions by Fe substitution

One of the outcomes of this work concerns the high sensitivity of the magnetic and polar orderings and their stability temperature range in TbMnO_3 due to partial substitution of Mn^{3+} by Fe^{3+} . We have found that the low-level isovalent substitution has a large impact on the balance between competitive ferro- and antiferromagnetic interactions in $\text{TbMn}_{1-x}\text{Fe}_x\text{O}_3$. The 4% level substitution of Mn^{3+} by Fe^{3+} results in the T_N decrease of 14%, and T_C of 48%. Considering that $\text{TbMn}_{0.95}\text{Fe}_{0.05}\text{O}_3$ does not exhibit ferroelectric phase but a weak ferromagnetic behavior [35], the results here reported give clear evidence for the reinforcement of the ferromagnetic interactions against the antiferromagnetic ones, and the consequent destabilization of the antiferromagnetic orders with increasing x up to 0.04. This interpretation is also corroborated by the decreasing $T_N/|\Theta_p|$ ratio with increasing Fe content, and the crossover between up- to downshifts observed in the BO_6 symmetrical-stretching Raman-active phonons, as it was pointed out before. The decrease of the maximum electric polarization at lowest temperature as x increases is also an indirect proof of the spin structure changes induced by Fe^{3+} in the crystal lattice. Indeed, according to the Dzyaloshinskii-Moriya model, the polarization magnitude decrease is a direct consequence of less-tilted neighbor spins in the cycloidal modulated antiferromagnetic phase. The high sensitivity of the electric polarization to the low substitution level results from the rather large static magnetoelectric coupling in these materials.

B. Magnetoelectric and crystal-field excitations in $\text{TbMn}_{1-x}\text{Fe}_x\text{O}_3$, $0 \leq x \leq 0.04$

Low-level Fe substitution also has relevant effects on the dynamic magnetoelectric excitations in $\text{TbMn}_{1-x}\text{Fe}_x\text{O}_3$, $0 \leq$

$x \leq 0.04$. The results corroborate that the magnetoelectric excitations are strictly tied to crystal lattice, although the substitution of Mn^{3+} by Fe^{3+} alters their activity and temperature dependence.

Clear evidence for a dynamic magnetoelectric contribution to the THz spectra is found for the three compounds, but with different properties. In TbMnO_3 , the low-energy electromagnon band peaks at 20 cm^{-1} and it is observed in the $\mathbf{E}^\omega \parallel a$ -polarized THz spectra, in agreement with the selection rule for exchange-striction activated electromagnons [24]. Its intensity is large in the cycloidal modulated antiferromagnetic phase, which is also ferroelectric and, as temperature approaches T_C from below, the electromagnon band intensity monotonously decreases and fades out above T_C . The THz signal observed above T_C exhibits a rather overdamped excitation that has been described as a Debye-like relaxation [21]. The electromagnon band is also observed around 20 cm^{-1} in the $\mathbf{E}^\omega \parallel a$ -polarized THz spectra of $\text{TbMn}_{1-x}\text{Fe}_x\text{O}_3$, $x = 0.02$ and 0.04, but in both the cycloidal modulated antiferromagnetic and ferroelectric phase, and the collinear sinusoidal modulated antiferromagnetic and paraelectric phase. The electromagnon band disappears above T_N , with two broad and weak absorption bands up to 300 K remaining; instead, one as is observed in TbMnO_3 . The existence of the electromagnon band below T_N in $\text{TbMn}_{0.98}\text{Fe}_{0.02}\text{O}_3$ and $\text{TbMn}_{0.96}\text{Fe}_{0.04}\text{O}_3$ compounds gives clear evidence for the different origin of this excitation in the Fe-substituted compounds. According to the current models, the electromagnon in TbMnO_3 arises in the dielectric spectra due to exchange-striction mechanism ($\propto \vec{S}_i \cdot \vec{S}_j$) [24,25]. Exchange-striction activated electromagnons have been observed even in the paraelectric phases of $\text{Ba}_2\text{Mg}_2\text{Fe}_{12}\text{O}_{22}$ [52] and $\text{CuFe}_{1-x}\text{Ga}_x\text{O}_2$ [53], which exhibit proper screw and collinear magnetic ordering, respectively. Therefore, the activation of electromagnons is not necessarily tied to spin-induced ferroelectric phases. The results here presented for the Fe-substituted TbMnO_3 compounds clearly evidence the large impact that low-level Mn substitution by Fe^{3+} has in the magnetic structure and, consequently, in the mechanisms underlying the electromagnon activation.

The observation of the overdamped component in the THz spectra of TbMnO_3 , at 20 cm^{-1} , and of $\text{TbMn}_{0.98}\text{Fe}_{0.02}\text{O}_3$ and $\text{TbMn}_{0.96}\text{Fe}_{0.04}\text{O}_3$, at around 18–20 and 50–55 cm^{-1} , above T_N should not have magnetic origin. In fact, recent temperature and transverse magnetic field μSR studies in TbMnO_3 [33], performed by the authors, exclude any short- (and long)-range magnetic ordering above T_N , in agreement with inelastic neutron-scattering experiments [11,12].

The second polar absorption component, developing in the THz spectra of TbMnO_3 below T_C , near 40 cm^{-1} , has been tentatively assigned to a Brillouin-zone boundary electromagnon, with wave vector $q = 2\pi/b - 2q_m$ [12,24,25]. Nevertheless, inelastic neutron-scattering studies in TbMnO_3 revealed magnons with higher frequencies at this wave vector [11]. In fact, Takahashi *et al.* [16] reported a second electromagnon excitation near 60 cm^{-1} in TbMnO_3 . The excitation we detect in this work is 20 cm^{-1} lower, which excludes its assignment to an electromagnon. Following Mansouri *et al.* [40], q -independent crystal-field excitations have been observed in TbMnO_3 , one of them having rather sim-

ilar frequency as to this second broad component, which enable us to assign this component to a crystal-field excitation. Similar component is also observed in the THz spectra of $\text{TbMn}_{0.98}\text{Fe}_{0.02}\text{O}_3$ and $\text{TbMn}_{0.96}\text{Fe}_{0.04}\text{O}_3$, developing around 55 and 50 cm^{-1} , respectively, below 100 K. Interestingly, the crystal-field excitation reveals a 15 cm^{-1} downshift on cooling that is not seen in pure TbMnO_3 . The shift of crystal-field excitation frequency can be understood as a consequence of the thermal occupation of the excited crystal-field levels of Tb^{3+} and concomitant changes in atomic environment around the Tb^{3+} site. This causes lattice distortions and explains the observed anomalous thermal expansion of the lattice on cooling [30]. We currently have no explanation for the absence of the second electromagnon in the THz spectrum of TbMnO_3 .

The $E^\omega \perp a$ -polarized THz absorption spectra are almost temperature independent above 100 K and below 50 K. However, an abrupt decrease in absorption on cooling from 100 to 50 K is observed, with change rate that increases with increasing x . A similar decrease of absorption was observed (but not explained) by Takahashi *et al.* in pure TbMnO_3 [16]. This absorption cannot be ascribed to magnetic excitations above T_N , as it was previously explained, and also because this would instead lead to an increase in losses with decreasing temperature below T_N . The broad absorption peaking near 50 cm^{-1} in the $E^\omega \parallel b$ -polarized absorption spectra above 100 K likely originates from a two-phonon difference process, which expires below 40 K, when the zone-boundary acoustic phonons involved in this process are no longer thermally populated. The spectral component at 80 cm^{-1} is clearly seen at all temperatures in the absorption spectra of both $\text{TbMn}_{0.98}\text{Fe}_{0.02}\text{O}_3$ and $\text{TbMn}_{0.96}\text{Fe}_{0.04}\text{O}_3$, which is assigned to a crystal-field excitation [40]. The origin of the band near 12 cm^{-1} in $E^\omega \parallel b$ -polarized absorption spectra of Fe-substituted compounds is not clear. The existence of this band in both $E^\omega \parallel a$ and $E^\omega \parallel b$ absorption spectra of $\text{TbMn}_{0.96}\text{Fe}_{0.04}\text{O}_3$ points at a deep change in the magnetic structure, induced by the Mn^{3+} substitution by Fe^{3+} .

The intensity transfer observed in the $E^\omega \parallel a$ -polarized absorption spectra can be quantitatively described by looking at the low-frequency infrared spectra displayed in Fig. 9. The lowest-frequency band assigned to an optical phonon at $\sim 115 \text{ cm}^{-1}$ (marked in Fig. 9 by a star) loses intensity on cooling, while the electromagnon and the crystal-field excitation gain strength at low temperatures. To quantitatively analyze the intensity transfer, we calculated the spectral weight of these two excitations through the equation [16]

$$S = \frac{2m_0V}{\pi e^2} \int_{\omega_1}^{\omega_2} \omega \epsilon''(\omega) d\omega, \quad (6)$$

where m_0 , e , and V are the free-electron mass, electron charge, and primitive unit-cell volume, respectively. The temperature dependence of the spectral weight change relatively to the value at 250 K, $\Delta S = S(T) - S(250 \text{ K})$, is depicted in the inset of Fig. 9 for the electromagnon plus crystal-field excitation, and the lowest-energy polar phonon. The spectral weight was calculated in the frequency ranges $(\omega_1, \omega_2) = (8, 70)$ and $(90, 123) \text{ cm}^{-1}$ for the electromagnons (region I) and phonon (region II), respectively. The spectral weight of the electromagnon and crystal-field excitation considerably increases below 150 K. It is also below that temperature that

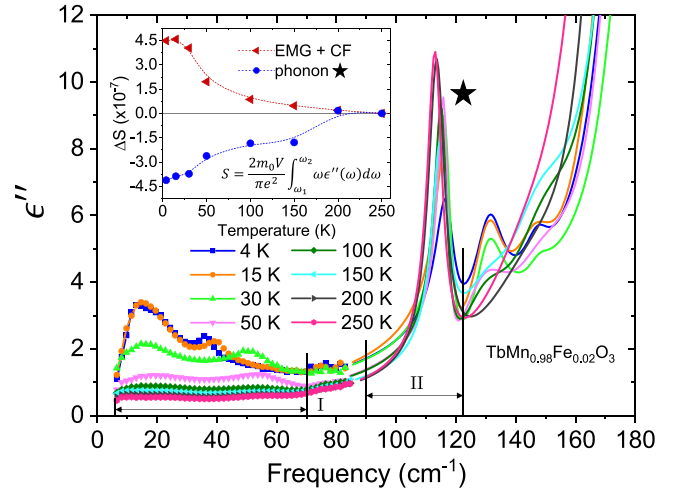


FIG. 9. Temperature dependence of the ϵ'' spectra for $E^\omega \parallel a$ of $\text{TbMn}_{0.98}\text{Fe}_{0.02}\text{O}_3$ up to 180 cm^{-1} . Inset: Temperature dependence of the change in spectral weight [Eq. (6)] of the electromagnon (EMG) plus crystal-field (CF) excitation and the lowest-lying optical phonon around 115 cm^{-1} (signaled by a star) from their values at 250 K.

the lowest-lying optical phonon exhibits a decrease in spectral weight. Indeed, it can be seen from the inset of Fig. 9 that the change in spectral weight of the phonon largely accounts for that of the electromagnon and crystal-field excitation. This is consistent with what was previously reported in TbMnO_3 [16]. Moreover, Fig. 6 shows that not only the phonon near 115 cm^{-1} transfers its strength to the THz excitation. Also, the phonons near 190, 240, and 400 cm^{-1} reduce their intensities below T_N , indicating their coupling with electromagnon and crystal-field excitations at 40 and 135 cm^{-1} .

C. What happens in the paramagnetic phase?

The experiment results here reported evidence interesting changes in the magnetization and lattice distortions, mirrored by both IR and Raman-active phonons, in all compounds in the paramagnetic phase, well above T_N . Such observations were reported in TbMnO_3 , but their explanation is still controversial. Our results show that the Fe substitution has strong impact on the low-temperature magnetic and ferroelectric phases, but not in the temperature dependence of the magnetization in the paramagnetic phase. Anomalous temperature dependence of the magnetization, Raman-active phonons, and lattice parameters have been also reported at 150 K in TbFeO_3 , well within its antiferromagnetic phase ($T_N = 650 \text{ K}$) [34]. From these observations, we conclude that the changes in both magnetization and crystal lattice are due to the Tb^{3+} and/or O^{2-} atoms. The temperature variations observed in the oscillator strength of the polar optical phonons, in the spectral range where oxygen motions contribute to the lattice vibrations, evidence octahedra deformations involving oxygen atoms in the paramagnetic phase. The anomalous temperature dependence of the lattice parameters, ascertained for both TbMnO_3 and TbFeO_3 , supports the existence of such deformations. Therefore, we propose that oxygen shifts occur around 200 K. The oxygen movements can be explained by the different temperature occupancy of the crystal-field

electronic Tb^{3+} levels. The oxygen movements explain the changes on the superexchange integrals and, consequently, the abnormal temperature dependence of magnetization above T_N .

The Mn^{3+} substitution by Fe^{3+} has another interesting effect on the coupling between different lattice and electronic excitations in the paramagnetic phase. Regarding the temperature dependence of the Raman-active Tb^{3+} oscillations, significant deviations of the frequency of the $\text{Tb}(a)$ oscillations are observed only in Fe-substituted compounds, just below 100 K, while no deviations could be ascertained in TbMnO_3 . These deviations not only mirror the anisotropy in these compounds but also show a strong interplay between Tb^{3+} and Fe^{3+} spins, as in TbFeO_3 [54], even at small concentrations ($x < 0.05$).

V. CONCLUSIONS

This work evidences the deep influence of the Mn^{3+} substitution by Fe^{3+} in the low-temperature magnetic phase sequence, static and dynamic magnetoelectricity, spin structure and ferroelectricity, as well as spin-phonon coupling in $\text{TbMn}_{1-x}\text{Fe}_x\text{O}_3$ ($0 \leq x \leq 0.04$). This substitution is found to reinforce the ferromagnetic interactions against the antiferromagnetic ones, leading to a decrease of both magnetic phase transition temperatures and to the spin-structure changes that allows for electric polarization. As Fe^{3+} concentration increases up to 4%, the spin-structure helicity decreases, and the maximum electric polarization magnitude decreases as a consequence.

The low-energy electromagnon excitation is found to be rather strong in the paraelectric and magnetic collinear sinusoidal antiferromagnetic phase in the Fe-substituted compounds, contrarily to TbMnO_3 . The activation of electromagnon in the spin-collinear phase can be understood in

the framework of the exchange-striction mechanism, and corroborates the change of the magnetic structure induced by the presence of Fe^{3+} in the lattice, enabling the activation of electromagnon in the paraelectric and collinear sinusoidal modulated antiferromagnetic phase, stable between T_C and T_N .

Traces of the Debye-like background and crystal-field absorption remain in the THz spectra up to room temperature. A detailed analysis of IR reflectivity spectra revealed that the spectral weight of the THz excitations in $\text{TbMn}_{0.98}\text{Fe}_{0.02}\text{O}_3$ mainly originates from the lowest-lying optical phonon near 115 cm^{-1} , as previously reported for pure TbMnO_3 . The mode near 135 cm^{-1} is assigned to a crystal-field excitation, which receives its dielectric strength from phonons up to 400 cm^{-1} . Raman spectra reveal a spin-phonon coupling above T_N , in the Fe-substituted compounds.

The abnormal temperature dependence of magnetization around 200 K is explained by changes in the crystal-field electronic levels of Tb^{3+} and oxygen shifts. This evidences a magnetoelastic coupling in the studied materials, even in the paramagnetic phase.

ACKNOWLEDGMENTS

This work was supported by Scientific Grant Agency MŠVVaŠ SR and SAS Project No. VEGA 2/0011/22; the Czech Science Foundation (Project No. 21–06802S); the MŠMT Projects No. SOLID 21- CZ.02.1.01/0.0/0.0/16_-019/0000760, No. PTDC/FIS-MAC/29454/2017, No. NORTE/01/0145/FEDER/028538, and No. IFIMUP: Norte-070124-FEDER-000070; and NECL: Grants No. NORTE-01-0145- FEDER-022096, No. UIDB/04968/2020, and No. UIDB/04968/2020.

The authors declare no competing interests.

-
- [1] Y. Tokura, S. Seki, and N. Nagaosa, Multiferroics of spin origin, *Rep. Prog. Phys.* **77**, 076501 (2014).
 - [2] S. Dong, J. M. Liu, S. W. Cheong, and Z. Ren, Multiferroic materials and magnetoelectric physics: Symmetry, entanglement, excitation, and topology, *Adv. Phys.* **64**, 519 (2015).
 - [3] D. Khomskii, Classifying multiferroics: Mechanisms and effects, *Physics* **2**, 20 (2009).
 - [4] T. Kimura, T. Goto, H. Shintani, K. Ishizaka, T. Arima, and Y. Tokura, Magnetic control of ferroelectric polarization, *Nature (London)* **426**, 55 (2003).
 - [5] M. Balkanski, R. F. Wallis, and E. Haro, Anharmonic effects in light scattering due to optical phonons in silicon, *Phys. Rev. B* **28**, 1928 (1983).
 - [6] S. B. Wilkins *et al.*, Nature of the Magnetic Order and Origin of Induced Ferroelectricity in TbMnO_3 , *Phys. Rev. Lett.* **103**, 207602 (2009).
 - [7] A. B. Harris, J. W. Lynn, M. Kenzelmann, C. Broholm, O. P. Vajk, C. L. Zhang, S.-W. Cheong, S. B. Kim, J. Schefer, and S. Jonas, Magnetic Inversion Symmetry Breaking and Ferroelectricity in TbMnO_3 , *Phys. Rev. Lett.* **95**, 087206 (2005).
 - [8] I. A. Sergienko and E. Dagotto, Role of the Dzyaloshinskii-Moriya interaction in multiferroic perovskites, *Phys. Rev. B* **73**, 094434 (2006).
 - [9] H. Katsura, N. Nagaosa, and A. V. Balatsky, Spin Current and Magnetoelectric Effect in Noncollinear Magnets, *Phys. Rev. Lett.* **95**, 057205 (2005).
 - [10] A. Pimenov, A. A. Mukhin, V. Y. Ivanov, V. D. Travkin, A. M. Balbashov, and A. Loidl, Possible evidence for electromagnons in multiferroic manganites, *Nat. Phys.* **2**, 97 (2006).
 - [11] D. Senff, P. Link, K. Hradil, A. Hiess, L. P. Regnault, Y. Sidis, N. Aliouane, D. N. Argyriou, and M. Braden, Magnetic Excitations in Multiferroic TbMnO_3 : Evidence for a Hybridized Soft Mode, *Phys. Rev. Lett.* **98**, 137206 (2007).
 - [12] D. Senff, N. Aliouane, D. N. Argyriou, A. Hiess, L. P. Regnault, P. Link, K. Hradil, Y. Sidis, and M. Braden, Magnetic excitations in a cycloidal magnet: The magnon spectrum of multiferroic TbMnO_3 , *J. Phys.: Condens. Matter* **20**, 434212 (2008).
 - [13] J. S. Lee, N. Kida, S. Miyahara, Y. Takahashi, Y. Yamasaki, R. Shimano, N. Furukawa, and Y. Tokura, Systematics of electromagnons in the spiral spin-ordered states of RMnO_3 , *Phys. Rev. B* **79**, 180403 (2009).
 - [14] P. Rovillain, M. Cazayous, Y. Gallais, A. Sacuto, M. A. Measson, and H. Sakata, Magnetoelectric excitations in multiferroic TbMnO_3 by Raman scattering, *Phys. Rev. B* **81**, 054428 (2010).

- [15] P. Rovillain, J. Liu, M. Cazayous, Y. Gallais, M. A. Measson, H. Sakata, and A. Sacuto, Electromagnon and phonon excitations in multiferroic TbMnO₃, *Phys. Rev. B* **86**, 014437 (2012).
- [16] Y. Takahashi, N. Kida, Y. Yamasaki, J. Fujioka, T. Arima, R. Shimano, S. Miyahara, M. Mochizuki, N. Furukawa, and Y. Tokura, Evidence for an Electric-Dipole Active Continuum Band of Spin Excitations in Multiferroic TbMnO₃, *Phys. Rev. Lett.* **101**, 187201 (2008).
- [17] M. Schmidt, C. Kant, T. Rudolf, F. Mayr, A. A. Mukhin, A. M. Balbashov, J. Deisenhofer, and A. Loidl, Far-infrared optical excitations in multiferroic TbMnO₃, *Eur. Phys. J. B* **71**, 411 (2009).
- [18] R. Schleck, R. L. Moreira, H. Sakata, and R. P. S. M. Lobo, Infrared reflectivity of the phonon spectra in multiferroic TbMnO₃, *Phys. Rev. B* **82**, 144309 (2010).
- [19] A. Pimenov, A. Shuvaev, A. Loidl, F. Schrettle, A. A. Mukhin, V. D. Travkin, V. Yu. Ivanov, and A. M. Balbashov, Magnetic and Magnetoelectric Excitations in TbMnO₃, *Phys. Rev. Lett.* **102**, 107203 (2009).
- [20] A. M. Shuvaev, A. A. Mukhin, and A. Pimenov, Magnetic and magnetoelectric excitations in multiferroic manganites, *J. Phys.: Condens. Matter* **23**, 113201 (2011).
- [21] A. Pimenov, A. M. Shuvaev, A. A. Mukhin, and A. Loidl, Electromagnons in multiferroic manganites, *J. Phys.: Condens. Matter* **20**, 434209 (2008).
- [22] N. Kida, Y. Takahashi, J. S. Lee, R. Shimano, Y. Yamasaki, Y. Kaneko, S. Miyahara, N. Furukawa, T. Arima, and Y. Tokura, Terahertz time-domain spectroscopy of electromagnons in multiferroic perovskite manganites [Invited], *J. Opt. Soc. Am. B* **26**, A35 (2009).
- [23] A. M. Shuvaev, V. D. Travkin, V. Y. Ivanov, A. A. Mukhin, and A. Pimenov, Evidence for Electroactive Excitation of the Spin Cycloid in TbMnO₃, *Phys. Rev. Lett.* **104**, 097202 (2010).
- [24] R. Valdés Aguilar, M. Mostovoy, A. B. Sushkov, C. L. Zhang, Y. J. Choi, S. W. Cheong, and H. D. Drew, Origin of Electromagnon Excitations in Multiferroic RMnO₃, *Phys. Rev. Lett.* **102**, 047203 (2009).
- [25] M. P. V. Stenberg, and R. de Sousa, Model for twin electromagnons and magnetically induced oscillatory polarization in multiferroic RMnO₃, *Phys. Rev. B* **80**, 094419 (2009).
- [26] Y. Takahashi, R. Shimano, Y. Kaneko, H. Murakawa, and Y. Tokura, Magnetoelectric resonance with electromagnons in a perovskite helimagnet, *Nat. Phys.* **8**, 121 (2012).
- [27] N. Kida, Y. Ikebe, Y. Takahashi, J. P. He, Y. Kaneko, Y. Yamasaki, R. Shimano, T. Arima, N. Nagaosa, and Y. Tokura, Electrically driven spin excitation in the ferroelectric magnet DyMnO₃, *Phys. Rev. B* **78**, 104414 (2008).
- [28] D. O'Flynn, M. R. Lees, and G. Balakrishnan, Magnetic susceptibility and heat capacity measurements of single crystal TbMnO₃, *J. Phys.: Condens. Matter* **26**, 256002 (2014).
- [29] J. Blasco, C. Ritter, J. García, J. M. de Teresa, J. Pérez-Cacho, and M. R. Ibarra, Structural and magnetic study of Tb_{1-x}Ca_xMnO₃ perovskites, *Phys. Rev. B* **62**, 5609 (2000).
- [30] K. Berggold, J. Baier, D. Meier, J. A. Mydosh, T. Lorenz, J. Hemberger, A. Balbashov, N. Aliouane, and D. N. Argyriou, Anomalous thermal expansion and strong damping of the thermal conductivity of NdMnO₃ and TbMnO₃ due to 4f crystal-field excitations, *Phys. Rev. B* **76**, 094418 (2007).
- [31] S. Issing, A. Pimenov, Y. V. Ivanov, A. A. Mukhin, and J. Geurts, Spin-phonon coupling in multiferroic manganites RMnO₃: Comparison of pure (R = Eu, Gd, Tb) and substituted (R = Eu_{1-x}Y_x) compounds, *Eur. Phys. J. B* **78**, 367 (2010).
- [32] S. Elsässer, M. Schiebl, A. A. Mukhin, A. M. Balbashov, A. Pimenov, and J. Geurts, Impact of temperature-dependent local and global spin order in RMnO₃ compounds for spin-phonon coupling and electromagnon activity, *New J. Phys.* **19**, 013005 (2017).
- [33] R. Vilarinho, R. C. Vilão, H. V. Alberto, A. G. Marinopoulos, J. M. Gil, H. Luetkens, Z. Guguchia, R. Scheuermann, M. Mihalik, M. Zentkova, and J. Agostinho Moreira (unpublished).
- [34] R. Vilarinho, M. C. Weber, M. Guennou, A. C. Miranda, C. Dias, P. Tavares, J. Kreisel, A. Almeida, and J. A. Moreira, Magnetostructural coupling in RFeO₃ (R = Nd, Tb, Eu and Gd), *Sci. Rep.* **12**, 9697 (2022).
- [35] R. Vilarinho, E. Queirós, D. J. Passos, D. A. Mota, P. B. Tavares, M. Mihalik, M. Zentkova, M. Mihalik, A. Almeida, and J. A. Moreira, On the ferroelectric and magnetoelectric mechanisms in low Fe³⁺ doped TbMnO₃, *J. Magn. Magn. Mater.* **439**, 167 (2017).
- [36] M. Mihalik, M. Mihalik, Z. Jagličić, R. Vilarinho, J. A. Moreira, E. Queiros, P. B. Tavares, A. Almeida, and M. Zentková, Magnetic phase diagram of the TbMn_{1-x}Fe_xO₃ solid solution system, *Physica B Condens. Matter* **506**, 163 (2017).
- [37] V. Skoromets, C. Kadlec, H. Němec, D. Fattakhova-Rohlfing, and P. Kužel, Tunable dielectric properties of KTaO₃ single crystals in the terahertz range, *J. Phys. D: Appl. Phys.* **49**, 065306 (2016).
- [38] F. Gervais, High-temperature infrared reflectivity spectroscopy by scanning interferometry, in *Infrared and Millimeter Waves V8: Electromagnetic Waves in Matter*, edited by K. J. Button, 1st ed. (Elsevier Science & Technology Books, Amsterdam, 1983), Chap. 7, p. 279.
- [39] W. Hayes and R. Loudon, *Scattering of Light by Crystals* (John Wiley & Sons, New York, 1978), Vol. 47.
- [40] S. Mansouri, S. Jandl, M. Balli, P. Fournier, A. A. Mukhin, V. Y. Ivanov, A. Balbashov, and M. Orlita, Study of crystal-field excitations and infrared active phonons in TbMnO₃, *J. Phys.: Condens. Matter* **30**, 175602 (2018).
- [41] M. Mihalik, M. Mihalik, M. Zentková, A. Maia, R. Vilarinho, A. Almeida, J. Agostinho Moreira, J. Pospíšil, and K. Uhlířová, Magnetic properties of TbMn_{0.98}Fe_{0.02}O₃ single crystal, *J. Magn. Magn. Mater.* **549**, 168986 (2022).
- [42] See Supplemental Material at <http://link.aps.org/supplemental/10.1103/PhysRevB.107.104410> for THz spectra recorded at different temperatures for all polarization configurations of the THz radiation, temperature dependence of the imaginary part of the complex optical index at 55 cm⁻¹ for all compounds, and representative unpolarized Raman spectra of all compounds recorded at several temperatures.
- [43] S. Kamba, D. Noujmi, A. Pashkin, J. Petzelt, R. C. Pullar, A. K. Axelsson, and N. McN. Alford, Low-temperature microwave and THz dielectric response in novel microwave ceramics, *J. Eur. Ceram. Soc.* **26**, 1845 (2006).
- [44] M. P. V. Stenberg, and R. de Sousa, Sinusoidal electromagnon in RMnO₃: Indication of anomalous magnetoelectric coupling, *Phys. Rev. B* **85**, 104412 (2012).
- [45] F. Kadlec, V. Goian, C. Kadlec, M. Kempa, P. Vaněk, J. Taylor, S. Rols, J. Prokleška, M. Orlita, and S. Kamba, Possible coupling between magnons and phonons in multiferroic CaMn₇O₁₂, *Phys. Rev. B* **90**, 054307 (2014).

- [46] R. Kajimoto, H. Mochizuki, H. Yoshizawa, H. Shintani, T. Kimura, and Y. Tokura, R-dependence of spin exchange interactions in RMnO_3 ($R = \text{Rare-Earth Ions}$), *J. Phys. Soc. Jpn.* **74**, 2430 (2005).
- [47] M. N. Iliev, M. V. Abrashev, J. Laverdière, S. Jandl, M. M. Gospodinov, Y. Q. Wang, and Y. Y. Sun, Distortion-dependent Raman spectra and mode mixing in RMnO_3 perovskites ($R = \text{La, Pr, Nd, Sm, Eu, Gd, Tb, Dy, Ho, Y}$), *Phys. Rev. B* **73**, 064302 (2006).
- [48] J. Laverdière, S. Jandl, A. A. Mukhin, and V. Y. Ivanov, Raman study of orbital mediated multiphonons in RMnO_3 ($R = \text{Pr, Sm, Eu, Tb, Y}$), *Eur. Phys. J. B* **54**, 67 (2006).
- [49] S. Mansouri, S. Jandl, A. Mukhin, V. Y. Ivanov, and A. Balbashov, A comparative Raman study between PrMnO_3 , NdMnO_3 , TbMnO_3 and DyMnO_3 , *Sci. Rep.* **7**, 13796 (2017).
- [50] W. Baltensperger and J. S. Helman, Influence of magnetic order in insulators on the optical phonon frequency, *Helv. Phys. Acta* **41**, 668 (1968).
- [51] K. Wakamura and T. Arai, Effect of magnetic ordering on phonon parameters for infrared active modes in ferromagnetic spinel CdCr_2S_4 , *J. Appl. Phys.* **63**, 5824 (1988).
- [52] N. Kida, D. Okuyama, S. Ishiwata, Y. Taguchi, R. Shimano, K. Iwasa, T. Arima, and Y. Tokura, Electric-dipole-active magnetic resonance in the conical-spin magnet $\text{Ba}_2\text{Mg}_2\text{Fe}_{12}\text{O}_{22}$, *Phys. Rev. B* **80**, 220406(R) (2009).
- [53] S. Seki, N. Kida, S. Kumakura, R. Shimano, and Y. Tokura, Electromagnons in the Spin Collinear State of a Triangular Lattice Antiferromagnet, *Phys. Rev. Lett.* **105**, 097207 (2010).
- [54] M. C. Weber, M. Guennou, H. J. Zhao, J. Íñiguez, R. Vilarinho, A. Almeida, J. A. Moreira, and J. Kreisel, Raman spectroscopy of rare-earth orthoferrites RFeO_3 ($R = \text{La, Sm, Eu, Gd, Tb, Dy}$), *Phys. Rev. B* **94**, 214103 (2016).

Supplemental Information

Modifying the Magnetoelectric Coupling in TbMnO₃ by low-level Fe³⁺ Substitution

A. Maia¹, R. Vilarinho², C. Kadlec¹, M. Lebeda¹, M. Mihalik jr.³, M. Zentková³, M. Mihalik³, J. Agostinho Moreira², S. Kamba¹

¹*Institute of Physics of the Czech Academy of Sciences, Na Slovance 2, 182 21 Prague 8, Czech Republic*

²*IFIMUP, Physics and Astronomy Department, Faculty of Sciences, University of Porto, Rua do Campo Alegre 687, s/n- 4169-007 Porto, Portugal*

³*Institute of Experimental Physics of the Slovak Academy of Sciences, Watsonova 47, Košice, Slovak Republic*

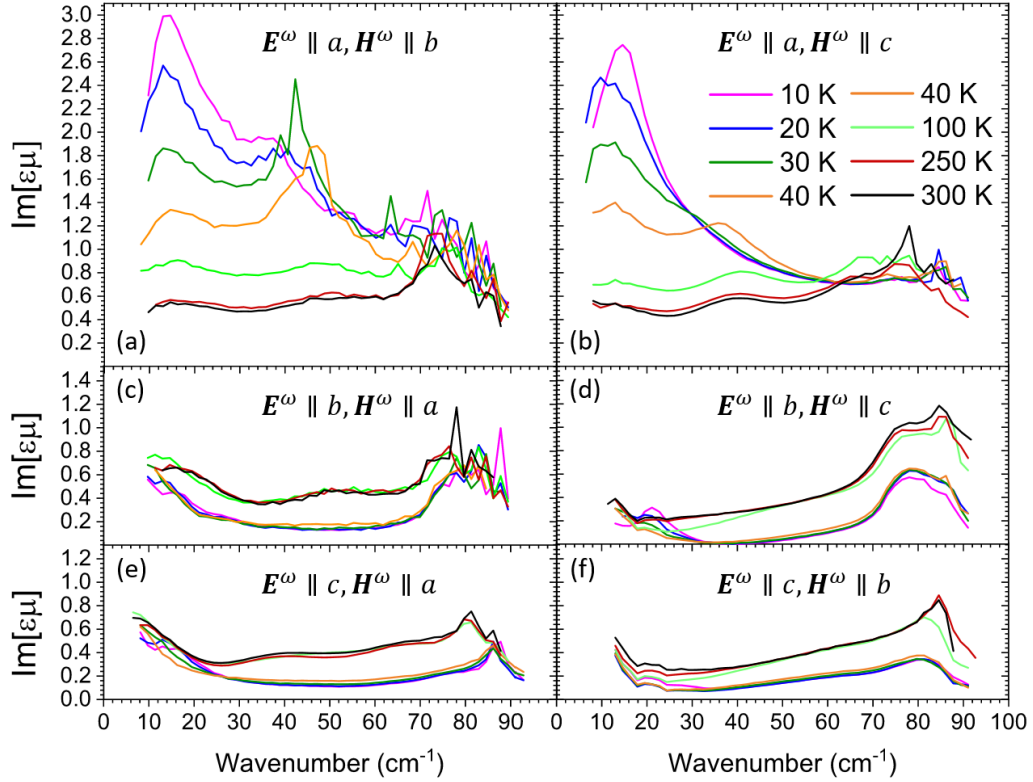


Figure S1. Temperature dependence of the $Re[\epsilon\mu]$ and $Im[\epsilon\mu]$ spectra of $TbMn_{0.96}Fe_{0.04}O_3$ for all the E^ω , H^ω polarization configurations of the THz radiation. The sharp peak seen at 100 K near 45 cm^{-1} is a consequence of high inaccuracy at this frequency due to high opacity of the sample.

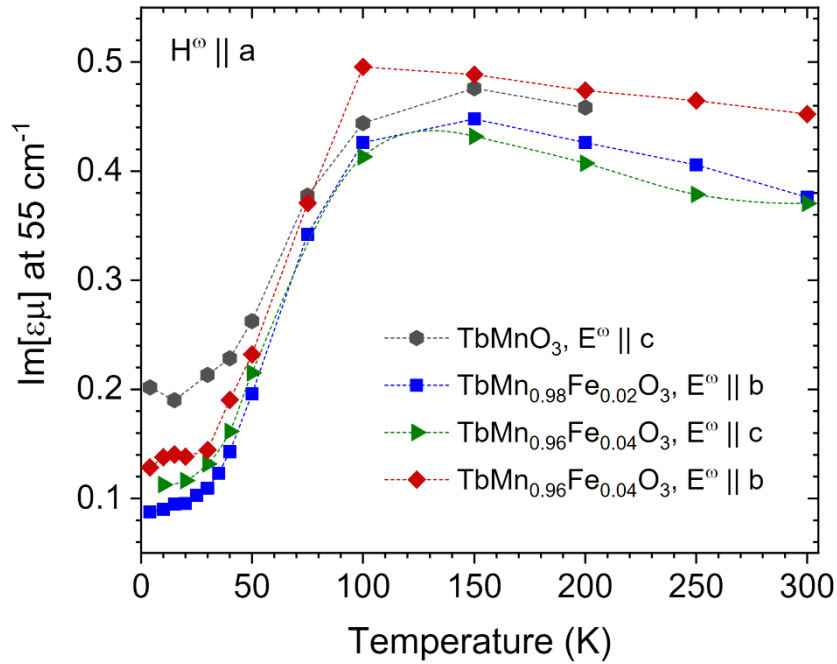


Figure S2. Temperature dependence of the $Im[\epsilon\mu]$ spectra at 55 cm^{-1} for $H^\omega \parallel a$ of $TbMn_{1-x}Fe_xO_3$ for $x = 0, 0.02$ and 0.04 .

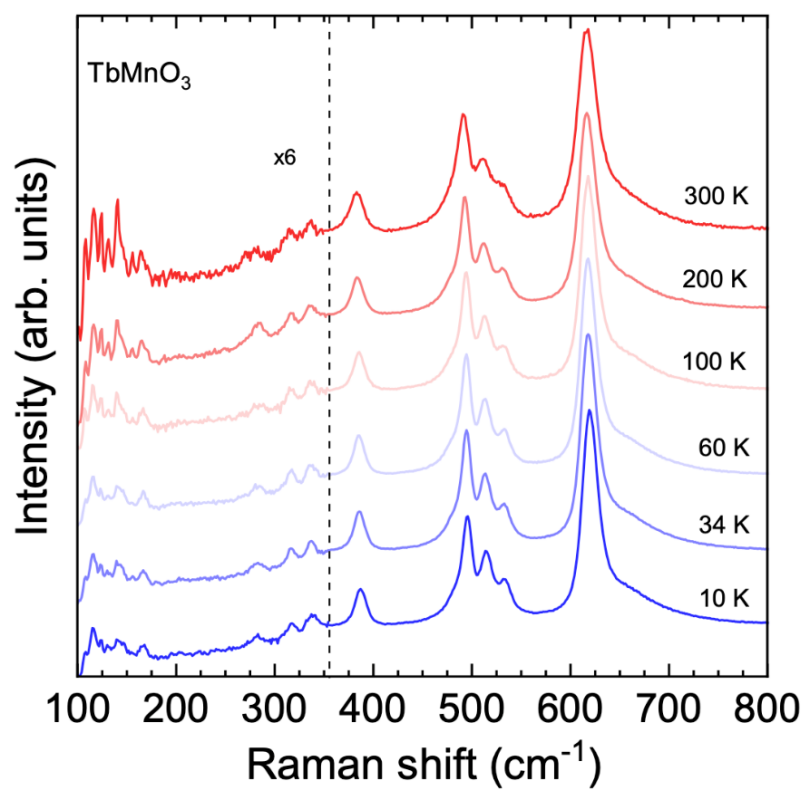


Figure S3. Unpolarized Raman spectra of TbMnO₃ recorded at several temperatures. The spectra below 354 cm⁻¹ are multiplied by 6 for clarity.

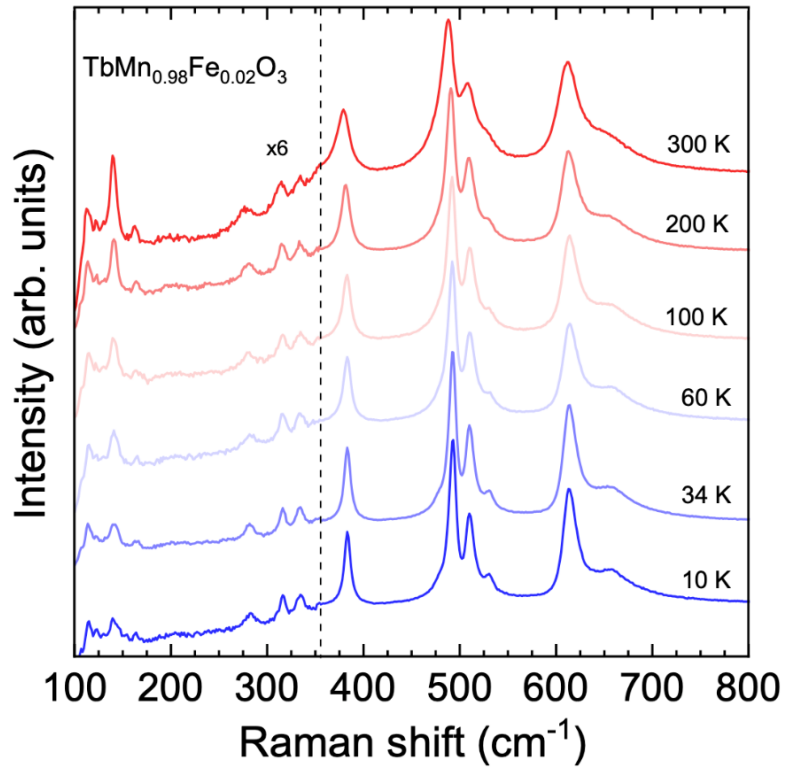


Figure S4. Unpolarized Raman spectra of $\text{TbMn}_{0.98}\text{Fe}_{0.02}\text{O}_3$ recorded at several temperatures. The spectra below 354 cm^{-1} are multiplied by 6 for clarity.

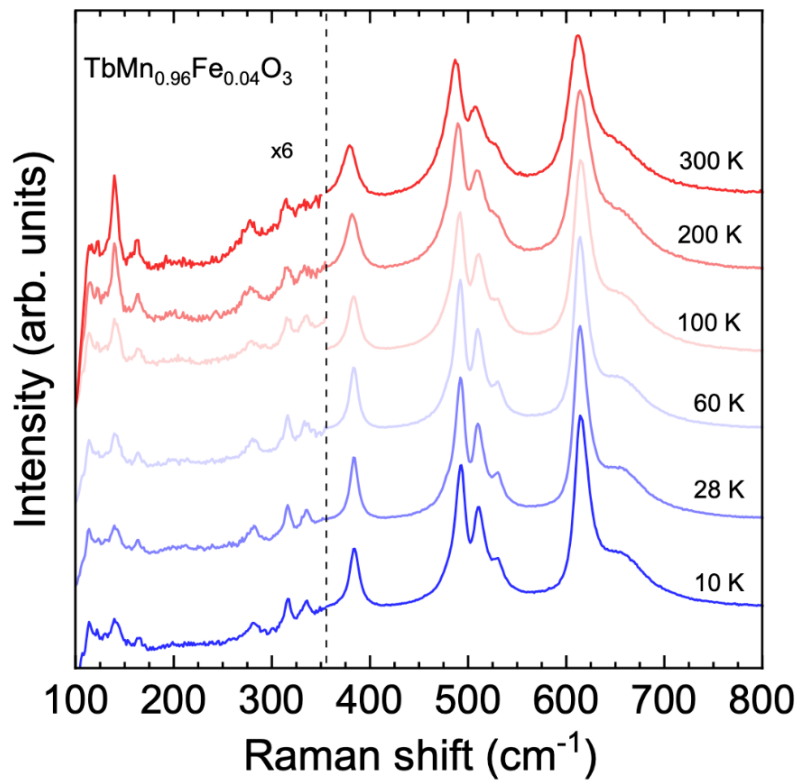







Figure S5. Unpolarized Raman spectra of $\text{TbMn}_{0.96}\text{Fe}_{0.04}\text{O}_3$ recorded at several temperatures. The spectra below 354 cm^{-1} are multiplied by 6 for clarity.

A.4 Strong impact of low-level substitution of Mn by Fe on the magnetoelectric coupling in TbMnO₃

The paper “Strong impact of low-level substitution of Mn by Fe on the magnetoelectric coupling in TbMnO₃”, Ref.^{A4}, is presented in this section.

Strong impact of low-level substitution of Mn by Fe on the magnetoelectric coupling in TbMnO₃A. Maia ¹, R. Vilarinho ², P. Proschek,³ M. Lebeda,¹ M. Mihalik, Jr. ⁴, M. Mihalik,⁴ P. Manuel,⁵ D. D. Khalyavin,⁵ S. Kamba ¹ and J. Agostinho Moreira ²¹*Institute of Physics of the Czech Academy of Sciences, Na Slovance 2, 182 00 Prague, Czech Republic*²*IFIMUP, Physics and Astronomy Department, Faculty of Sciences, University of Porto, 4169-007 Porto, Portugal*³*Faculty of Mathematics and Physics, Charles University, Ke Karlovu 5, 121 16 Prague, Czech Republic*⁴*Institute of Experimental Physics Slovak Academy of Sciences, Watsonova 47, 040 01 Košice, Slovak Republic*⁵*ISIS Facility, Rutherford Appleton Laboratory, Harwell Campus, Didcot OX11 0QX, United Kingdom*

(Received 20 December 2023; revised 29 February 2024; accepted 24 July 2024; published 9 August 2024)

The correlation between static magnetoelectric coupling and magnetic structure was investigated in TbMn_{0.98}Fe_{0.02}O₃ with magnetic field up to 8 T and down to 2 K. Single-crystal neutron diffraction experiments reveal a substantial increase in the temperature dependence of the incommensurate modulation wave vector of the antiferromagnetic phase as the magnetic field strength increases. Magnetic field-dependent pyroelectric current measurements revealed significantly higher magnetoelectric coupling at magnetic fields below 4 T than in pure TbMnO₃. This is due to the higher sensitivity of the incommensurably modulated cycloid structure to weak magnetic fields. Detailed analysis of our data confirmed that the ferroelectric polarization is induced by inverse Dzyaloshinskii-Moriya interaction for magnetic field strength up to 4 T, but at higher fields a departure from theoretical predictions is ascertained, giving evidence for an additional, as yet misunderstood, contribution to magnetoelectric coupling. It shows that a small 2% substitution of Mn³⁺ by Fe³⁺ has a strong impact on the magnetic structure, promoting the destabilization of the incommensurably modulated magnetic cycloidal structure of TbMnO₃ in a magnetic field above 5 T. We demonstrate that the magnetoelectric coupling magnitude can be tuned through suitable substitutional elements, even at low level, inducing local lattice distortions with different electronic and magnetic properties.

DOI: [10.1103/PhysRevMaterials.8.084405](https://doi.org/10.1103/PhysRevMaterials.8.084405)

I. INTRODUCTION

Magnetoelectric multiferroics, where spontaneous long-range magnetic ordering and ferroelectricity coexist and are coupled, represent a very attractive class of compounds combining rich and fascinating fundamental physics [1,2]. A key point to be studied in this report is the effect of controlled chemical substitution on the relationship between structure, magnetism, ferroelectricity, and magnetoelectric coupling. In this regard, the solid solution TbMn_{1-x}Fe_xO₃ proved to be a suitable system to unravel such delicate coupling between magnetism and ferroelectricity [3–6]. Although the Mn³⁺ cation is Jahn-Teller active, unlike the Fe³⁺ cation, they have the same ionic radius for the sixth coordination, allowing one to synthesize isostructural solid solutions in the entire x range. However, the substitution of Mn³⁺ by Fe³⁺ implies a change in the octahedra distortions of perovskite lattice, with a high impact on the magnetic and polar properties. Previous experimental studies in TbMn_{1-x}Fe_xO₃ at ambient temperature have evidence for the linear decrease of the cooperative Jahn-Teller distortion amplitude for $0 \leq x \leq 0.5$, and its suppression for higher Fe concentrations [7]. Furthermore, the octahedra tilting has been found to be sensitive to the amplitude of the Jahn-Teller distortion, which gives clear evidence for the role played by the interplay between structure and magnetism, with impact on the ferroelectric stabilization [7].

TbMnO₃ is a type-II multiferroic [8] prototype with a large magnetoelectric coupling. Its phase diagram can be summarized as follows. At room conditions, TbMnO₃ is a paraelectric paramagnet with orthorhombic crystal structure described by the $Pbnm$ space group [8]. At $T_N = 41$ K, TbMnO₃ undergoes an antiferromagnetic (AFM) phase transition, with incommensurate sinusoidal collinear order of the Mn³⁺ spins [9,10]. In this phase, the spins are aligned along the b axis with a temperature-dependent propagation vector, taking the value $\mathbf{q}_m = (00.291)$ at T_N [9,10]. Accompanying the magnetic modulation structure, there is a lattice modulation with the wave vector found to be $\mathbf{k}_1 = 2\mathbf{q}_m$ [11,12]. Below $T_C = 28$ K, the sinusoidal spin modulation turns into a cycloidal spiral in the bc plane, as revealed by neutron diffraction studies [9,10]. Whether the magnetic modulation remains incommensurate or changes into commensurate is still a matter of debate, since it becomes weakly temperature-dependent below T_C but not completely locking in a fixed commensurate value [9–11,13]. The emergence of a spontaneous electric polarization along the c axis coincides with the cycloid spin ordering below T_C , implying an intrinsic entanglement between the spiral-type antiferromagnetism and ferroelectricity [8,14]. According to Aliouane *et al.* [15], TbMnO₃ exhibits quadratic magnetoelastic coupling in the absence of applied magnetic field. Still, a linear magnetoelastic coupling emerges in TbMnO₃ when an external magnetic field is applied along the b axis, so that ferroelectricity is no longer a secondary effect [15]. The linear magnetoelastic cou-

pling drives a magneto-structural transition from the cycloidal modulated phase, with the spontaneous polarization along the c axis, to a phase with the spontaneous polarization along the a axis, for a magnetic field higher than 4.5 T [14]. When the external field is applied along the a axis, a similar flop is found but at higher critical field of about 9 T [14]. Upon further temperature decrease, a quasi-long-range ordering of the f electrons spins of the Tb^{3+} ions takes place below $T_N^{\text{Tb}} \approx 7$ K [9,10].

In general, the isovalent partial substitution of Mn by Fe ($\text{TbMn}_{1-x}\text{Fe}_x\text{O}_3$) modifies the sequence of phase transitions [5]. However, for low-level substitution, corresponding to $0 < x < 0.05$, the phase sequence is found to be the same as in TbMnO_3 , although both T_N and T_C decrease with increasing x , while T_N^{Tb} barely shifts [6]. The critical temperatures decrease with increasing x gives clear evidence for the destabilization of the magnetic interactions underlying the magnetic properties [6]. The main outcome concerns the decrease of the maximum electric polarization as Fe^{3+} content increases towards $x = 0.04$, which has been attributed to the gradual fading out of the cycloidal spin ordering with increasing x , and the suppression of ferroelectricity for $x \geq 0.05$ [6].

Most of the previous studies in the multiferroic region of the $\text{TbMn}_{1-x}\text{Fe}_x\text{O}_3$ solid solution ($0 < x < 0.05$) relied on polycrystalline samples, losing information regarding the anisotropic properties of both polarization and magnetism [4,6]. Because such features play important roles in the pure compound, they are assumed to be particularly important in the multiferroic region of the solid solution as well. In particular, the direction of the applied magnetic field should have interesting effects on the magnetic structure, some of which is inferred by the direction of polarization switching from the c to the a axis [14]. To understand in more detail the magnetic structure and magnetoelectric coupling of low-level Fe-substituted TbMnO_3 , we performed a detailed study of the temperature and magnetic field dependence of the ferroelectric polarization of oriented $\text{TbMn}_{0.98}\text{Fe}_{0.02}\text{O}_3$ single crystals. Neutron diffraction data in $\text{TbMn}_{0.98}\text{Fe}_{0.02}\text{O}_3$ are discussed in connection with the results of polarization measurements, towards the characterization of the magnetoelectric coupling. The systematic study of magnetoelectric phenomena provides a deeper understanding of the effect of the B-site cation on the microscopic mechanisms underlying the magnetic and polar properties in TbMnO_3 .

II. EXPERIMENTAL DETAILS

High-quality $\text{TbMn}_{0.98}\text{Fe}_{0.02}\text{O}_3$ single crystals were grown by the floating zone method in an FZ-T-4000 (Crystal Systems Corporation) mirror furnace, using MnO_2 , Tb_4O_7 , and Fe_2O_3 as starting materials. The starting powders were mixed in the intended Tb:Mn:Fe stoichiometric ratio, cold pressed into rods, and sintered at 1100 °C for 12–14 h in air. Growing was performed in air atmosphere, feed and seed rod were rotated with a speed of 30 rpm in opposite directions, and a pulling speed of 6 mm/h was used. The typical length of a grown ingot was between 3 and 5 cm [3,4]. The obtained ingot was oriented using Laue diffraction patterns, and special care was taken to avoid macle. The samples were cut from a macle-free region of the oriented ingot. The samples were

first characterized by x-ray diffraction and Raman scattering at room temperature, and temperature-dependent magnetization and specific heat. The obtained results are in good agreement with published data [3,4].

The pyroelectric currents were measured in a standard Quantum Design PPMS while heating at a rate of 5 K min⁻¹, after cooling under a fixed applied magnetic field. The pyroelectric current measurements were performed after poling the crystals with an electric field of 100 V mm⁻¹, while cooling from a temperature above the Néel temperature. Before measuring, the poling electric field was turned off at 2 K. The temperature dependence of the electric polarization was obtained through time integration of the measured pyroelectric currents.

Single-crystal neutron diffraction under applied magnetic field was measured at Wish beamline of the ISIS Neutron and Muon Source at the Rutherford Appleton Laboratory of the Science and Technology Facilities Council. Single-crystal neutron diffraction patterns were recorded at fixed temperatures between 5 and 50 K after cooling the sample under an applied magnetic field along the b axis, up to 8 T. The sample was inserted in a helium flow Oxford cryostat, placed in such a way that the b axis is oriented in the vertical direction, parallel to the applied magnetic field, generated by a 9 T magnet. This magnet has an 80° window in the horizontal and a 30° one in the vertical directions. Due to the magnet surrounding the sample, only a restricted angle range could be measured. With this configuration, a limited number of nuclear and magnetic diffraction peaks could be studied as a function of temperature and magnetic field, with the condition that the (hkl) peaks have $k = 0$ or $k = q_{\text{Mn}}$.

III. RESULTS

A. Polar properties under magnetic field

This section is focused on the temperature dependence of the electric polarization, obtained in the following measurement configurations: $\mathbf{E}||a$ and $\mathbf{B}||b$, and $\mathbf{E}||c$ and $\mathbf{B}||a, b$, and c , for which the largest effects of the applied magnetic field on the polar properties of $\text{TbMn}_{0.98}\text{Fe}_{0.02}\text{O}_3$ are found.

Figures 1(a) and 1(b) show the temperature dependence of the pyroelectric current density, $J(T)$, of $\text{TbMn}_{0.98}\text{Fe}_{0.02}\text{O}_3$ measured along the a and c axes, respectively, under an applied magnetic field (0–9 T) along the b axis. The corresponding temperature dependence of the electric polarization, along the a and c axis, obtained from the time integration of the pyroelectric current density, is presented in Figs. 1(c) and 1(d), respectively. At 0 T, the pyroelectric current density measured along the c axis, $J_c(T)$, peaks at $T_C = 23$ K, as expected according to earlier reports for $\text{TbMn}_{0.98}\text{Fe}_{0.02}\text{O}_3$ ceramics, evidencing the onset of the ferroelectric phase, with spontaneous electric polarization along the c axis [6]. This anomaly slightly downshifts with increasing magnetic field strength, reaching 21 K at 9 T.

A second anomaly in $J_c(T)$ is observed at lower temperatures, but only for a magnetic field strength above 2 T. This anomaly peaks in opposite sense relatively to the first one, and monotonously upshifts from 6 K, for 2 T, to 14 K, for 9 T. Its amplitude exhibits a nonmonotonous magnetic field dependence, being maximum at 5 T. At 0 T, $P_c(T)$

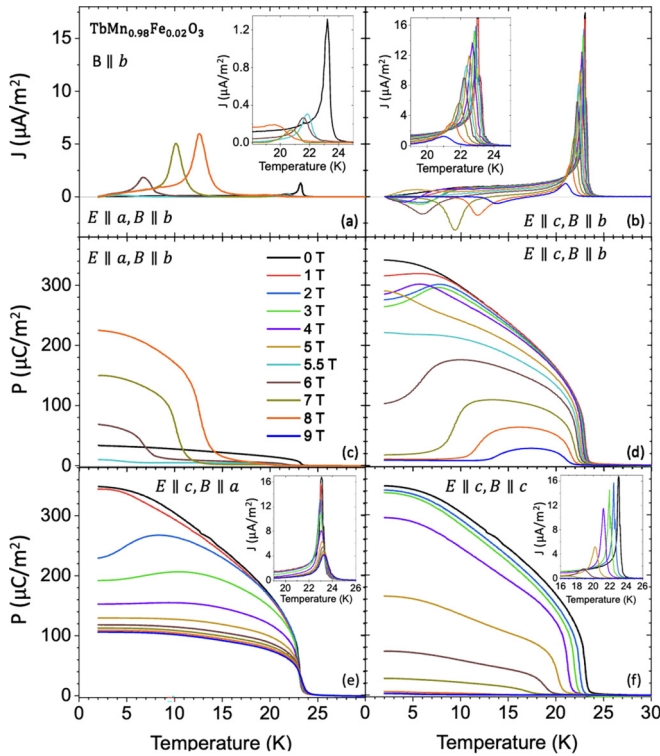


FIG. 1. Temperature dependence of the (a), (b) pyroelectric current densities and (c), (d) electric polarization of $\text{TbMn}_{0.98}\text{Fe}_{0.02}\text{O}_3$, measured along the a and c axes under an applied magnetic field along the b axis. The insets show a magnified view of the temperature profiles of the pyroelectric current density.

monotonously increases on cooling from $T_C = 23$ K, and its value at 2 K is $350 \mu\text{C}/\text{m}^2$, 58% smaller than the maximum polarization observed in TbMnO_3 after poling in twice higher field (200 V mm^{-1}) [14]. The decrease of the P_c value in $\text{TbMn}_{0.98}\text{Fe}_{0.02}\text{O}_3$ has been reported as a consequence of the destabilization of the magnetic structure due to the changes in magnetic interactions promoted by Fe^{3+} [6]. As the magnetic field increases toward 3 T, $P_c(T)$ shows a maximum, peaking at highest temperatures according to the magnetic field strength, and then shifts to lower temperatures on further magnetic field increase up to 5 T. Interestingly, the value of P_c at fixed temperatures decreases at a faster magnetic field rate for $B > 5.5$ T. The $P_c(T)$ curve changes its shape for at 6 T, fading out with decreasing temperature, in such a way that for 9 T, $P_c \sim 0$ below 13 K. Contrarily to TbMnO_3 , the magnetic field evolution of $P_c(T)$, with $B \parallel b$ is more gradual in this compound [14].

Concerning the temperature dependence of the pyroelectric current density recorded along the a axis, $J_a(T)$, a small anomaly at $T_C = 23$ K is already observed for 0 T contrary to pure TbMnO_3 , where no anomaly was detected [14]. As the magnetic field strength increases, the amplitude of this anomaly decreases and downshifts, following a similar temperature trend as observed for $J_c(T)$ [see inset of Fig. 1(a)]. Due to the similar temperature behavior, we assign this anomaly to the minor electric polarization projection in the measurement direction, due to a small misorientation in the sample. A second anomaly in $J_a(T)$ emerges at low tempera-

tures with the same sign as the first one. The second anomaly peaks at higher temperatures, and its amplitude increases as the magnetic field strength increases. These results evidence the enhancement of the electric polarization along the a axis as the magnetic field increases, as seen in Fig. 1(c). The maximum electric polarization along the a axis, recorded at 2 K and 8 T, is about 70% of the maximum spontaneous polarization value measured at the same temperature along the c axis, in the absence of the applied magnetic field. In TbMnO_3 , the maximum value of the electric polarization along the a axis is about 67% of the maximum value of the electric polarization from the c axis, after the magnetically induced polarization flop [14].

Figure 1(e) shows the temperature dependence of the electric polarization measured under applied magnetic field along the a axis ($B \parallel a$). The pyroelectric current $J_c(T)$, shown in the inset of Fig. 1(e), exhibits just one anomaly, peaking at $T_C = 23$ K, weakly dependent on the field strength. However, the amplitude of this anomaly decreases with increasing field strength; consequently, the electric polarization is a decreasing function of the magnetic field strength, gradually converging to the limit value $110 \mu\text{C}/\text{m}^2$, contrarily to what is observed when the magnetic field is applied along the other two crystallographic axes. At 9 T, the value of P_c at the lowest temperature is 25% of the value obtained in TbMnO_3 which, however, was poled at twice higher electric field [14].

Figure 1(f) depicts the temperature dependence of the electric polarization and pyroelectric current [inset of Fig. 1(f)] measured along the c axis, under different magnetic field strength, applied along the same c axis. Only one anomaly is observed in $J_c(T)$ for all the values of the field strength; as consequence, at a fixed magnetic field, the electric polarization increases monotonously on cooling below T_C . Moreover, the $J_c(T)$ anomaly peaks at $T_C = 23$ K for 0 T, monotonously decreasing the peaking temperature as the magnetic field increases, reaching 16 K for 9 T [see inset of Fig. 1(f)]. The amplitude of this anomaly also decreases and eventually disappears for $B > 9$ T, meaning that the electric polarization is a decreasing function of the applied magnetic field along the c axis, reaching negligible values for 9 T. The latter result contrasts with the temperature/magnetic field dependence of the electric polarization of TbMnO_3 measured in the same configuration but poled at twice higher electric field [14]. In fact, for $B < 6$ T, $P_c(T)$ is weakly dependent on the magnetic field, increasing with decreasing temperature, although a change of slope of $P_c(T)$ is observed just below 10 K [14]. However, as the magnetic field increases further from 6 T, the $P_c(T)$ curve profile changes, and, for 8 and 9 T, the electric polarization takes non-negligible values between T_C and 15 K [14].

B. Neutron diffraction

In this section, we will address the temperature and magnetic field dependencies of the measured nuclear and magnetic diffraction peaks. Figure 2 shows representative neutron diffraction patterns, recorded at fixed temperatures in the 5–50 K range, and fixed magnetic field strength (0–8 T range), applied along the b axis. The results recorded for other magnetic field strengths and same temperatures, are

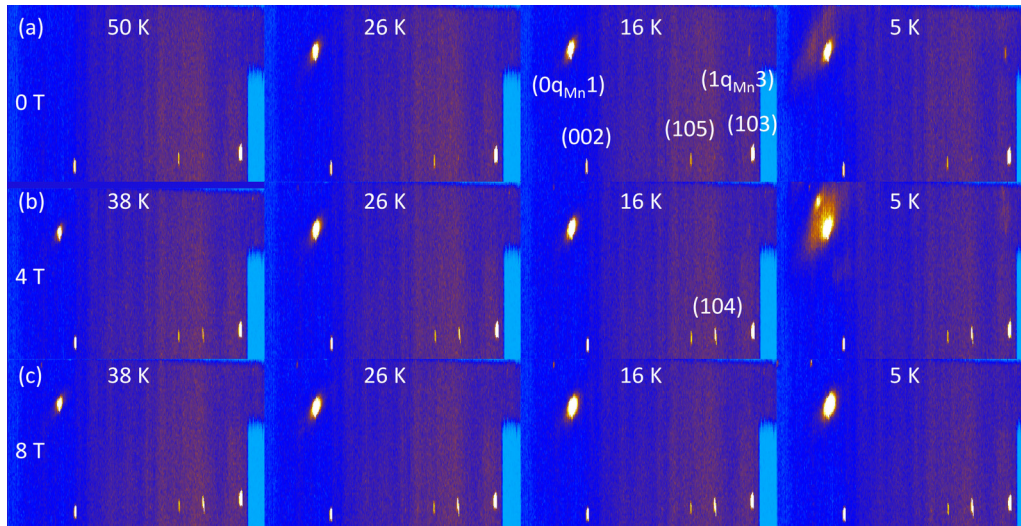


FIG. 2. Diffraction patterns of $\text{TbMn}_{0.98}\text{Fe}_{0.02}\text{O}_3$, recorded at different fixed temperatures and magnetic fields of 0 T (a), 4 T (b), and 8 T (c), applied along the b axis.

shown in Fig. S1 of the Supplemental Material [16]. Only the upper half part of the detectors panel is presented, with the main observed diffraction peaks indexed. Experimental restrictions, due to the configuration of the magnets, prevented us from collecting enough diffraction peaks to determine the real space spin structure.

Above $T_N = 39$ K, only nuclear peaks are observed and are indexed to reflections from the (0 0 2), (1 0 5), and (1 0 3) crystallographic planes. From the analysis of these peaks, the temperature and magnetic field dependence of the a and c lattice parameters was determined, as shown in Fig. S2 of the Supplemental Material for 0 and 8 T, respectively [16]. The lattice parameters slightly decrease with decreasing temperature in the 5–50 K range, and their values are magnetic field independent. These results evidence the negligible influence of both the magnetic phase transitions and the applied magnetic field on the lattice parameters, within the sensitivity of the diffraction technique. However, this does not mean that the magnetic phase transitions do not involve atomic motions, because the inversion center must be broken for the electric polarization to appear. Recently, spin-phonon coupling was ascertained from a temperature-dependent Raman scattering study in $\text{TbMn}_{0.98}\text{Fe}_{0.02}\text{O}_3$, where small anomalies in the temperature dependence of the wavenumber of some phonons assigned to Tb oscillations and symmetrical stretching mode of the oxygen octahedra were detected [3]. However, the magnetoelastic coupling is rather small in this compound to be observed through neutron diffraction techniques.

As the temperature decreases from $T_N = 39$ K, well-defined magnetic diffraction peaks appear along with the nuclear diffraction peaks (see Fig. 2). This is the case of the magnetic superlattice peak attributed to the Mn^{3+} moment ordering with propagation wave vector $(0 q_{\text{Mn}} 1)$ (q_{Mn} is expressed in reciprocal lattice units, r.l.u.), which appears just below T_N , as was also reported for TbMnO_3 [9,10,12]. This peak is observed in the 0–8 T magnetic field strength range. On further cooling, a second magnetic superlattice peak appears, but only below $T_C = 23$ K. Following Kajimoto *et al.*, we assign this peak to the G -type propagation wave vec-

tor $(1 q_{\text{Mn}} 3)$ of the Mn^{3+} moment ordering structure; the intensity of the $(1 q_{\text{Mn}} 3)$ magnetic superlattice peak strongly increases below T_C of TbMnO_3 , being negligibly small above this temperature [10]. Due to the limited q space covered in this experiment, we could not observe the Tb^{3+} magnetic superlattice peaks. Still, the Tb^{3+} spin ordering is ascertained from the appearance of other magnetic superlattice peaks and a strong diffuse scattering around the $(0 q_{\text{Mn}} 1)$ peak. Under applied magnetic field, we observe an additional Bragg peak indexed to $(1 0 4)$ and assigned to a (weak) ferromagnetic spin ordering, likely associated with a spin canting induced by the applied field. In the following, we shall address the temperature and magnetic field dependencies of the magnetic diffraction peaks.

Figure 3(a) shows the temperature dependence of the intensity of the magnetic superlattice peak $(0 q_{\text{Mn}} 1)$, recorded at 0, 4, 6, and 8 T, as representative examples. On cooling below $T_N = 39$ K, the intensity of this reflection increases and is enhanced by the applied magnetic field, the effect being more pronounced in the temperature range of the ferroelectric phase. A detailed analysis of the temperature dependence of the intensity of the magnetic superlattice peak $(0 q_{\text{Mn}} 1)$ reveals a small magnetic field-dependent kink at T_C , which, for the case of $B = 0$ T as a representative example, can be clearly observed in the inset of Fig. 3(a), where the solid line describes the temperature-dependent intensity, $I(T)$, in the $T_C < T < T_N$ range, extrapolated for $T < T_C$. The small but clear deviation of the experimental intensity on cooling below T_C was also reported for TbMnO_3 [9,10], and it gives clear evidence for the interplay between magnetism and ferroelectricity in these compounds. On further cooling, the intensity of the reflection exhibits different temperature behavior, depending on the magnetic field strength: while for 0 T and 4 T, a maximum is ascertained at 10 K, a sudden increase of the intensity at 10 K and at 14 K is observed for 6 T and 8 T, respectively. The temperature dependence of the modulation wave number q_{Mn} , determined from the magnetic superlattice peak $(0 q_{\text{Mn}} 1)$ position, recorded for different field strengths,

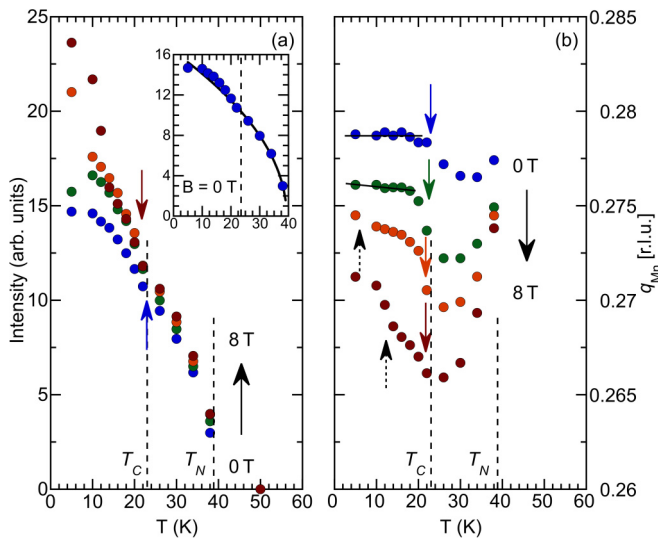


FIG. 3. Temperature dependencies of the (a) intensity and (b) q_{Mn} of the magnetic superlattice peak ($0 q_{Mn} 1$), recorded at 0, 4, 6, and 8 T, as representative examples. The vertical dashed lines mark the Mn^{3+} magnetic ordering temperatures at 0 T. The colored arrows point at the critical temperature T_C where the pyroelectric current density curve exhibits maximum value, while the black dashed arrows in (b) point at the temperatures where anomalous increasing of q_{Mn} is ascertained. Inset: Temperature dependence of the magnetic superlattice peak measured at $B = 0$ T. The solid line represents the temperature trend of the peak intensity in the $T_C < T < T_N$ range, extrapolated to $T < T_C$.

is presented in Fig. 3(b). In the absence of an applied magnetic field and at 38 K, $q_{Mn} = 0.278$, which is about 18% smaller than $q_{Mn} = 0.295$ reported for $TbMnO_3$ just below T_N , which evidences for a longer magnetic modulation wavelength in $TbMn_{0.98}Fe_{0.02}O_3$ [9,10,17]. In the whole temperature range here explored, q_{Mn} is a nonmonotonous function of temperature, although the temperature dependence is a function of the magnetic field. In the $T_C < T < T_N$ interval, q_{Mn} reaches a minimum value at temperatures approaching T_C as the magnetic field increases (32 K for 0 T and 24 K for 8 T). The relative variation of q_{Mn} in the $T_C < T < T_N$ range is 0.7%, a much smaller value when compared with $TbMnO_3$, for which the total variation in the sinusoidal incommensurate phase is 3.7% [17].

In the absence of the applied magnetic field, $q_{Mn}(T)$ of $TbMnO_3$ decreases on cooling and remains almost temperature independent below T_C , reaching values 0.276 in Refs. [9,10] and 0.28 in Ref. [17]. In $TbMn_{0.98}Fe_{0.02}O_3$, $q_{Mn}(T)$ slightly increases below 35 K and finally saturates near 0.279. Therefore, the temperature dependence is different between T_N and T_C , although the modulation wave vector in the ferroelectric phase takes similar value, within measurement accuracy, in the pure and iron-substituted samples.

The most significant changes induced by the magnetic field concerning the temperature dependence of q_{Mn} are observed below T_C . For $B \leq 5$ T, $q_{Mn}(T)$ is a slowly varying temperature function on cooling in such a way that an almost constant plateau is reached, while for $B \geq 6$ T, q_{Mn} is strongly temperature dependent, increasing as temperature decreases. At

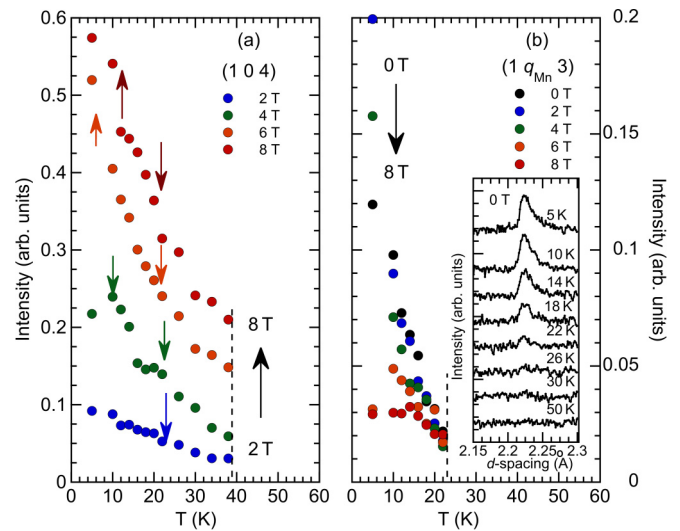


FIG. 4. Temperature dependence of (a) the intensity of the (1 0 4) magnetic diffraction peak and (b) the intensity of the magnetic superlattice peak ($1 q_{Mn} 3$) for $TbMn_{0.98}Fe_{0.02}O_3$, recorded at different fixed magnetic field strength. The colored arrows point at the critical temperature where the pyroelectric current density curve exhibits maximum value. Inset: Neutron diffraction pattern recorded at different fixed temperatures and in the absence of applied field, showing the magnetic superlattice peak ($1 q_{Mn} 3$).

8 T, the relative variation of q_{Mn} between T_C and the base temperature is 0.9%. The magnetic field threshold ($B \sim 5.5$ T) is the one for which the polarization flop is observed [see Figs. 1(c) and 1(d)]. The increasing of $q_{Mn}(T)$ on cooling from T_C contrasts with the observations in $TbMnO_3$, for which at 5.5 T a decrease on cooling is observed [12].

These results give clear evidence for the interplay between the mechanisms underlying the stabilization of the ferroelectricity and the modulation of the Mn^{3+} spin structure. However, the main difference here observed relatively to $TbMnO_3$ concerns the effect of the applied magnetic field, having a stronger effect on the modulation wave vector in the Fe-substituted compound in the whole temperature range, while in $TbMnO_3$ the effect is more pronounced in the cycloidal antiferromagnetic phase [12].

In the absence of an applied magnetic field, the (1 0 4) magnetic peak is not observed in the whole temperature range here explored. Under a 1 T strength magnetic field, this reflection appears just below T_N and its intensity increases with decreasing temperature and increasing magnetic field strength, respectively, as can be seen in Fig. 4(a). The appearance of this magnetic peak clearly points out the stabilization of a ferromagnetic component with increasing the magnetic field. Concomitantly, the intensity of the G -type Mn^{3+} moment ordering magnetic superlattice peak ($1 q_{Mn} 3$), shown in Fig. 4(b), only observed below T_C but already at $B = 0$ T, decreases as the magnetic field increases.

The strong changes induced by the applied magnetic field in the neutron diffraction patterns depicted in Fig. 2 point at magnetic phase transformations below the Tb^{3+} ordering temperature. The diffuse scattering signal, observed around the ($0 q_{Mn} 1$) magnetic superlattice peak, which prevails up to

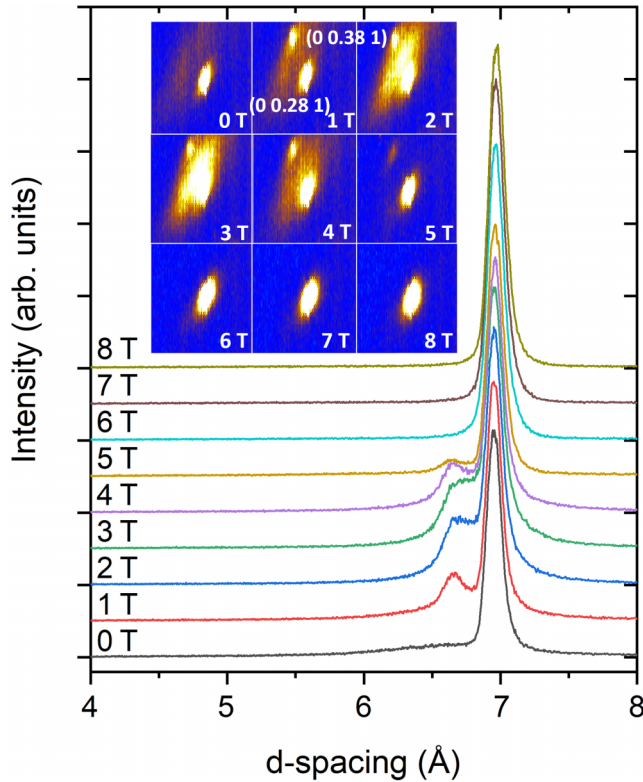


FIG. 5. Neutron diffraction patterns of $\text{TbMn}_{0.98}\text{Fe}_{0.02}\text{O}_3$ recorded at 5 K under several applied magnetic fields along the b axis. The inset shows a detailed view of the neutron diffraction patterns around the $(0 q_{\text{Mn}} 1)$ peak.

4 T, is ascribed to the quite complex and of short-range (local) ordering of Tb^{3+} spins [9,10]. On increasing the magnetic field strength, another magnetic satellite peak starts to be observed, emerging from the diffused scattering signal, as is shown in Fig. 5 for $T = 5$ K. This peak is indexed to the $(0 0.38 1)$ associated with the modulation of the Tb^{3+} spin structure induced by the applied magnetic field. The intensity and width of this magnetic satellite peak are strongly dependent on the applied magnetic field, and it disappears above 5 T. This result evidences a magnetic field-induced transition of the Tb^{3+} spins, with critical field strength of ~ 5 T, which deserve to be further studied.

IV. DISCUSSION

In this section, we will discuss and correlate the results obtained from polarization and neutron diffraction measurements under magnetic field to unravel the microscopic origin of the magnetically induced ferroelectricity in this compound and its magnetic field dependence. We will address the interplay between magnetism and polar properties, highlighted in Fig. 6, which shows the temperature dependence of the pyroelectric current density and the intensity of the magnetic superlattice peak $(0 q_{\text{Mn}} 1)$, for 0, 4, 6, and 8 T magnetic field strength, applied along the b axis, respectively.

The paramagnetic to incommensurate sinusoidal antiferromagnetic phase transition at T_N is not revealed by any anomaly in the pyroelectric current density, as expected if the

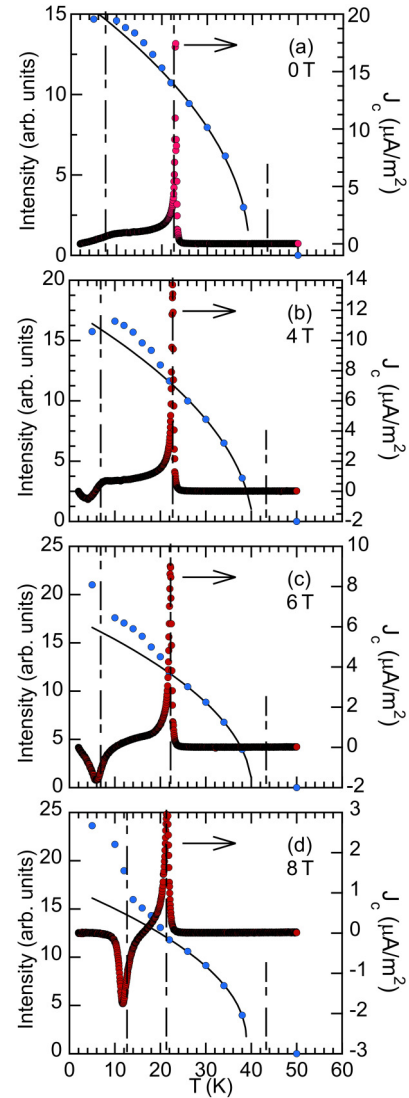


FIG. 6. Temperature dependence of the magnetic superlattice peak $(0 q_{\text{Mn}} 1)$ intensity (left) and the pyroelectric current density (right), measured along the c axis in different magnetic fields applied along the b axis. The solid line represents the temperature trend of the peak intensity in the $T_C < T < T_N$ range, extrapolated to $T < T_C$.

inverse Dzyaloshinskii-Moriya mechanism is assumed only below T_C , like in TbMnO_3 [18,19]. The magnetically induced ferroelectric phase transition is marked by the anomalous temperature dependence of the $(0 q_{\text{Mn}} 1)$ magnetic superlattice peak intensity at T_C . At zero magnetic field, the small anomaly in $J_c(T)$ occurs at 8 K, which is likely associated with the Tb^{3+} spin ordering. The correlation between the anomalous temperature dependence of both $J_c(T)$ and the magnetic superlattice peak $(0 q_{\text{Mn}} 1)$ intensity holds even for applied fields, but following different behavior: at 4 T, $J_c(T)$ exhibits a downward peak at 4 K and the magnetic superlattice peak intensity reaches a maximum value at 10 K; for 6 and 8 T, the downward peak of $J_c(T)$, whose amplitude increases with the field strength, is accompanied by a sudden increase of the slope of the temperature dependence of the magnetic superlattice peak intensity. The spin cycloid is a polar magnetic

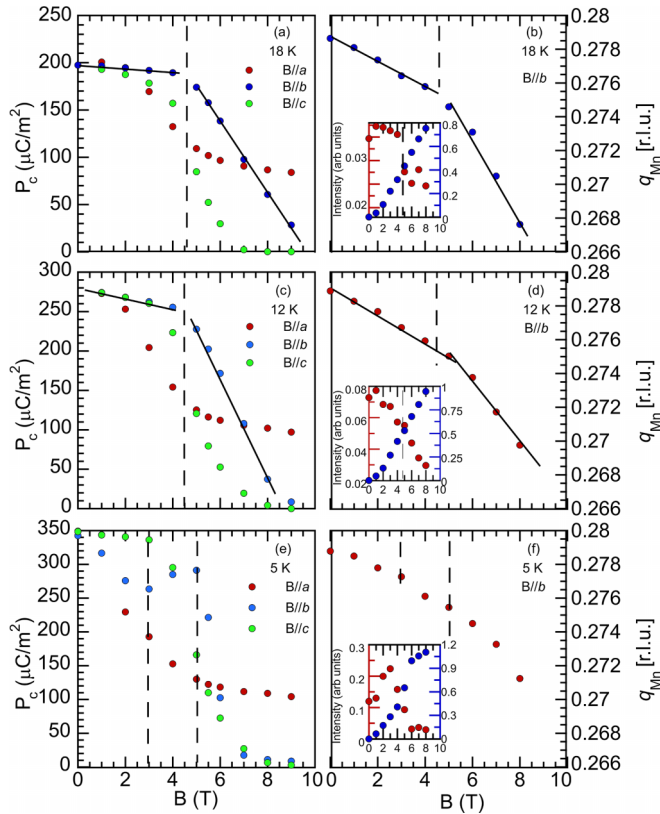


FIG. 7. Magnetic field dependence of the electric polarization P_c measured along the c axis in external magnetic field applied along the $-$, b , and c axes, and the modulation wave vector q_{Mn} , calculated from the $(0 q_{Mn} 1)$ peak position, measured at 18 K (a), (b), 12 K (c), (d), and 5 K (e), (f). Insets: Magnetic field dependence of the intensity of the $(1 q_{Mn} 3)$ magnetic superlattice peak (left red) and the $(1 0 4)$ magnetic peak (right blue).

structure, generating electric polarization in the spin plane, perpendicular to the propagation vector ($\mathbf{P} \sim \mathbf{k} \times (\mathbf{S}_i \times \mathbf{S}_j)$) [18,19]. In the bc -cycloid phase, the electric polarization is expected to be along the c axis, while in the ab -cycloid phase, to be along the a axis. During the cycloid plane rotation from the bc to the ab plane, it is expected an increase of intensity of the $(0 q_{Mn} 1)$ magnetic superlattice peak, simply because in the experimental geometry here described, neutrons probe only the component of magnetic moment perpendicular to the scattering vector, this component being larger when the spins are confined within the ab plane. The results here presented evidence a strong interplay between the modulated magnetic Mn^{3+} spin structure and the stabilization of the electric polarization, as expected in type-II multiferroics.

The interplay between the magnetic structure, electric polarization and magnetoelectric coupling is better ascertained by comparative plots at fixed temperatures. For this purpose, we represent in Fig. 7 the magnetic field dependence of $P_c(T)$, measured with applied magnetic field along the three crystallographic directions, the modulation wave vector q_{Mn} , determined from the magnetic superlattice peak $(0 q_{Mn} 1)$ position, and, in inset, the intensity of the magnetic superlattice $(1 q_{Mn} 3)$ (left axis) and of the ferromagnetic (right axis) peaks. Here we chose to analyze these quantities as a

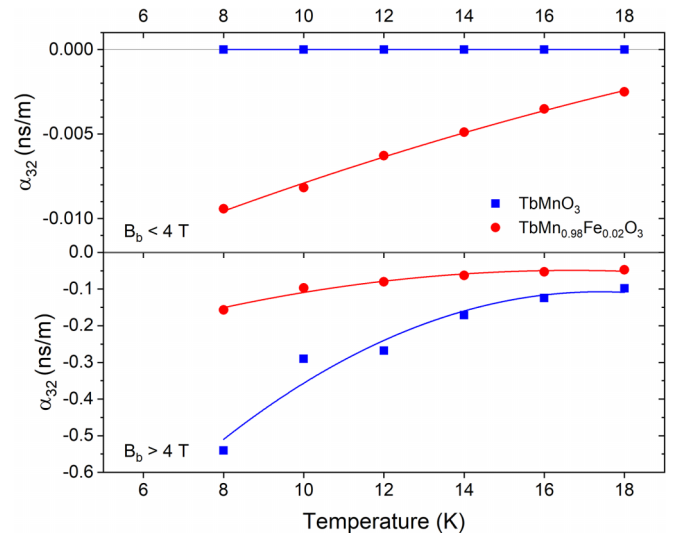


FIG. 8. Temperature dependence of the effective magnetoelectric coefficient α_{32} of TbMnO_3 and $\text{TbMn}_{0.98}\text{Fe}_{0.02}\text{O}_3$ for (a) $B_b < 4 \text{ T}$ and (b) $B_b > 4 \text{ T}$. The solid lines are guide for the eyes. Data concerning TbMnO_3 were taken from Ref. [14].

function of the magnetic field strength at 18 K (for which the a -axis component of the polarization is not observed up to 8 T), 12 K (for which the polarization rotates with applied magnetic field), and 5 K (to study the Tb^{3+} -spin ordering effect), which represent the overall trend of the aforementioned quantities.

For the three chosen representative temperatures, $P_c(B)$ exhibits different magnetic field dependences according to the applied magnetic field direction, mirroring the anisotropic nature of the magnetoelectric coupling. In the 8 to 22 K range, $P_c(B)$ is a linear function of $B \parallel b$ below and above 4.5 T, although with different slopes; it is a linear function of $B \parallel a$ only for $B_a < 4 \text{ T}$ and has a nonlinear dependence with $B \parallel c$, eventually disappearing above a certain value of magnetic field which depends on temperature.

From the slopes of the linear relation between P_c and $B \parallel b$ strength (B_b), we have estimated the effective magnetoelectric coefficient $\alpha_{32} = dP_c/dB_b$ and its temperature dependence is presented in Fig. 8, below and above 4 T.

The effective magnetoelectric coefficient of $\text{TbMn}_{0.98}\text{Fe}_{0.02}\text{O}_3$ is negative, mirroring the decrease the polarization with the magnetic field increase. The value of the magnetoelectric coefficient is one order of magnitude larger for $B_b > 4 \text{ T}$. In both magnetic field ranges, the absolute value α_{32} increases monotonously as temperature decreases, giving evidence for the strengthening of the magnetic field dependence of the electric polarization as the temperature/magnetic field decreases/increases down to 8 K.

Comparing with TbMnO_3 , two different regimes are found, as is clear from Fig. 8. For applied magnetic field strength below 4 T, the effective magnetoelectric coefficient $\alpha_{32} = dP_c/dB_b$ obtained for TbMnO_3 is exactly 0, meaning that while the polarization does not rotate towards the a axis, its value is independent of the applied magnetic field. In contrast, $\text{TbMn}_{0.98}\text{Fe}_{0.02}\text{O}_3$ has a finite negative α_{32} coefficient for the same temperature and magnetic field strength. This result

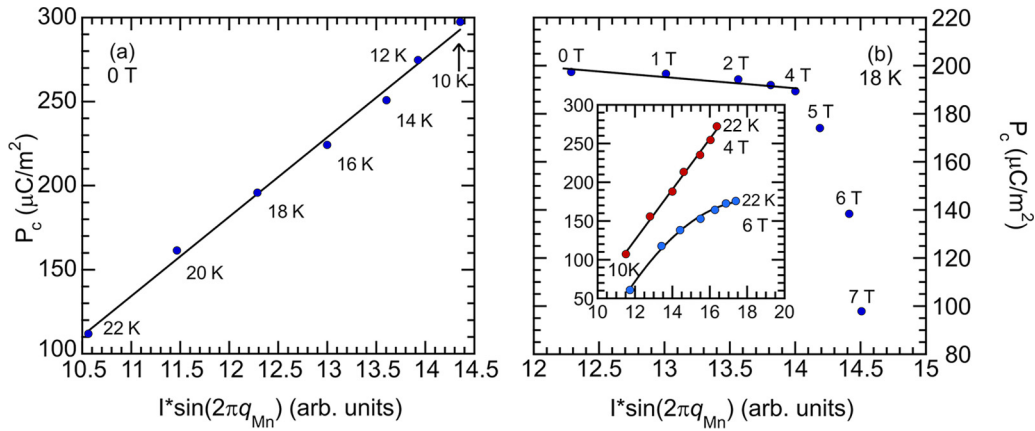


FIG. 9. P_c vs $I \times \sin(2\pi q_{Mn})$ recorded at 0 T for different temperatures (a) and at 18 K with magnetic field $\mathbf{B} \parallel \mathbf{b}$ (b). The intensity I and q_{Mn} values were calculated from the $(0 q_{Mn} 1)$ magnetic superlattice peak. Inset: P_c vs $I \times \sin(2\pi q_{Mn})$ recorded at 4 T and 6 T, for different temperatures.

proves the role played by the Fe^{3+} magnetism, that even a low-level substitution slightly changes the cycloidal ordering, in agreement with the neutron data that show the promotion of a canted structure already at 1 T applied magnetic field. However, above 4 T, the modulus of the effective magnetoelectric coefficient of TbMnO_3 becomes higher than the one calculated for $\text{TbMn}_{0.98}\text{Fe}_{0.02}\text{O}_3$, due to a sharper rotation of the cycloid ordering with the applied magnetic field. The difference between both values increases as temperature decreases, in such a way that at 8 K the effective magnetoelectric coefficient of the pure compound is almost 4 times larger than in the Fe-substituted compound. This demonstrates the strong impact of low-level substitution of Mn^{3+} by Fe^{3+} in the electric polarization dependence on the low applied magnetic field.

Figures 7(b) and 7(d) show the magnetic field dependence of the modulation wave vector q_{Mn} , recorded at 18 K and 12 K, respectively. Two linear regimes in $q_{Mn}(\mathbf{B}_b)$ are ascertained below and above 4.5 T, with a slope increasing from the low to high magnetic field ranges. It is worth stressing that the magnetic field dependence of both $P_c(\mathbf{B}_b)$ and $q_{Mn}(\mathbf{B}_b)$ is rather similar, evidencing a correlation between P_c and the modulated magnetic structure. To discuss the microscopic origin of the magnetically induced ferroelectricity in this compound, we have analyzed the correlation between the electric polarization P_c and the $(0 q_{Mn} 1)$ magnetic superlattice peak characteristics, as it better mirrors the cycloidal spin structure underlying the electric polarization. Following the grounds of the spin current model, presented by Y. Yamasaki *et al.* [20], the electric polarization is predicted to be proportional to the product of $\sin(2\pi q_{Mn})$ and the square of the magnetic structural factor. Unfortunately, the geometric properties of the spin cycloid in this compound could not be determined from our experimental results, and the accurate determination of the magnetic structural factor is not possible. However, we can overcome this difficulty looking at the intensity I of the $(0 q_{Mn} 1)$ magnetic superlattice peak, which is proportional to the square of the magnetic structural factor. Figure 9(a) shows P_c as a function of $I \times \sin(2\pi q_{Mn})$, measured at different temperatures and 0 T. The linear regime observed in the absence of applied field evidences that the mechanism

underlying the magnetoelectric coupling is based on the spin current model applied to a noncolinear spin structure. It is interesting to study the same dependence but at constant temperature and for different applied magnetic field. This study is performed at 18 K where the polarization flip is not observed in the magnetic field range explored in this work. As can be observed in Fig. 9(b), for $B < 4$ T, a linear regime is already found, evidencing that the same microscopic mechanism also prevails in this magnetic field range. However, for $B > 4$ T, a clear deviation of the linear regime is ascertained, enabling us to conclude that the magnetoelectric coupling for $B > 4$ T is not accurately described by the model in Ref. [20]. Actually, the linear dependence of P_c on $I \times \sin(2\pi q_{Mn})$ is broken for magnetic fields above 4 T, as can be observed in the inset of Fig. 9(b). It is worth stressing that q_{Mn} is quite temperature independent for $B < 4$ T, while it becomes strongly temperature dependent for higher fields [see Fig. 3(b)]. The change of magnetic modulation properties at ~ 4 T is undoubtedly in the basis of the change of microscopic mechanisms underlying ferroelectricity. No similar study has been published for TbMnO_3 , to the best of our knowledge, and therefore this work provides a better understanding of the influence of the applied magnetic field on the microscopic mechanisms that induce electric polarization in this class of multiferroics.

Now, we focus on the decrease of P_c of $\text{TbMn}_{0.98}\text{Fe}_{0.02}\text{O}_3$ for $\mathbf{B} \parallel \mathbf{b}$ at 18 K with increasing magnetic field strength. It is worth stressing that at this temperature and for maximum magnetic field strength here applied, no polarization flop occurs. At this temperature, the intensity of the ferromagnetic reflection is a linear increasing function of $\mathbf{B} \parallel \mathbf{b}$, and no anomaly is ascertained at ~ 4.5 T [see inset of Fig. 7(b)], which gives clear evidence for the increase of the ferromagnetic component induced by the applied magnetic field, likely due to a spin canting. The destabilization of the cycloidal Mn^{3+} spin modulation, along with the concomitant appearance of a ferromagnetic component, explain the decrease of the P_c . This result obtained for $\text{TbMn}_{0.98}\text{Fe}_{0.02}\text{O}_3$ contrasts with the one obtained for pure TbMnO_3 from which we conclude that the magnetic field promoted spin canting is a consequence of the Fe spins, even in only 2% concentration [14]. Similar magnetic changes are perceived down to

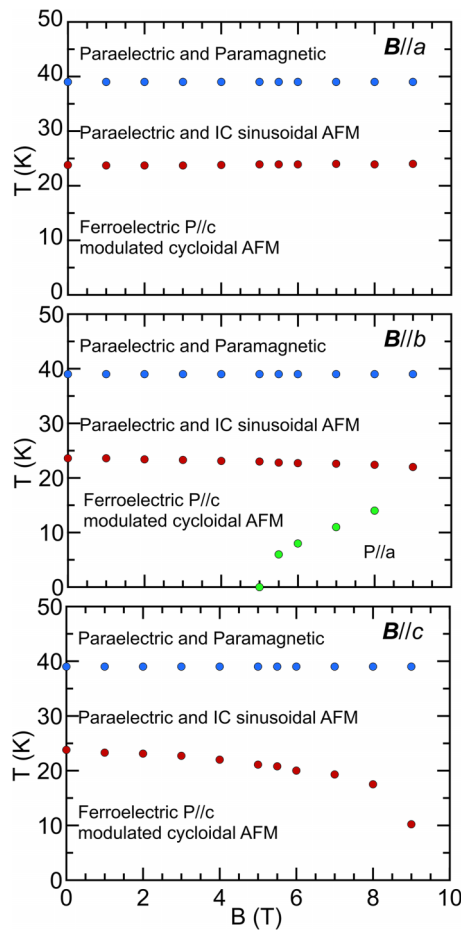


FIG. 10. The magnetolectric phase diagram of $\text{TbMn}_{0.98}\text{Fe}_{0.02}\text{O}_3$, with magnetic fields along the (a) a , (b) b , and (c) c axes. Antiferromagnetic structure has incommensurate sinusoidal modulation between T_N and T_C and cycloidal modulation below T_C .

8 K. Future experiments will be performed to confirm this interpretation.

The magnetolectric coupling at 5 K exhibits different properties. Strictly, q_{Mn} is no longer a linear function of the applied magnetic field [see Fig. 7(f)] and a hint of a downward jump is ascertained at 3.5 T. Interestingly, the magnetic field dependence of the G -type magnetic superlattice peak (1 q_{Mn} 3) intensity exhibits a maximum value at 3 T and becomes magnetic field independent above 5 T, while the (1 0 4) magnetic reflection intensity exhibits an s-shaped anomaly at 5 T. Revisiting Fig. 7(f), we can assign the aforementioned intensity changes at 5 T to the magnetically

induced phase transition. The different behavior described to the one above is a consequence of the Tb^{3+} magnetic ordering on the magnetolectric coupling at 5 K.

To summarize the results here presented, we propose the magnetolectric phase diagram of $\text{TbMn}_{0.98}\text{Fe}_{0.02}\text{O}_3$ shown in Fig. 10, with magnetic fields along the Fig. 10(a) a , Fig. 10(b) b , and Fig. 10(c) c axes.

V. CONCLUSIONS

In this work we report a combined experimental study of the temperature and magnetic field dependence of polarization and magnetic structures in $\text{TbMn}_{0.98}\text{Fe}_{0.02}\text{O}_3$ single crystal. The results show that the low level of Mn^{3+} substitution for Fe^{3+} , although it does not change the phase sequence regarding TbMnO_3 , causes a higher magnetic field sensitivity of the electric polarization for $B < 4$ T. This is due to the changes on the magnetic modulation of the Mn^{3+} spin structure. Two main consequences arise from the magnetic structure changes: (1) the value of the electric polarization is lower than in TbMnO_3 , and (2) the magnetolectric coupling coefficient α_{32} at low magnetic fields below 4 T is finite, ranging between -0.005 ns/m to -0.01 ns/m, contrasting with the vanishing value reported for TbMnO_3 , meaning that while the polarization does not rotate towards the a axis, its value is independent of the applied magnetic field. We attribute this magnetolectric performance enhancement to the effect of the Fe^{3+} magnetism, which alters the magnetic interactions to such an extent that the magnetic structure allowing for ferroelectricity, according to Dzyaloshinskii-Moriya interaction, is no longer stable at high magnetic fields. Our experimental work evidences that the low-level substitution of Mn^{3+} by Fe^{3+} , though keeping the same phase sequence, induces significant changes in properties and evidence for the rather delicate balance between the competitive magnetic interactions underlying the ground state of TbMnO_3 .

ACKNOWLEDGMENTS

This work was supported by the Scientific Grant Agency MŠVVaŠ SR and SAS Project No. VEGA 2/0011/22, the Czech Science Foundation (Project No. 21-06802S), a project from the European Union, and the Czech Ministry of Education, Youth and Sports (Projects No. TERA FIT-CZ.02.01.01/00/22 008/0004594), No. PTDC/FIS-MAC/29454/2017, No. NORTE/01/0145/FEDER/028538, No. IFIM-UP: Norte-070124-FEDER-000070; NECL: NORTE-01-0145-FEDER-022096, No. UIDB/04968/2020, No. UID/NAN/50024/2019, No. PTDC/NAN-MAT/28538/2017, and No. PTDC/FIS/03564/2022.

The authors declare no competing interests.

- [1] S. Dong, J. M. Liu, S. W. Cheong, and Z. Ren, Multiferroic materials and magnetolectric physics: Symmetry, entanglement, excitation, and topology, *Adv. Phys.* **64**, 519 (2015).
- [2] Y. Tokura, S. Seki, and N. Nagaosa, Multiferroics of spin origin, *Rep. Prog. Phys.* **77**, 076501 (2014).
- [3] A. Maia, R. Vilarinho, C. Kadlec, M. Lebeda, M. Mihalik, M. Zentková, M. Mihalik, J. A. Moreira, and S. Kamba, Modifying

the magnetolectric coupling in TbMnO_3 by low-level Fe^{3+} substitution, *Phys. Rev. B* **107**, 104410 (2023).

- [4] M. Mihalik, M. Mihalik, M. Zentková, A. Maia, R. Vilarinho, A. Almeida, J. Agostinho Moreira, J. Pospíšil, and K. Uhlířová, Magnetic properties of $\text{TbMn}_{0.98}\text{Fe}_{0.02}\text{O}_3$ single crystal, *J. Magn. Magn. Mater.* **549**, 168986 (2022).

- [5] M. Mihalik, M. Mihalik, Z. Jagličić, R. Vilarinho, J. A. Moreira, E. Queiros, P. B. Tavares, A. Almeida, and M. Zentková, Magnetic phase diagram of the $\text{TbMn}_{1-x}\text{Fe}_x\text{O}_3$ solid solution system, *Physica B Condens. Matter* **506**, 163 (2017).
- [6] R. Vilarinho, E. Queirós, D. J. Passos, D. A. Mota, P. B. Tavares, M. Mihalik, M. Zentkova, M. Mihalik, A. Almeida, and J. A. Moreira, On the ferroelectric and magnetoelectric mechanisms in low Fe^{3+} doped TbMnO_3 , *J. Magn. Magn. Mater.* **439**, 167 (2017).
- [7] R. Vilarinho, D. J. Passos, E. C. Queirós, P. B. Tavares, A. Almeida, M. C. Weber, M. Guennou, J. Kreisel, and J. A. Moreira, Suppression of the cooperative Jahn-Teller distortion and its effect on the Raman octahedra-rotation modes of $\text{TbMn}_{1-x}\text{Fe}_x\text{O}_3$, *Phys. Rev. B* **97**, 144110 (2018).
- [8] T. Kimura, T. Goto, H. Shintani, K. Ishizaka, T. Arima, and Y. Tokura, Magnetic control of ferroelectric polarization, *Nature (London)* **426**, 55 (2003).
- [9] M. Kenzelmann, A. B. Harris, S. Jonas, C. Broholm, J. Schefer, S. B. Kim, C. L. Zhang, S. W. Cheong, O. P. Vajk, and J. W. Lynn, Magnetic inversion symmetry breaking and ferroelectricity in TbMnO_3 , *Phys. Rev. Lett.* **95**, 087206 (2005).
- [10] R. Kajimoto, H. Yoshizawa, H. Shintani, T. Kimura, and Y. Tokura, Magnetic structure of TbMnO_3 by neutron diffraction, *Phys. Rev. B* **70**, 012401 (2004).
- [11] T. Kimura, S. Ishihara, H. Shintani, T. Arima, K. T. Takahashi, K. Ishizaka, and Y. Tokura, Distorted perovskite with e_g^1 configuration as a frustrated spin system, *Phys. Rev. B* **68**, 060403(R) (2003).
- [12] T. Arima, T. Goto, Y. Yamasaki, S. Miyasaka, K. Ishii, M. Tsubota, T. Inami, Y. Murakami, and Y. Tokura, Magnetic-field-induced transition in the lattice modulation of colossal magnetoelectric GdMnO_3 and TbMnO_3 compounds, *Phys. Rev. B* **72**, 100102(R) (2005).
- [13] T. Goto, T. Kimura, G. Lawes, A. P. Ramirez, and Y. Tokura, Ferroelectricity and giant magnetocapacitance in perovskite rare-earth manganites, *Phys. Rev. Lett.* **92**, 257201 (2004).
- [14] T. Kimura, G. Lawes, T. Goto, Y. Tokura, and A. P. Ramirez, Magnetoelectric phase diagrams of orthorhombic RMnO_3 ($R = \text{Gd}, \text{Tb}, \text{and Dy}$), *Phys. Rev. B* **71**, 224425 (2005).
- [15] N. Aliouane, D. N. Argyriou, J. Stempfer, I. Zegkinoglou, S. Landsgesell, and M. v. Zimmermann, Field-induced linear magnetoelastic coupling in multiferroic TbMnO_3 , *Phys. Rev. B* **73**, 020102(R) (2006).
- [16] See Supplemental Material at <http://link.aps.org/supplemental/10.1103/PhysRevMaterials.8.084405> for additional information obtained from the neutron diffraction and pyroelectric current experiments and data analysis: diffraction patterns of $\text{TbMn}_{0.98}\text{Fe}_{0.02}\text{O}_3$, recorded at different fixed temperatures and magnetic fields of 2 T and 6 T, applied along the b -axis; the temperature dependence of the a and c lattice parameters of $\text{TbMn}_{0.98}\text{Fe}_{0.02}\text{O}_3$, measured at 0 T and 8 T; and the magnetic field dependence of the electric polarization P_c measured along the c -axis in external magnetic field applied along the a -, b - and c -axes, at fixed temperatures.
- [17] S. Quezel, F. Tcheou, J. Rossat-Mignod, G. Quezel, and E. Roudaut, Magnetic structure of the perovskite-like compound TbMnO_3 , *Physica B+C* **86**, 916 (1977).
- [18] I. A. Sergienko and E. Dagotto, Role of the Dzyaloshinskii-Moriya interaction in multiferroic perovskites, *Phys. Rev. B* **73**, 094434 (2006).
- [19] H. Katsura, N. Nagaosa, and A. V. Balatsky, Spin current and magnetoelectric effect in noncollinear magnets, *Phys. Rev. Lett.* **95**, 057205 (2005).
- [20] Y. Yamasaki, H. Sagayama, T. Goto, M. Matsuura, K. Hirota, T. Arima, and Y. Tokura, Electric control of spin helicity in a magnetic ferroelectric, *Phys. Rev. Lett.* **98**, 147204 (2007).

Supplemental Information

Strong impact of low-level substitution of Mn by Fe on the magnetoelectric coupling in TbMnO_3

A. Maia¹, R. Vilarinho², P. Proschek³, M. Lebeda¹, M. Mihalik jr.⁴, M. Mihalik⁴, P. Manuel⁵, D. D. Khalyavin⁵, S. Kamba¹, J. Agostinho Moreira²

¹*Institute of Physics of the Czech Academy of Sciences, Na Slovance 2, 182 00 Prague, Czech Republic*

²*IFIMUP, Physics and Astronomy Department, Faculty of Sciences, University of Porto, Porto, Portugal*

³*Faculty of Mathematics and Physics, Charles University, Ke Karlovu 5, 121 16 Prague, Czech Republic*

⁴*Institute of Experimental Physics Slovak Academy of Sciences, Watsonova 47, Košice, Slovak Republic*

⁵*ISIS Facility, Rutherford Appleton Laboratory, Harwell Campus, Didcot OX11 0QX, UK.*

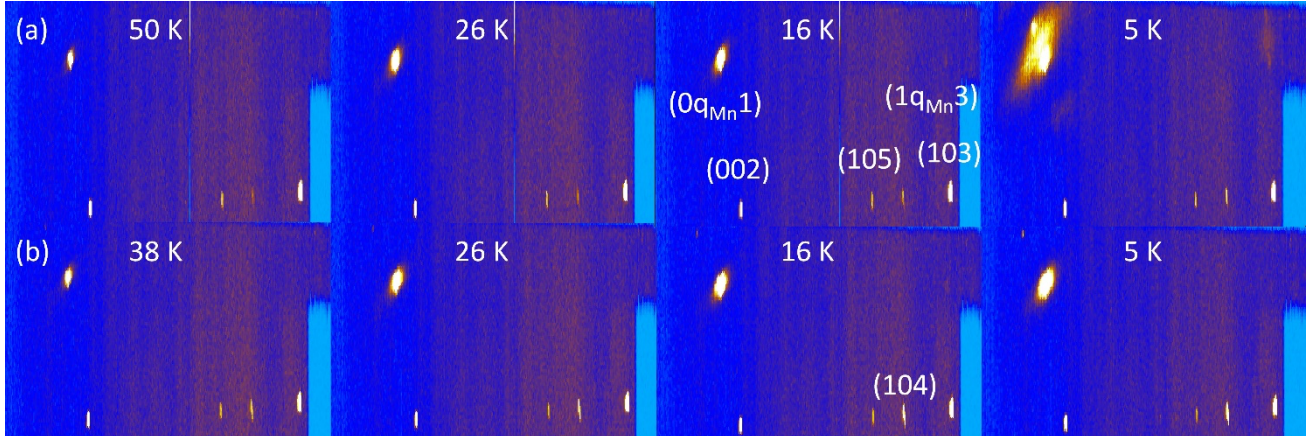


Figure S1. Diffraction patterns of $\text{TbMn}_{0.98}\text{Fe}_{0.02}\text{O}_3$, recorded at different fixed temperatures and magnetic fields of (a) 2 T and (b) 6 T, applied along the b -axis.

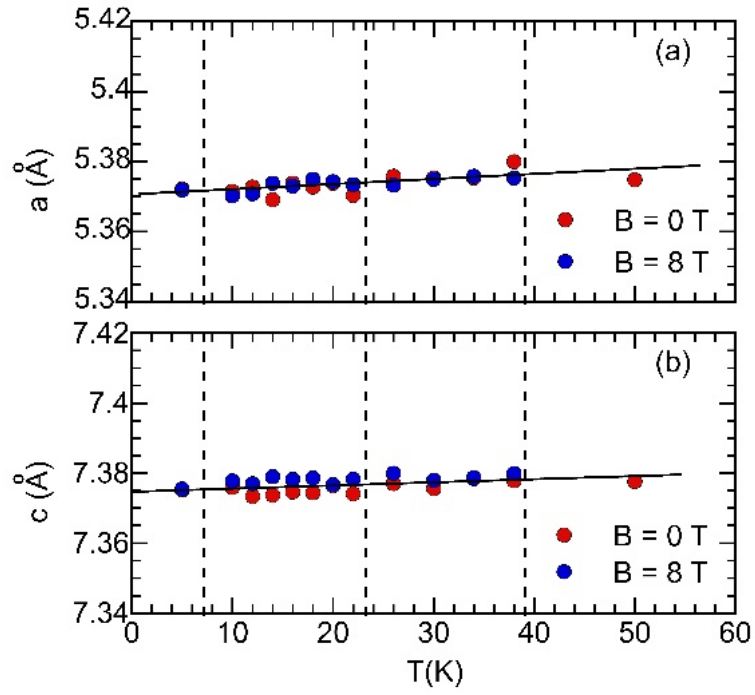


Figure S2. Temperature dependence of the a (a) and c (b) lattice parameters of TbMn_{0.98}Fe_{0.02}O₃, measured at 0 T (red) and 8 T (blue), respectively. The vertical dashed lines mark the critical temperatures and the solid line is a guide for the eyes.

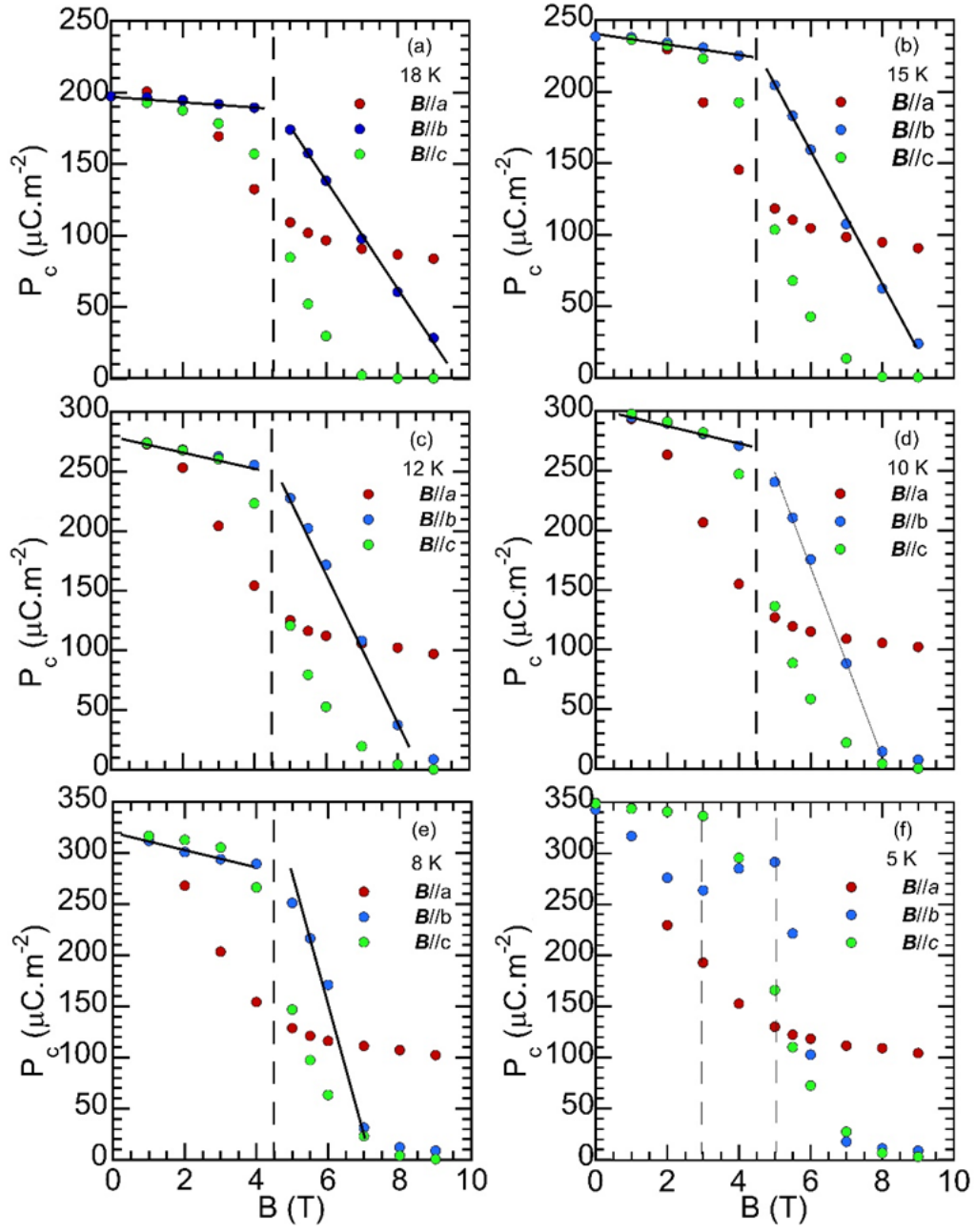


Figure S3. Magnetic field dependence of the electric polarization P_c measured along the c -axis in external magnetic field applied along the a -, b - and c -axes.